NANOSYSTEMS: PHYSICS, CHEMISTRY, MATHEMATICS, 2016, 7 (4), P. 678–682

ZnO decorated graphene nanosheets: an advanced material for the electrochemical performance and photocatalytic degradation of organic dyes

D. M. K. Siddeswara[1], K. R. Vishnu Mahesh[2*], S. C. Sharma[3], M. Mylarappa[4], H. Nagabhushana[5],
K. S. Ananthraju[2], H. P. Nagaswarupa[6], S. C. Prashantha[6], N. Raghavendra[7]

[1]Department of Chemistry Jyothy Institute of Technology, Bengaluru-560082, Karnataka, India
[2]Department of Chemistry, Dayananda Sagar College of Engineering, Kumara Swamy Layout, Bengaluru, 560078, Karnataka, India
[3]Department of Mechanical Engineering, DSCE, Provost, Dayananda Sagar University, Bangalore, 560078, India
[4]Research Center, Department of Chemistry, AMC Engineering College, Bengaluru-83, Karnatak,India
[5]Prof. C. N. R. Rao Centre for Advanced Materials, Tumkur University, Tumkur, 572 103, India
[6]Research Center, 4Department of Science and Humanities, EWIT, Bengaluru-91, India
[7]CMRTU, RV College of Engineering, Bangalore-59, India

*vishnumaheshkr@gmail.com

PACS 81.07.-b **DOI 10.17586/2220-8054-2016-7-4-678-682**

The objective of the current research was mainly focused on synthesizing the Reduced Graphene Oxide (RGO) using modified Hummers method and ZnO functionalized reduced graphene oxide (RGO) composite was fabricated by a one-pot approach. The ZnO functionalized graphene nanosheets were characterized by X-ray diffractometer (XRD) and surface morphology was examined using Transmission Electron Microscopy (TEM). Electrochemical characteristics of the ZnO/RGO composite were investigated through cyclic voltammetry and electrochemical impedance spectroscopy (EIS). The composite was capable of delivering a high specific capacitance with excellent cycling stability. The ZnO decorated RGO catalyst was also applied to degrade different nonvolatile compounds such as Methyl Blue (MB) and Indigo carmine (IC). The performance of RGO/ZnO shows rapid degradation of dyes of high concentrations.

Keywords: Reduced graphene oxide, ZnO, Mn_2O_3, electrochemical, catalytic activity.

Received: 5 Febraury 2016

1. Introduction

Graphene is one-atom thick two-dimensional sheet of carbon atoms fashioned in a honeycomb lattice and is considered as the future revolutionary material [1]. An exponential growth after 2004 in graphene-related research is reflected in the number of publications. Graphene is highly anticipated to be an excellent electrode material due to its notable characteristics such as high surface area to volume ratio, good electrical conductivity, good flexibility, fast electron mobility and good thermal and electrochemical properties [2–4].

Because of its outstanding mechanical properties compared to other carbon materials, has attracted enormous interest. Considering the excellent properties of graphene, ZnO and Mn_2O_3, a combination of graphene with ZnO and Mn_2O_3 nanoparticles (NPs) might provide enhanced performance. Several methods have been carried out to produce graphene/ZnO and graphene/Mn_2O_3 composites. Other researchers have also synthesized graphene/ZnO and graphene/Mn_2O_3, as they appear to be promising materials for pseudocapacitors due to their superior electrochemical performance, environmental friendliness, and lower production costs [5]. The present research is mainly focused on synthesizing Reduced Graphene Oxide (RGO) by using Hummer's method. RGO and metal oxides such as ZnO and Mn_2O_3 composite were fabricated by a one-pot approach. The obtained RGO with metal oxides were characterized using X-ray Diffractometry (XRD) and ZnO and Mn_2O_3 composites were concerning to electrochemical and photocatalytic activity [6–11].

In this report, a simple and facile synthetic route is developed to prepare graphene-ZnO composite as an electrode material and photocatalyst for the organic dyes. Initially, graphene oxide (GO) was synthesized using the well-known modified Hummer's method. ZnO nanorods are inserted between the graphene nanosheets layer-by-layer rather than simply appended to the surface of graphene during the GO hydrothermal reduction process. This strategy provides a novel method for preparing highly active materials (ZnO nanorods) directly grown on Gr surface that avoids the restacking of Gr sheets, which show high electrochemical activity at higher scan rates and superior long-term cycle stability applied in an all solid-state supercapacitor device. Such excellent electrochemical properties provide important prospects for graphene- ZnO hybrid to be widely used as electrode material in supercapacitor [12, 13].

2. Experimental

2.1. Materials

Graphite, zinc nitrate hexahydrate ($Zn(NO_3)_2{\cdot}6H_2O$), sodium nitrate ($NaNO_3$), sulfuric acid (H_2SO_4), hydrochloric acid (HCl), potassium permanganate ($KMnO_4$), hydrogen peroxide (H_2O_2), hydrazine hydrate ($N_2H_4{\cdot}H_2O$) and potassium chloride (KCl) were purchased from Sigma-Aldrich and used without additional purification.

2.2. Synthesis of Graphene Oxide

GO was prepared from natural graphite using a modified Hummers method. In a typical experiment, graphite (1.5 g), $NaNO_3$ (1.5 g) and H_2SO_4 (70 mL) were mixed and stirred in an ice bath. Subsequently, 9 g $KMnO_4$ was added slowly. In a particular reaction condition, water was added slowly, followed by the slow addition of 10 mL 30 % H_2O_2. The above mixture was centrifuged and purified, the sample was dispersed in deionized water to obtain highly exfoliated GO sheets. This as-prepared GO was reduced to obtain RGO.

2.3. Synthesis of RGO/ZnO Composite

Pure ZnO Nano rods were synthesized by hydrothermal method. In a typical experiment, 100 mg of $Zn(NO_3)_2$ was first dispersed into 30 ml deionized water. Then, 15 μl of hydrazine hydrate was added dropwise under stirring, followed by ultrasonication for 30 min. Then, the solution was transferred to a 50 ml Teflon-lined autoclave and heated at 160 °C for 12 h. Finally, the RGO/ZnO nanostructures were collected after washing and centrifugation.

3. Result and Discussion

3.1. X-Ray Diffractometer

Crystalline structure of the materials were examined by an X-ray diffractometer (XRD). It can be seen (Fig. 1) that the ZnO XRD patterns of the nanocomposites with different mass ratios are similar to that of pure zinc oxide, indicating that no other impurity peaks were detected. It can be readily assigned to pure ZnO with hexagonal structure [2]. The XRD pattern confirms the crystalline nature of the as-prepared RGO/ZnO material and the Transmission electron microscopy (TEM) images indicate the presence of nanosheets around the centers.

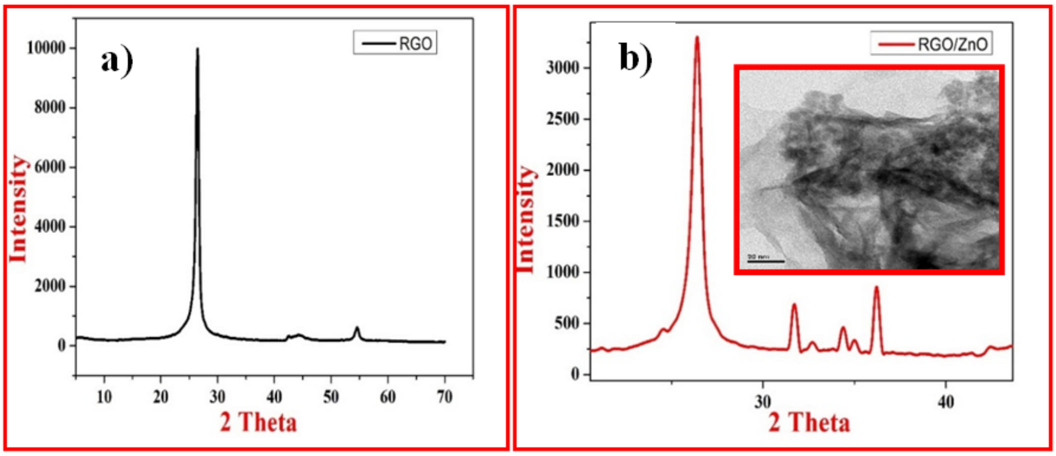

FIG. 1. XRD of a) RGO; b) XRD and TEM image of RGO/ZnO

3.2. Electrochemical Studies

The electrochemical activities of RGO and RGO/ZnO were assessed by cyclic voltammetry, which can provide additional information for material characterization from the shape, the number and the position of the different peak like the redox processes. The obtained black paste was immersed into a homemade disk electrode with glass walls and graphite bar as current collector. A CHI604E work station was used for all electrochemical measurements. Electrochemical measurement utilized three electrode system having working electrode, Ag/AgCl reference electrode and a platinum wire as counter electrode. Cyclic voltammetry (CV) studies were performed in potential between +0 to -1 V using electrolytes at constant scan rate. Cyclic voltammetry was used to determine the influence of RGO/ZnO on the overall charge capacity of the electrode. The value of $E_0 - E_R$ measures the electrode reversibility (E_R), which is one of the predominant factors influencing the power capabilities of electrodes in 0.5 M Na_2SO_4 electrolyte. In Fig. 2(a) the smaller value of $E_0 - E_R$ indicates greater reversibility for the electrode reaction. In the current studies, several scan rates ranging from 10 to 50 mVs^{-1} were used. The effect of scan rate is presented in Fig. 2(b). As the scan rate increased, the CV profile deviated from the ideal capacitive behavior. A smaller the value of RGO/ZnO showed greater reversibility for the electrode reaction. Decreased solution resistance (Rs) values indicate greater conductivity values for the sample. In Fig. 3(a), one can clearly see that the sample RGO/ZnO in 0.5 M Na_2SO_4 shows lower charge transfer resistance (Rct) than the RGO electrode, indicating the enhanced conductivity and confirming that the capacitive behavior is faster, as is shown in Table 1. The simulation of RGO/ZnO is shown in Fig. 3(b).

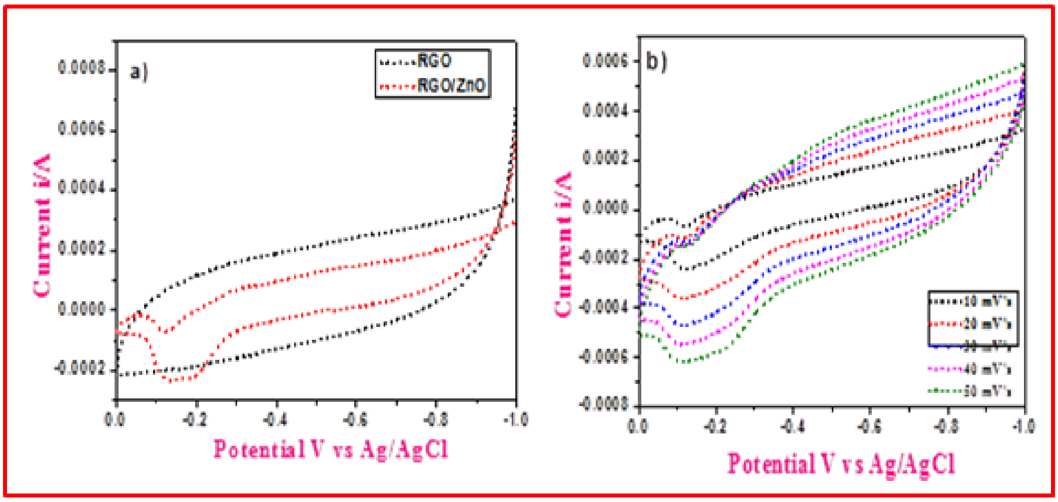

FIG. 2. a) Cyclovoltagramms of RGO and RGO/ZnO; b) different scan rate of RGO/ZnO

TABLE 1. Electrochemical reversibility and EIS of RGO, RGO/ZnO and RGO/Mn_2O_3 electrodes

Electrodes	$\mathbf{E_0(V)}$	$\mathbf{E_R(V)}$	$\mathbf{E_0 - E_R}$	$\mathbf{Rct(\Omega)}$	$\mathbf{C(F) \times 10^{-4}}$
RGO	0.8675	0.4480	0.4195	23.7	0.01
RGO/ZnO	0.3963	0.3077	0.0886	36.74	2.021

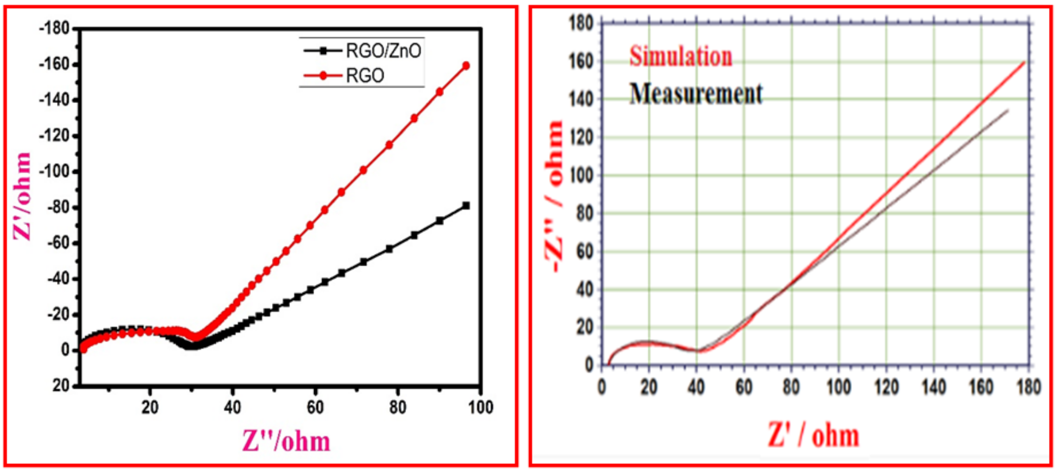

FIG. 3. a) Nyquist plots of RGO and RGO/ZnO; b) fitted simulation of RGO/ZnO

3.3. Photocatalytic Activity

In the existing work, Methylene blue (MB) and Indigo carmine (IC) dyes were used as ideal pollutants to estimate the photocatalytic activity of RGO/ZnO under UV light irradiation [12, 13]. In an experiment, 60 mg of RGO/ZnO was dispersed in 250 ml MB (20 ppm). The mixed suspensions were first magnetically stirred in the dark for 30 min to reach the adsorption–desorption equilibrium. Under ambient conditions and stirring, the mixed suspensions were exposed to visible light irradiation produced by a 400 W metal Philips lamp (wavelength: 254 nm). At certain time intervals, 5 ml aliquots of the mixed suspensions were extracted. The filtrates were analyzed by recording UV–vis spectra of MB and IC using a Spectratreats 3.11.01 Release 2A UV–vis spectrophotometer. In UV light, RGO/ZnO can absorb UV light (254 nm) and generate electron–hole pairs. These photo-generated electron and hole pairs can migrate into the catalyst surface and react with surface adsorbed O_2 to form active oxygen species. The photo degradation of MB and IC by RGO/ZnO nanoparticles and the effect of various parameters, like initial catalyst loading, initial dye concentration etc., were thoroughly investigated. RGO/ZnO nanomaterials exhibited the highest photocatalytic activity.

Figure 4 shows the UV-vis absorption spectra of MB and IC as a function of the catalytic reaction time. Both MB and IC solutions turned colorless after 80 min, indicating complete degradation of the dye molecules by RGO/ZnO. After 80 min of reaction, the RGO/ZnO showed good catalytic degradation of IC. When using the as-prepared composite material, the MB solution with concentration 60 mg/L can be degraded up to 79.9 % and mineralized up to 21 % in 80 minutes, as is shown Fig. 5.

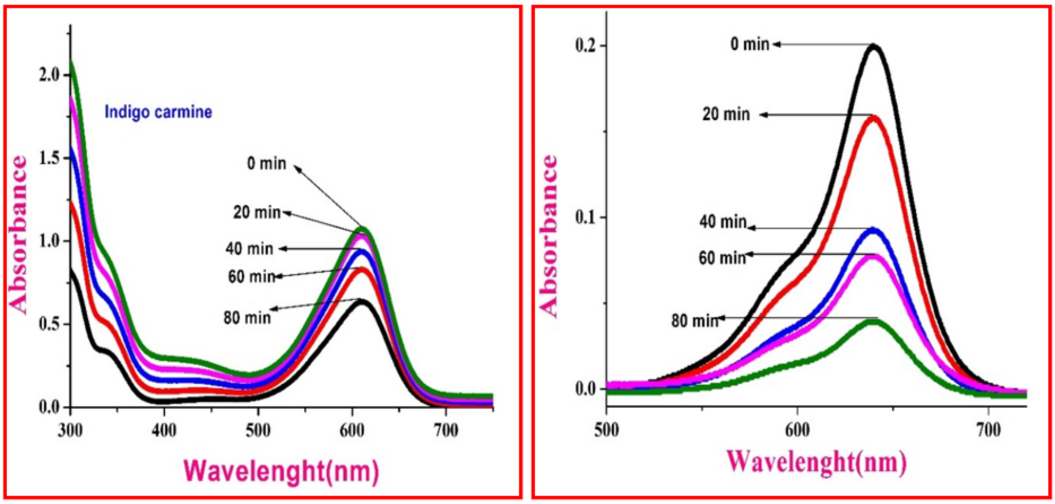

FIG. 4. Time-dependent UV-vis absorption spectra of RGO/ZnO in IC and MB

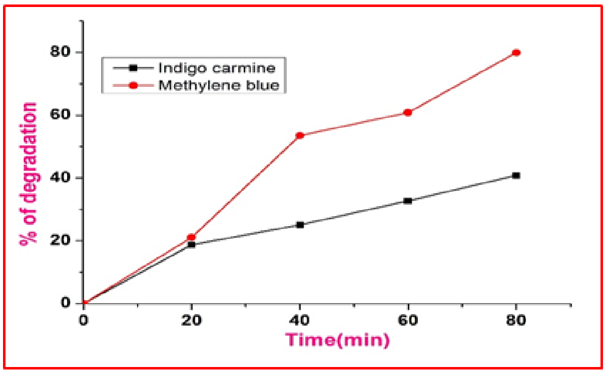

FIG. 5. UV-visible spectra of IC and MB degradation

4. Conclusion

RGO and RGO/ZnO composites were successfully prepared and their applications as electrode materials for electrochemical applications and photocatalytic activities were investigated. Cyclic voltammetry showed ideal capacitive behavior for RGO and RGO/ZnO hybrid nanosheets. Table 1 shows RGO/ZnO having less $E_0 - E_R$ and hence electrochemical reversible reactions will be more, and RGO/Mn_2O_3 having lesser Rct value and hence capacitance will be more. The photocatalytic activity was assessed through UV-Visible spectra, from which, we conclude that RGO/ZnO showed a good catalytic degradation of IC. This test showed that using the as-prepared composite material, the MB solution with concentration 60 mg/L can be degraded up to 79.9 % and mineralized up to 21 % and IC degraded up to 40.85 in 80 minutes.

References

[1] Yuvaraj Haldorai, Walter Voit, Jae-Jin Shim. Nano ZnO @reduced graphene oxide composite for high performance super capacitor. *Green synthesis in supercritical fluid Electrochemical Acta.*, 2014, **120**, P. 65–72.

[2] Ejikeme Raphael Ezeigwe, Michelle T.T. Tan, Poi Sim Khiew, Chiu Wee Siong. One-step green synthesis of graphene/ZnO nanocomposites for electrochemical capacitors. *Ceramics International*, 2015, **41**, P. 715–724.

[3] Zhou Y.K., He B.L., Zhang F.B., Li H.L. Hydrous manganese oxide/carbon nanotube composite electrodes for electrochemical capacitors. *Solid State Electrochem.*, 2004, **8**, P. 482.

[4] Subramanian V., Zhu H., Wei B. Alcohol-assisted room temperature synthesis of different nanostructured manganese oxides and their pseudocapacitance properties in neutral electrolyte. *Chem. Phys. Lett.*, 2008, **453**, P. 242–249.

[5] Zijiong Li, Zhihua Zhou, et al. High-performance solid-state supercapacitors based on graphene-ZnO hybrid nanocomposites. *Nanoscale Research Letters*, 2013, **8**, P. 473.

[6] Li B., Liu T., Wang Y., Wang Z. ZnO/graphene-oxide nanocomposite withremarkably enhanced visible-light-driven photocatalytic performance. *J. Col-loid Interface Sci.*, 2012, **377**, P. 114.

[7] Tingting Liu, Guangjie Shao, Mingtong Ji, Guiling Wang. Synthesis of MnO_2-graphene composites with enhanced super capacitive performance via pulse electrodeposition under supergravity field. *Journal of Solid State Chemistry*, 2014, **215**, P. 160–166.

[8] Xichuan Lia, Xiaoyang Xua, et al. Electrochemically active MnO_2/RGO nanocomposites using Mn powder as the reducing agent of GO and the MnO_2 precursor. *Electro chimica Acta*, 2014, **130**, P. 305–313.

[9] Yongchuan Liu, Dawei He, et al. Synthesis of MnO_2/graphene/carbon nanotube nanostructured ternary composite for supercapacitor electrodes with high rate capability. *Materials Chemistry and Physics*, 2014, **147**, P. 141–146.

[10] Conway B.E. *Electrochemical Supercapacitors: Scientific Fundamentals and Technological Applications*. Kluwer Academic/Plenum, New York, 1999.

[11] Muhammad Mohsin Hossaina, Bon-Cheol Kub, Jae Ryang Hahna. Synthesis of an efficient white-light photo catalyst composite of graphene and ZnO nanoparticles: Application to methylene blue dye decomposition. *Applied Surface Science*, 2015, **354**, P. 55–65.

[12] Prathap Anu M.U., Kaur B., Srivastava R. Hydrothermal synthesis of CuO micro-/nanostructures and their applications in the oxidative degradation of methylene blue and non-enzymatic sensing of glucose/H_2O_2. *J. Colloid Interface Sci.*, 2012, **370**, P. 144–154.

[13] SiXu Deng, Dan Sun, et al. Synthesis and electrochemical properties of MnO_2 nanorods/graphene composites for supercapacitor applications. *Electrochimica Acta*, 2013, **111**, P. 707–712.

NANOSYSTEMS: PHYSICS, CHEMISTRY, MATHEMATICS, 2016, 7 (4), P. 683–686

Characterization studies on the novel mixed thin films

P. Ramasundari[1], S. Ganeshan[2] and R. Vijayalakshmi[3]

[1]P. G. & Research Department of Physics, S. V. N. College, Madurai, India
[2]Department of Physics, Vivekananda College, Madurai, India
[3]P. G. & Research Department of Physics, Thiagarajar. College, Madurai, India

ramprof62@gmail.com, ramyarv@rediffmail.com

PACS 68 **DOI 10.17586/2220-8054-2016-7-4-683-686**

Among electrochemical processes having a considerable impact on technical development, the mixed thin film (Mo-Ni oxide) plays an important role, due to its better mechanical, anticorrosive and thermal stability characteristics. The mixed films have been prepared by dip spin coating. The films are grown on substrates like Indium Tin Oxide (ITO) and are well adherent on the substrates, pinhole free and transparent. The X-ray diffraction analysis of the films confirms they are polycrystalline in nature. The morphological study reveals that the uniform distributions have flower-like structure. From the compositional analysis, the EDAX spectra show the presence of molybdenum and nickel. The optical band gap was found to be 1.36 eV and band assignments for Fourier Transform Infrared (FTIR) spectra are comparable to reported values.

Keywords: Dip Spin Coating, EDAX, SEM, X-Ray Diffraction.

Received: 5 February 2016

Revised: 27 April 2016

1. Introduction

The optical properties of thin films are very important for many applications. Researchers have shown considerable interest in Ni–Mo oxide films, because of their applications such as hydrogen evolution catalysis [1,2] and anticorrosion treatment [3]. Transition metal oxides, like nickel oxides have found application due to their anti-ferromagnetic semiconducting properties with a wide band gap of 3.6 eV [4,5]. This provides opportunities for use in electrochromic devices [6], fuel cells [7] or other applications. Electrodeposition-prepared transition metal oxide films exhibit good electrochromic properties. For electrodeposited Mo–Ni oxide films, it has been shown that as Mo content increases, certain peaks in XRD broaden and disappear due to a decrease in grain size [8, 9]. Even though there are reports for the optical properties, structural characteristics, band assignments and electrical properties by dip spin coating Indium Tin Oxide (ITO) plates, values are reported only for Indium Tin Oxide (ITO) substrates in this paper.

2. Experimental

The concentrations of 0.05 N (of MoO_3 and $NiSO_4$ mixture) at 330 K by dip spin coating under optimized conditions. The coating was performed at 3000 rpm for 30 mins as optimized parameters to obtain the mixed oxide thin film. The coated samples were investigated by conventional XRD with CuKα radiation using XPERT-PRO diffractometer. FTIR measurements in the range of 400 – 4000 cm^{-1} were carried out by JASCO CANVAS. The SEM photographs were recorded using HITACHI S-3400.

3. Results and Discussion

3.1. XRD Analysis

The structural properties of these films were analyzed by the X-ray diffractometer. Fig. 1 shows the diffraction pattern of Mo–Ni mixed oxide thin film which is deposited on the Indium Tin Oxide (ITO) plate. From the surface analysis, it was found that the mixed thin films exhibit uniform thickness. The diffracting angles were set to 20 ° to 80 ° with a low scanning speed and in continuous mode. Diffraction peaks were observed at $2\theta = 28.450$, 39.430, 44.720, 47.320 and 65.560, corresponding to the (0 0 2), (-2 -2 2), (1 2 2), (1 -1 3), (-1 -5 1) planes of the mixed thin films respectively. XRD pattern of Mo–Ni mixed oxide thin films showed polycrystalline wurzite structure with a preferential (1 2 2) orientation peak and the peaks are comparable to reported values [10].

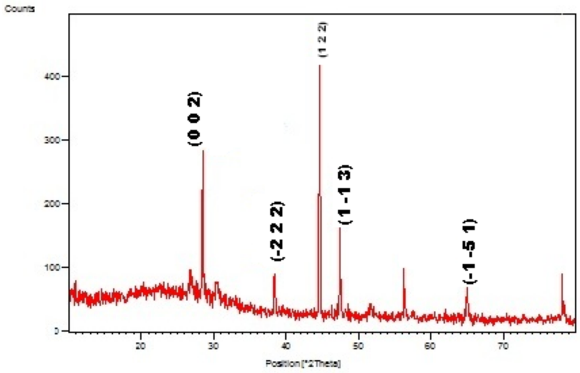

FIG. 1. XRD pattern of as deposited Mo–Ni oxide film on ITO substrate

3.2. SEM Analysis

The film deposited on the Indium Tin Oxide (ITO) substrate showed flower-like structure. The EDAX, which was used in conjunction with SEM, confirmed the elemental composition of the film as deposited on the substrate, revealing the presence of molybdenum and nickel (89.52 % Mo & 5.42 % Ni) as well as impurities like copper and zinc.

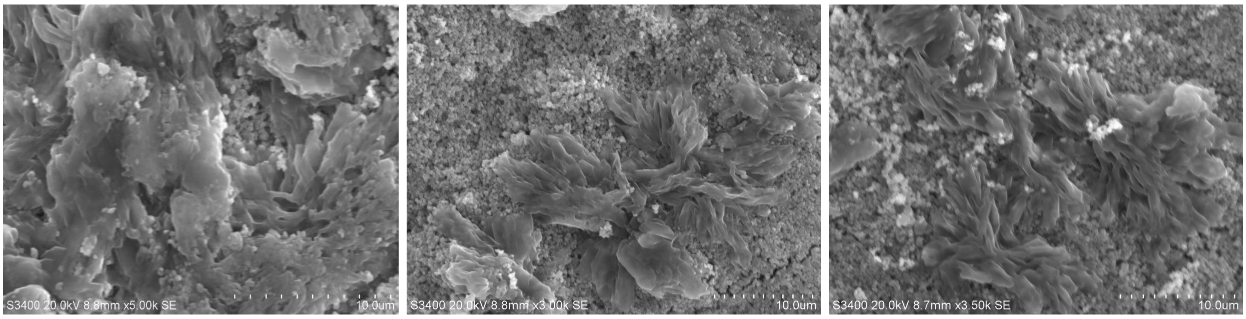

FIG. 2. SEM images of as deposited Mo–Ni oxide film on ITO substrate

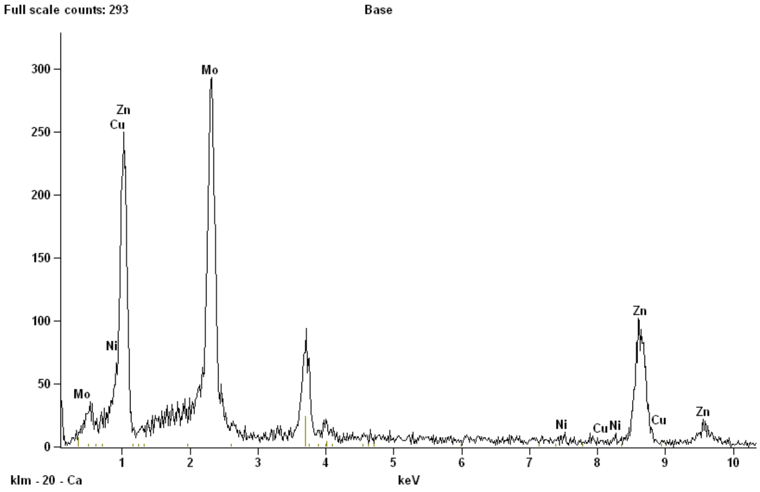

FIG. 3. EDAX spectra of as deposited mixed Mo–Ni oxide film on ITO substrate

3.3. FTIR Spectra

Fourier transform infrared spectroscopy provides information about a particular compound's functional groups, molecular geometry and inter/intramolecular interactions. The bands at 3425 cm^{-1}, 1614 cm^{-1} in Fig. 4 were attributed to the surface absorbed water in the mixed Mo–Ni oxide thin films. The band 3780 cm^{-1} and 3932 cm^{-1} are due to O–H stretching vibrations of water molecules. The vibration absorption peaks at 875 cm^{-1} were due to Mo–O–Mo stretching [11].

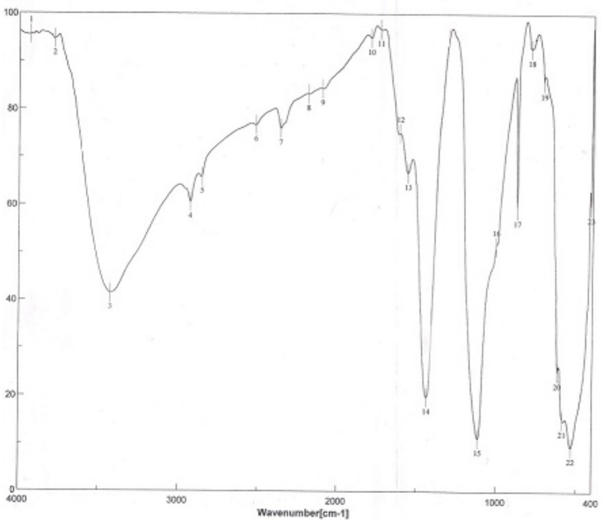

FIG. 4. FTIR Spectra of as deposited mixed Mo–Ni oxide film

3.4. Optical Studies

Optical absorption characterisitcs were studied in the 200 – 1100 nm range. The absorption spectrum for the as-deposited mixed Mo–Ni oxide film is shown in Fig. 5. The UV-Visible spectrum shows a sharp peak centered at 360 – 376 nm with a long tail towards longer wavelength side. Absorption has very high value in the UV region and decreases with increasing wavelength, becoming constant towards the visible region, which indicates a high transparency in the visible region. The optical band gap of mixed Mo-Ni thin film was found to be 1.36 eV.

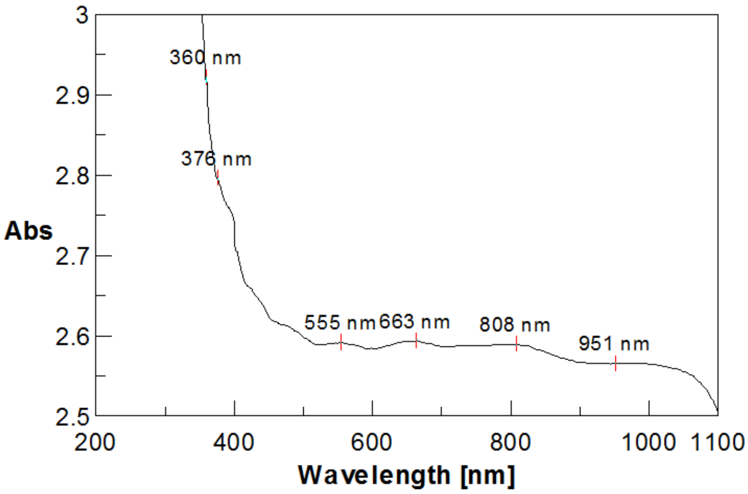

FIG. 5. Absorprtion Spectra for as deposited mixed Mo–Ni oxide film on ITO substrate

4. Conculsion

Electrochromic materials, like mixed Mo–Ni oxide thin film, were deposited on ITO under optimized conditions. The dip spin coated films are white in color and are transparent. The films are well adherent on the substrates, pinhole-free and transparent. X-ray diffraction shows that the films are polycrystalline in nature and are comparable to JCPDS data. SEM images reveal that the films are without any pinholes or cracks and cover the substrate well. The optical absorption spectrum reveals that the material has a direct band gap nature and its energy is in agreement with the reported values.

References

[1] Mihailov L., Spassov T., Kanazirski I., Tsvetnaov I. Electrocatalytic behavior of Ni-based amorphous alloys for hydrogen evolution. *J. Mater. Sci.*, 2011, **46**, P. 7068–7073.

[2] Kirk D.W., Thorpe S.J., Suzuki H. Ni-base amorphous alloys as electrocatylst for alkaline water electrolysis. *Int. J. Hydrogen Energy*, 1997, **22**, P. 493–500.

[3] Chassaing E.E., Portail N.N., Levy A.F., Wang G. Electrodeposition and Characterization of Nanocrystalline Ni-Mo Catalysts for Hydrogen Production. *J. Appl. Electrochem.*, 2004, **34**, P. 1085–1091.

[4] Adler D., Fainleb J.J. Electrical and optical properties of 'Narrow?Band Materials'. *Phys. Rev. B*, 1970, **2** (8), P. 3112–3134.

[5] Zollner M., Kipp S., Becker K.D. Reactive Processes of Nickel Oxide on oxidic Substrates as observed by Scanning Force Microscopy. *Crystal Research and Technology*, 2000, **35** (3), P. 299–305.

[6] Purushothaman K.K., Muralidharan G. Nanostructured NiO Based All Solidstate electrochromicdevice. *Journal of Sol-Gel Science and Technology*, 2008, **46**, P. 190–197.

[7] Shaigan N., Ivey D.G., Chen W. Metal?Oxide Scale Interfacial Imperfections and Performance of Stainless Steels Utilised as interconnects in Solid Oxide Fuel cells. *Journal of The Electrochemical Society*, 2009, **156** (6), P. 765–770.

[8] Beltowaka-Lehman E., Bigos A., Indykaand P. Electrodeposition and characterisation of nanocrystalline Ni-Mo coatings. *Surf. Coat. Technol.*, 2012, **211**, P. 67–71.

[9] Beltowaka-Lehman E., Indyka P.P. Kinetics of Ni-Mo electrodepsotion from Ni-rich citrate baths. *Thin Solid Films*, 2012, **520**, P. 2046.

[10] Masatoshi Saitou. Characterization of Electrodeposited Ni and Ni?Mo Thin Films by X-ray Diffraction. *Int. J. Electrochem. Sci.*, 2014, **9**, P. 6033–6042.

[11] Sulma Marisela Fernandez-Valverde, Eduardo Ordonez-reqil, Gerardo cabanas-Moreno, Omar Solorza-feria. Electrochemical Behavior of Ni-Mo Electrocatalyst for Water Electrolysis. *J. Mex. Chem. Soc.*, 2010, **54** (3), P. 169–174.

NANOSYSTEMS: PHYSICS, CHEMISTRY, MATHEMATICS, 2016, 7 (4), P. 687–690

Optical and structural studies of vanadium pentoxide thin films

S. Ganeshan[1], P. Ramasundari[2], A. Elangovan[3] and R. Vijayalakshmi[4]

[1]Department of Physics, Vivekananda College, Madurai
[2]P. G. & Research Department of Physics, S. V. N. College, Madurai
[3]P. G. & Research Department of Chemistry, Thiagarajar College, Madurai
[4]P. G. & Research Department of Physics, Thiagarajar College, Madurai
sganeshanmdu@gmail.com, ramyarv@rediffmail.com

PACS 81.15 Pq, 74.25 Gz, 61.05 Cp **DOI 10.17586/2220-8054-2016-7-4-687-690**

Recently, transition metal oxides like Vanadium pentoxide have become a subject of intensive studies. The particular physical and chemical properties of these materials allow a wide range of practical applications such as electrochromic devices, cathode electrodes for lithium batteries, humidity sensors. The V_2O_5 film was prepared by an electrodeposition technique. The structural and optical properties were studied by X-Ray Diffraction (XRD), scanning electron microscopy (SEM), UV-Visible and Fourier Transform Infrared Spectroscopy (FT-IR). XRD spectra recorded has been observed and compared with the JCPDS values. SEM images showed very smooth surface morphology and the elemental compositions of the film were confirmed by EDAX. The transmittance of the V_2O_5 films showed 75 % at 425 nm for the as-deposited substrate. The energy band gap of the films was found to be 2.45 eV and the band assignments of the V_2O_5 film are comparable with the reported values.

Keywords: Electrodeposition, optical properties, X-ray diffraction.

Received: 5 February 2016

Revised: 11 May 2016

1. Introduction

V_2O_5 is an important material among other transition metal oxides from the view point of its novel electronic and optical characteristics in thin film form, leading to applications in lithium solid state micro batteries, gas sensors and electrochromic display devices [1,2].The vanadium-oxygen system has been intensively studied by theoretical and experimental techniques. Vanadium oxide is used in thermal sensing and switching. Vanadium pentoxide films have been prepared using various physical and chemical techniques, such as thermal evaporation, electron beam evaporation, sol-gel, electrochemical deposition and pulsed laser ablation [3–6]. Some unique features of V_2O_5 include its orthorhombic layered structure, high electrochromic activity, high stability and ease of thin film formation by numerous deposition techniques. Among the various preparation methods, the electrodeposition method was one of the simplest methods, due to its deposition rate, good uniformity on the substrates and thickness control of the film. The main advantage of this electrodeposition coating is the conformal resist layer, independent of the substrate geometry. Electrodeposition coating is the most suited technique to pattern structures that run in and across cavities or when a smaller line width is required. In this present work, the films were prepared by an electrodeposition technique and were characterized to study the optical and structural properties using XRD, SEM with EDAX, UV-Vis Spectroscopy and FT-IR Spectra.

2. Experimental

In electrodeposition techniques, structurally and compositionally-modulated alloys and compounds can be deposited and the deposition can be carried out at room temperature enabling the formation of the semiconductor junctions without interdiffusion. The V_2O_5 films were prepared by electrodeposition technique having a bath 0.2 M of vanadium pentoxide powder mixed with hydrogen peroxide which was used as the stock solution. The parameters like the concentration of the solution, pH, current and temperature were optimized. The electrodeposition process was carried out with three electrode systems, one is ITO coated plate acting as working electrode, the other the platinum electrode as counter electrode and the third one was the saturated calomel electrode (SCE) as the reference electrode. Two grams of vanadium pentoxide of 99 % purity and 30 % of sulfuric acid were added to avoid the effervescence produced in the solution. Then the stock solution was diluted to get the concentration of 0.1 M. The pH of the solution was maintained as 3.0 and the deposition current was fixed as 1 mA and the temperature maintained at the room temperature. The crystallographic structure of the film was determined from Powder X-ray diffraction patterns obtained by using BRUKER ECO D8 Advance diffractometer with a monochromatic

CuKα radiation ($\lambda = 0.15406$ nm , 40 kV, 20 mA). The surface morphology was studied using SEM (BRUKER ECO D8 ZEISS). The Compositional analysis was done using EDAX spectrometer attached to SEM. The optical transmission studies were done using UV-Vis Spectrophotometer (HP2000). FTIR Spectra were obtained from Perkin-Elmer make model spectrum RXI spectrophotometer.

3. Results and discussion

3.1. XRD Analysis

Figure 1 shows the diffraction pattern of V_2O_5 thin film which was deposited on the ITO substrate. From the analysis, it was found that the V_2O_5 film exhibited uniform thickness [7, 8]. The XRD analysis proves that the V_2O_5 films exhibit polycrystalline nature and the diffraction peaks for (2 2 0), (3 2 0) and (3 0 1) planes were prominent. The other low intensity peaks showed that the as-deposited film has coarsely fine crystallites and nanocrystallites. Sharp diffraction peaks at positions $2\theta = 22.4$ °, 27.14 ° and 52.22 ° correspond to the (2 2 0), (3 2 0) and (3 0 1) planes respectively. The XRD pattern suggests that the film is polycrystalline with varying degree of orientation and has FCC structure when compared with the JCPDS (03-0206) value. The smoothness of the XRD pattern confirms the uniformity in the grown film. The average particle size, which was calculated using the Scherrer relation, ranges from 28.21 nm to 30.81 nm.

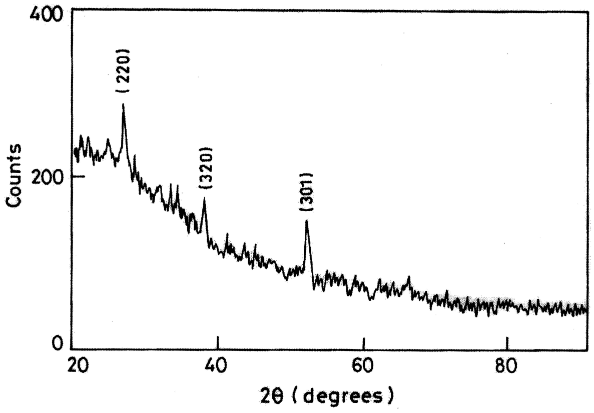

FIG. 1. XRD pattern images of V_2O_5 film on ITO substrate

3.2. Surface morphology studies: SEM with EDAX

The microstructure and morphology analysis of the as-deposited V_2O_5 thin film was carried out. The SEM image in Fig. 2 shows that the film is nearly homogeneous without any pinholes or cracks and covers the substrate well. The particles are spherical in shape. The particle size observed from the SEM images was of the order of 100 – 200 nm [9]. Fig. 3 shows the elemental composition of the as deposited V_2O_5 film. The presence of vanadium and oxygen were confirmed by EDAX analysis and their atomic weight percentages are calculated as 10.45 % and 28.33 % for vanadium and oxygen respectively.

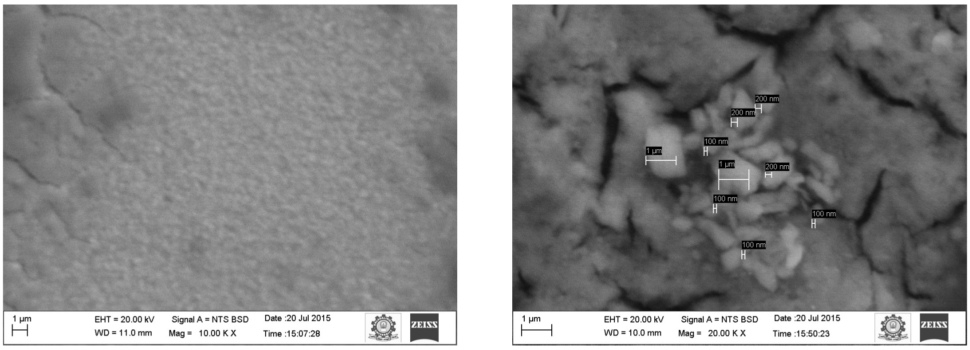

FIG. 2. SEM images of as deposited V_2O_5 film on ITO substrate

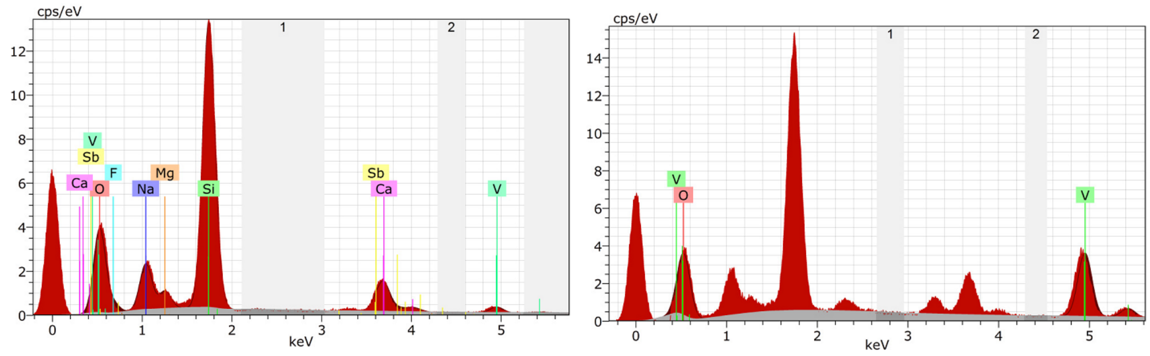

FIG. 3. EDAX spectra of as deposited V_2O_5 film on ITO substrate

3.3. FTIR

The FTIR spectrum of V_2O_5 film is portrayed in Fig. 4. FTIR investigation was performed to study the structural changes and band stretching of vanadium pentoxide. The band at 841 cm^{-1} corresponds to the polycrystalline V_2O_5 also the band at 814 cm^{-1} is assigned to the crystalline V_2O_5. A shoulder type of vanadium band is observed at 767 cm^{-1} and bands located at 530 cm^{-1}, 521 cm^{-1} are assigned to the stretching mode of the oxygen which is shared between 3 vanadium atoms. The band at 431 cm^{-1} is assigned to the bending vibrations of the bound oxygen which is shared by 2 vanadium atoms [10, 11].

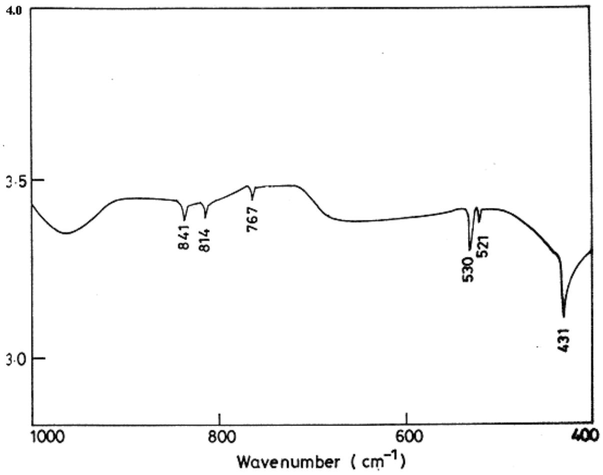

FIG. 4. FTIR Spectra of the V_2O_5 film

3.4. Optical studies

The UV-VIS spectrum measured for V_2O_5 film is shown in Fig. 5(b) and the band gap calculated from Fig. 5(a). The optical parameters are calculated from the transmittance spectrum in the 300 nm to 800 nm wavelength region. The as-deposited film has a steady transmittance of 75 % in the visible region. The oscillations in the curves were due to interference effects that depend on the film thickness and the refractive index. The plot is linear, indicating a direct optical transition and the evaluated energy gap is 2.45 eV, which agrees with the reported values [12, 13] and is similar to the value reported in the pulsed laser deposition technique [13]. Given this data, one can say that a high quality V_2O_5 thin film was obtained using the electrodeposition method.

4. Conclusion

Polycrystalline V_2O_5 thin films were deposited on ITO substrate by electrodeposition method and the films were well adherent, uniform and pinhole-free. The XRD pattern of the V_2O_5 film showed a polycrystalline nature with a preferential (3 0 1) orientation. Morphological studies showed a well-defined structure and elemental composition. The optical band gap of the V_2O_5 thin film was found to be 2.45 eV. The electrochromic studies and coloration efficiency of the vanadium pentoxide thin films are areas for future exploration.

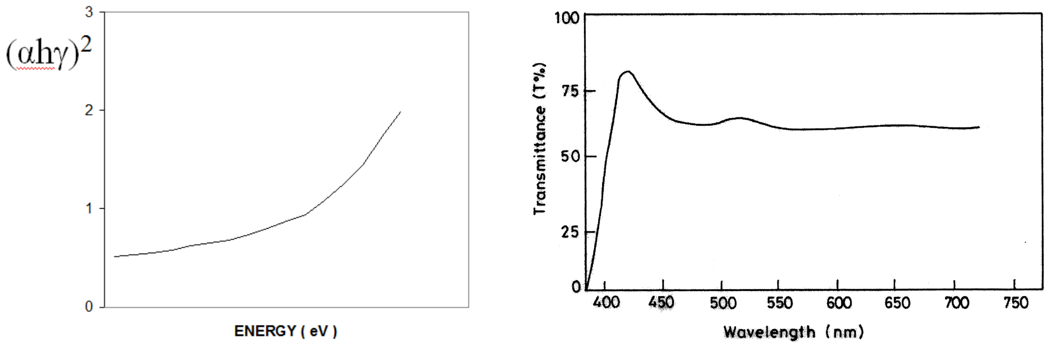

FIG. 5. (a) $(\alpha h\gamma)^2$ versus Photon energy film for V_2O_5 thin film; (b) Transmittance curve for V_2O_5 thin film

References

[1] Julien C. Electrochemical properties of disordered cathode materials. *Ionics*, 1996, **2** (3-4), P. 169–178 .

[2] Ramana C.V., Hussain O.M., Srinivasulu Naidu B., Reddy P. Influence of substrate temperature on the composition and structural properties of electron beam evaporated V_2O_5 thin films. *J. Vaccum*, 1997, **48** (5), P. 431–434.

[3] Bates J.B., Dudney N.J., et al. Fabrication and characterization of amorphous lithium electrolyte thin films and rechargeable thin-film batteries. *J. Power Sources*, 1993, **43**, P. 103–110.

[4] Moshfegh A.Z., Ignatiev A. Formation and characterization of thin film vanadium oxides: Auger electron spectroscopy, X-ray photoelectron spectroscopy, X-ray diffraction, scanning electron microscopy, and optical reflectance studies. *Thin Solid films*, 1991, **198** (1), P. 251–268.

[5] Bouzidi A., Benramdane N., et al. Physical Properties of V_2O_5 sprayed films. *Mater. Sci. Eng. B*, 2002, **95**, P. 141–147.

[6] Julien C., Haro-Poniatowski E., et al. Growth of V_2O_5 thin films by pulsed laser deposition and their applications in lithium microbatteries. *Mater. Sci. Eng. B*, 1999, **65** (3), P. 170–176.

[7] Ramana C.V., Smith R.J., et al. Correlation between Growth Conditions, Microstructure, and Optical Properties in Pulsed-Laser-Deposited V_2O_5 Thin Films. *Chem. Matter*, 2005, **17** (5), P. 1213–1219.

[8] Shiho lwanaga, Darling R.B., Cooden D.H. Stable and erasable patterning of vanadium pentoxide thin films by atomic force microscope nanolithography. *Appl. Physics*, 2005, **86**, P. 133113.

[9] Olivetti E.A., Kim J.H., et al. Sol-Gel syntheis of Vanadium oxide within a block copolymer matrix. *Chem. Matt.*, 2006, **18**, P. 2828–2833.

[10] Culea E., Nicula A.L., Bratu I. An infrared study of $xV_2O_5 \cdot (1?x)B_2O_3$ glasses. *Phys. Status. Solid*, 1984, **83** (1), K15–K18.

[11] Abello L., Husson E., Repelin Y., Lucazeau G. Vibrational spectra and valence force field of crystalline V_2O_5. *Spectrochimica Acta Part A: Molecular Spectroscopy*, 1983, **39** (7), P. 641–651.

[12] Madhuri K.V.,Srinivasa rao K., et al. Optical and electrical properties of $(V_2O_5)_{1-x}$–$(MoO_3)_x$ thin films. *J. Indian Inst. Sci.*, 2001, **81**, P. 653–658.

[13] Ramana C.V., Naidu B.S., Hussain O.M., Pinto R. Low temperature growth of Vanadium pentoxide thin films produced by Pulsed Laser ablation. *J. Phys. D: Appl. Phys.*, 2001, **34**, L35–L38.

NANOSYSTEMS: PHYSICS, CHEMISTRY, MATHEMATICS, 2016, 7 (4), P. 691–694

Optically tuned poly (3-hexylthiophene-2,5-diyl) P3HT/PCBM (modified fullerene) blend for plastic solar cell

Ishwar Naik[1]*, Rajashekhar Bhajantri[2], Lohit Naik[2], B. S. Patil[3], Ullas shetti Pragasam[1],
Sunil Rathod[4], Jagadeesh Naik[4]

[1]Govt. Arts & Science College, Karwar, India
[2]Dept. of Physics, Karnatak University, Dharwad, India
[3]Govt. First Grade College Poojgeri, Ankola, India
[4]Dept. of Physics, Mangalore University, Mangalore, India

*iknaik@rediffmail.com, rfbhajantri@gmail.com

PACS 73.61.Ph; 73.50.Pz; 81.01.Fb; 81.05.ub; 82.35.Cd; 83.80.Tc

DOI 10.17586/2220-8054-2016-7-4-691-694

Nanotechnology-assisted organic electronics is a wide-spread and promising research field at present in the search for an efficient solar cell. The strong absorption spectra of the donor polymer poly[3-hexylthiophene-2,5-diyl)(P3HT) in the visible region and the prominent absorption of the acceptor [6,6]-phenyl C_{61} butyric acid methyl ester(PCBM) in UV region have proved them to be the most popular donor-acceptor pair for preparing photoactive materials. The active blend, having a broad absorption spectrum, is the primary requisite for an efficient solar cell. The present work is focused on optimizing the photoactive blend of (P3HT)) and PCBM for the maximum absorption of the solar energy. P3HT: PCBM blends of weight ratio 3:1, 1:1 & 1:3 were prepared in xylene as the solvent and glass coated samples are prepared by solution cast method. Samples were characterized by JASCO UV Vis NIR V 670 spectrometer. P3HT has strong absorption in the visible region, while PCBM has an effective absorption in the UV region with broad tail of absorption extending up to 800 nm. The spectrum for the blend is a superposition of the spectra of the component moieties. The 1:3 blend of P3HT with PCBM has broad spectral sensitivity for absorption and can be used as the best photoactive blend for construction of a plastic solar cell. The energy difference (band gap) between Highest Occupied Molecular Orbital (HOMO) and the Lowest Un-occupied Molecular Orbital (LUMO) of the samples were determined through Tauc's plot. Calculations from Tauc's plot indicated that pure P3HT sample has an onset wavelength of 640 nm with a band gap of 1.93 eV. The onset wavelengths for 3:1 & 1:1 blends are almost same of about 632 nm with a band gap of 1.96 eV. The optimized blend 1:3 sample has the onset wavelength 653 nm with the least energy gap 1.9 eV.The absorption by the blend can be further enhanced by either dye sensitization or plasmon resonance.

Keywords: P3HT, PCBM, HOMO, LUMO, LSPR.

Received: 5 February 2016

1. Introduction

First generation silicon-based solar cells are are hindered by material cost, installation cost, and fabrication complications. Even the second generation thin film solar cells are also not economical [1]. Plastic solar cells are promising because of their low cost, simple processing and flexibility. Since efficiency is the main drawback of these solar cells, the search for an efficient plastic solar cell has become a global challenge at present in the field of plastic electronics. The physics involved in the energy conversion efficiency of polymer cells is a multistep process, including photon absorption, exciton formation and migration, exciton dissociation, charge transport and charge collection [2]. The bulk heterojunction concept of the donor-acceptor system has provided remarkable progress in the efficiency enhancement in this regard. The exciton diffusion mechanism and the charge collection rate have been significantly increased due to the formation of number of hetero P-N junctions in the blend. The photoactive blend must be properly tuned with respect to the choice of donor-acceptor pair as well as their weight percentage combination to have a broad solar spectral response. Among the conducting polymers, P3HT has the absorption spectrum matching well with the strongest solar spectrum and also has good transport properties. The present work is focused on the preparation of an optimized active blend of the widely used donor polymer Poly[3-hexylthiophene-2,5-dily) (P3HT) and N-type acceptor [6,6]-Phenyl C_{61} butyric acid methyl ester (PCBM), a modified fullerene. The strong absorption spectrum of P3HT in the visible region and the prominent absorption of PCBM in the UV region, along with the broad tail of absorption beyond the visible region are the key factors in selecting them as the donor-acceptor pair. The resulting active blend must show broad spectral absorption extending from the UV to the region beyond the visible for a proper composition between them. Blends of different donor-acceptor weight ratios were prepared in the high boiling point solvent xylene and their glass coated samples (solution cast method) were characterized by UV-Visible spectra. The blend showing broad spectral sensitivity for absorption is selected as the best photoactive blend.

2. Experimental

The P-type donor polymer P3HT (electronic grade, average mol wt 15000 – 45000, HOMO 5 eV, LUMO 3 eV) and N-type acceptor PCBM (functionalized Fullerene, HOMO 6.1 eV,LUMO 3.7 eV) were purchased from Sigma Aldrich Corporation. The solvent xylene was obtained from Rankem Chemicals. These chemicals are used as received without further purification. The chemical structures of these donor and acceptor molecules are as shown below.

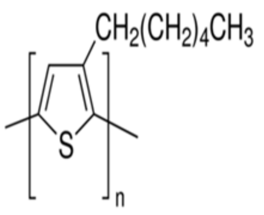

P3HT

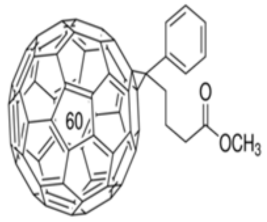

PCBM

10 mg of P3HT and 10 mg of PCBM were dissolved in 100ml of xylene in separate beakers and magnetically stirred for 48 hrs at room temperature until clear solutions were formed. The resulting solutions were of concentrations 0.1 mg/ml each. The solutions were blended with P3HT: PCBM at weight ratios of 3:1, 1:1 & 1:3 keeping the total weight of the film fixed at 4 mg. The mixtures were magnetically stirred for 3 days at room temperature and then transferred to 3 cm diameter petri-plates, dried at room temperature and then at about 50 °C in hot air oven. The film composition is as shown in Table 1.

TABLE 1. Weight proportions of blends

P3HT/Xylene (P type)	PCBM/Xylene (N type)	P:N
4 mg	0 mg	Pure P
3 mg	1 mg	3:1
2 mg	2 mg	1:1
1 mg	3 mg	1:3
0 mg	4 mg	Pure N

3. Result and discussion

One of the major problems in polymer solar cells is insufficient absorption in the solar irradiation spectrum. Even the widely studied phenylene-vinylene polymers have band edges at 550 nm [2]. However, the pure P3HT film has absorption extending from 300 nm to 640 nm. The spectrum has two peaks at 520 nm and 560 nm with one shoulder around 620nm, having onset of absorption (the absorption edge) at about 640 nm, matching well with the strongest solar spectrum (Fig. 1(a)). The first two peaks arise from π – π^* transition and the shoulder is due to interchain interactions [2]. Pure PCBM shows the strongest absorption in the UV region with a broad tail of absorption extending up to 800 nm (Fig. 1(e)). The strong absorption in the UV region arises from HOMO-LUMO (Highest Occupied Molecular Orbital-Lowest Unoccupied Molecular Orbital) transitions [3] or in other words the strongest absorption is attributed to the formation of higher excited singlet states [4]. The spectra are in good agreement with previously reported results. Spectra for all other blends are the superposition of the component spectra. The effect of PCBM in the blend is to reduce the absorption of P3HT in the visible region followed by increase of absorption in UV region and beyond 650 nm. The modification in the spectrum is because of the interaction between PCBM molecules and P3HT polymer chain. Modified fullerene molecules hinder the interaction among the P3HT chains [5]. Although the 3:1 and 1:1 blends have enough absorption in the visible region as indicated Fig. 1(b) and Fig. 1(c) respectively, the absorption coefficient of 1:3 blend is greater in the UV region and beyond 640 nm as depicted in Fig. 1(d). Relatively, the 1:3 blend has wide spectral sensitivity (Fig. 1(f)) and can be considered as the best photoactive blend among the samples prepared. Pure P3HT sample has onset wavelength of 640 nm with a band gap of 1.93 eV as calculated from Fig. 2(a). Onset wavelengths for 3:1 & 1:1 blends are almost same of about 632 nm with a band gap of 1.96 eV as revealed by Fig. 2(b) and Fig. 2(c). The calculations from Tauc's plot shows that the onset wavelength of the optimized blend is 653 nm with band gap 1.9 eV in accordance with Fig. 2(d). The absorption by the blend can be further enhanced by doping with metal nano particles, exploiting Localised Surface Plsmon Resonance (LSPR) or by dye sensitization. Nanodoping/dye sensitization of 1:3 P3HT: PCBM blend and construction of solar cell using the same is our work in progress.

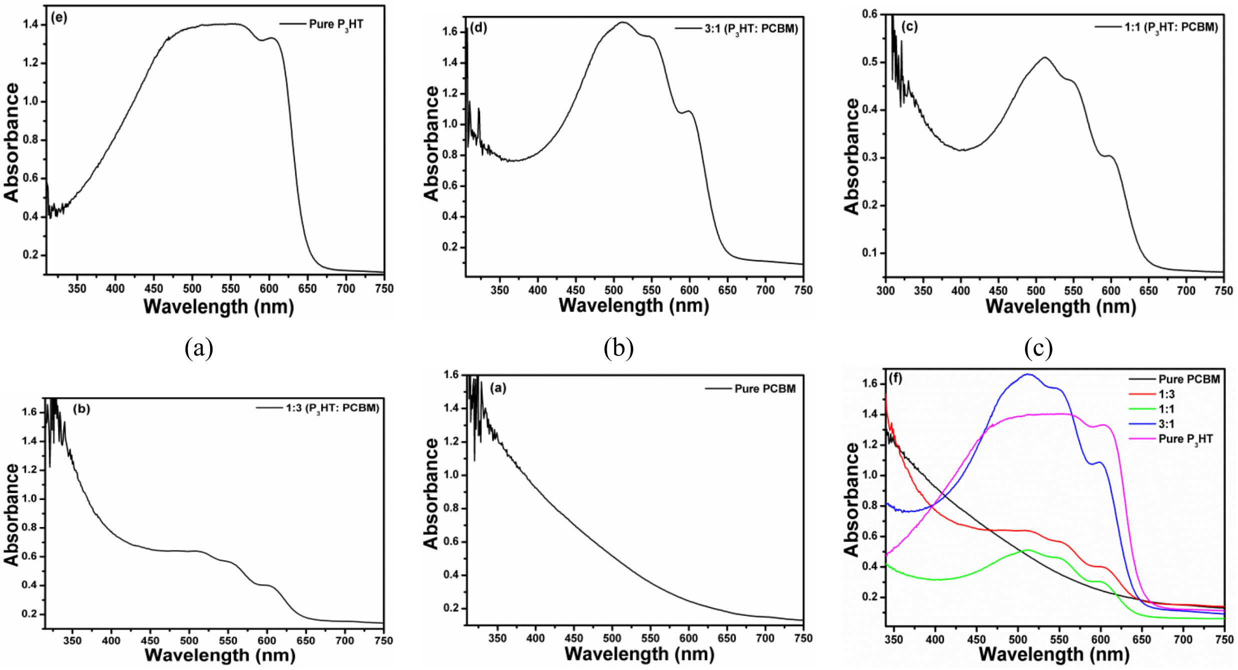

(a) (b) (c)

(d) (e) (f)

FIG. 1. Spectrum of pure P3HT film (a); 3:1 (b); 1:1 (c); 1:3 (d) P3HT:PCBM; pure PCBM (e) and overlay spectra of all films (f)

4. Conclusion

We have investigated the UV-VISIBLE absorption spectra for 3:1, 1:1, 1:3 blends of P3HT:PCBM mixed p-n junction photoactive material along with their pristine glass coated films. Spectral analysis indicated that increased weight percentage of PCBM in the blend broadened the spectral region of absorption. The 1:3 blend of P3HT:PCBM showed broad spectral absorption and was selected as the best photoactive blend. The optimized blend had the smallest band gap (1.9 eV). By doping the blend with metal oxide nanoparticles or by dye sensitization, the absorption can be further enhanced. Exploiting Plasmon Resonance through nanodoping of the selected blend is an area for future investigation. Additionally, there are plans for dye sensitization of the active blend which are being explored. Finally, we conclude that the 1:3 blend of P3HT:PCBM can be used as a photoactive material for constructing a plastic solar cell and the construction of this solar cell is progressing.

Acknowledgements

Thanks to UGC for sanctioning the Minor research project entitled 'construction and characterization of an organic solar cell (OPV) devised from a self-made low cost spin coating machine'. Order No. 1419-MRP/14-15/KAKA088/UGC-SWRO, dated 04-02-2015.

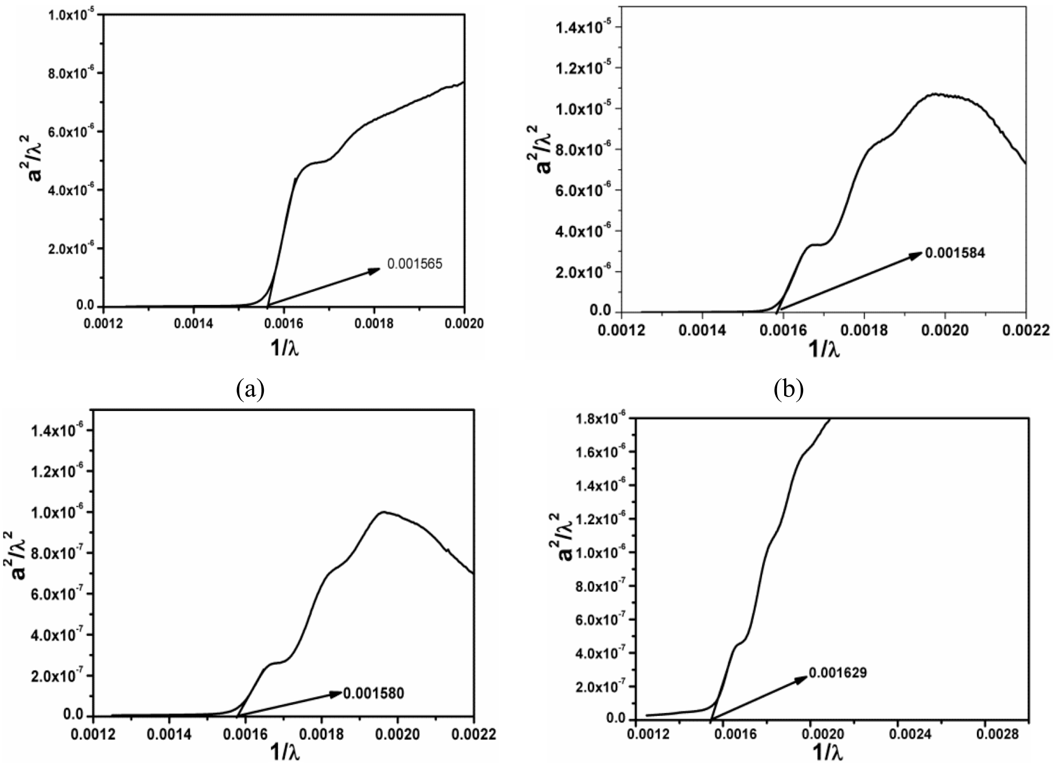

(a) (b)

(c) (d)

FIG. 2. Tauc's plot for pure P (a); 3:1 P:N (b); 1:1 P:N (c); 1:3 P:N (d)

References

[1] Ritesh Tipnis, Darin Laird, Mathew Mathai. Polymer-based Materials for Printed Electronics: Enabling High Efficiency Solar Power and Lighting. *Material Matters*, 2008, **3** (4), P. 92.

[2] Li G., Vishal Shrotriya, et al. Manipulating regioregular poly (3-hexylthiophene):[6,6]-phenyl-C_{61}-butyric acid methyl ester blends?route towards high efficiency polymer solar cells. *Journal of Materials Chemistry*, 2007, **17**, P. 3126–3140.

[3] Mohamad K.A., Afishah Alias, et al. Mixed P3HT/PCBM Organic Thin-Film Transistors: Relation between Morphology and Electrical Characteristics. *J. Chem. Chem. Eng.*, 2014, **8**, P. 476–481.

[4] Hummelen(Kees) J.C. Improved fullerene materials for plastic photovoltaics. `http://www.rug.nl/msc/research/groups/molecularMaterialsDevices`.

[5] Chirvase D., Parisi J., Hummelen J.C., Dyakonov V. Influence of nanomorphology on the photovoltaic action of polymer-fullerene composites. *Nanotechnology*, 2004, **15**, P. 1317.

NANOSYSTEMS: PHYSICS, CHEMISTRY, MATHEMATICS, 2016, 7 (4), P. 695–698

Visible light degradation of textile effluent using nanostructured TiO_2/Ag/CuO photocatalysts

N. Karthikeyan[1,2], V. Narayanan[3] and A. Stephen[1]

[1]Department of Nuclear Physics, University of Madras, Guindy Campus, Chennai, India
[2]Department of Physics, The Open University of Sri Lanka, Nawala, Nugegoda, Sri Lanka
[3]Department of Inorganic Chemistry, University of Madras, Guindy Campus, Chennai, India
karthikppt@gmail.com, vnnara@yahoo.co.in, stephen_arum@hotmail.com

PACS 62.23.St, 42.70.Qs, 87.85.Rs **DOI 10.17586/2220-8054-2016-7-4-695-698**

TiO_2, Ag and CuO nanomaterials, and nanostructured TiO_2/Ag/CuO photocatalytic materials coupled in different weight percentages were synthesized. The prepared materials were characterized by XRD, SEM, EDX and UV-Vis diffuse reflectance spectroscopy. Photocatalytic degrading capabilities of the pure, as well as the nanostructured TiO_2/Ag/CuO photocatalytic materials were tested on the dye effluent collected from the textile industries. The samples collected during the photocatalytic degradation of textile dye effluent were studied with UV-Vis spectroscopy. The nanostructured TiO_2/Ag/CuO photocatalyst with the composition of 80:10:10 weight percentage exhibited remarkable performance. Coupling of Ag metal nanoparticles and narrow bandgap CuO semiconductor nanomaterial to the wide bandgap TiO_2 semiconductor nanomaterial was found to modify the operative bandgap of the system and generate electron-hole pairs under visible light irradiation. The coupled TiO_2/Ag/CuO system facilitates improved electron transfer to the adsorbed molecules, and thus the system improves the photocatalytic degradation of dyes by enhanced redox mechanism.

Keywords: Coupled TiO_2/Ag/CuO, Nanostructured photocatalysts, bandgap, degradation of textile effluents, advanced oxidation process.

Received: 5 February 2016. Revised: 18 April 2016.

1. Introduction

In 1972, Fujishima and Honda found that TiO_2 could be used as catalytic electrode in a photo-electrolysis cell to decompose water into H_2 and O_2, without applying an external voltage [1]. Further researches established the use of TiO_2 for photo-assisted degradation of organic compounds and reduction of inorganic compounds. Researches on purification of polluted water gained greater importance with ever increasing need to purify the industrial effluents as well as the contaminated water resources by the industrial waste streams which often created serious health and environmental problems. Among the many, textile effluents play significant role in polluting the water resources and the environment. Traditional effluent purification processes often produce end products with carcinogenic compounds, which require further treatment for complete purification. The photocatalytic degradation of textile effluents using nanophotocatalysts through advanced oxidation process is one of the recent scientific explorations that gain importance mainly due to its ability to produce harmless end products [2–4].

Titania is a semiconductor with bandgap energies in the range of 3.2 – 3.4 eV, and hence could produce electron–hole pairs upon UV region photon irradiation. When these photogenerated charge carriers migrate to the surface without recombining, they could interact with the adsorbed water and oxygen molecules to produce radical species. These radicals strike any adsorbed organic dyes and lead to complete or selective degradation. Repeated efforts are being made by the researchers to trigger this degradation process under visible light irradiation, to make the process very economical by using abundantly-available solar light in various photocatalytic applications. Efficient photogeneration of electron – hole pairs, prevention of their recombination and reduction of specific surface area of the particles of the photocatalysts are the key factors in increasing the efficiency of photocatalytic activity. Several researchers have proven that coupling of semiconductors with noble metals and other semiconductor materials at nanoscales plays significant role in modifying the above factors [5–9].

In this exploration, TiO_2, Ag and CuO nanomaterials, and nanostructured TiO_2/Ag/CuO photocatalysts coupled in different weight percentages were synthesized under optimized conditions [10,11] and tested for their degradation efficiency on a model dye and also on an effluent collected from textile industries in Tamil Nadu, India.

2. Experimental methods

Titania was synthesized using the sol-gel method, by dissolving the precursor titanium (IV) isopropoxide in isopropanol under continuous stirring at room temperature, and then by adding citric acid as the chelating agent mixed with deionized water. Ag and CuO were synthesized via thermal decomposition method by heat treatment of silver acetate and copper acetate, separately in alumina crucibles, by rising the temperature up to 300 °C in steps of 4 °C/min. Then, the respective polycrystalline nanoparticles were synthesized by annealing the as-prepared samples at the optimized temperature of 450 °C for 30 minutes. Details for this protocol were reported elsewhere [12]. Then, the coupled TiO_2/Ag/CuO photocatalysts were synthesized by taking the as prepared samples in three different weight percentages, viz. 80:15:05. 80:10:10 and 80:05:15, grinding them well for 2 hrs, and then annealing at 450 °C for 30 min.

X-ray diffraction studies were carried out on RICH SEIFERT, Germany (model 3000) diffractometer using Cu-$K_{\alpha 1}$ radiation (λ = 1.54056 Å), 30 kV voltage, and 10 mA current. Surface morphology and elemental composition were carried out using QUANTA 200 FEG high resolution scanning electron microscopy (HR-SEM) and energy-dispersive X-ray spectroscopy (EDX). The optical properties of the samples in UV and Visible ranges were investigated using CARY 5E UV-VIS-NIR spectrophotometer.

3. Results and discussions

3.1. Phase and structure confirmation

Figure 1 shows the powder XRD patterns of the TiO_2, Ag, and CuO, and that of coupled TiO_2/Ag/CuO samples prepared at weight percentages 80:05:15, 80:10:10 and 80:15:05, and annealed at 450 °C. The primary diffraction peaks of the TiO_2 were indexed to anatase phase Titania with tetragonal crystal structure, and the values well matched with the JCPDS card 84-1285. The calculated lattice parameter values are: $a = b = 3.784$ Å and $c = 9.561$ Å.

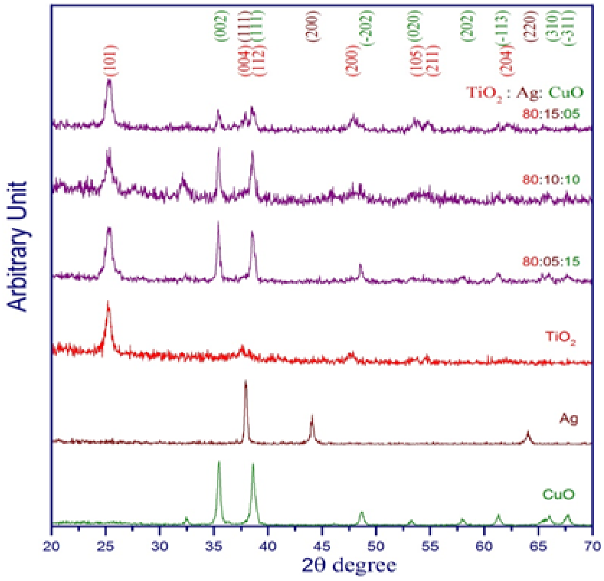

FIG. 1. XRD patterns of all the prepared samples, annealed at 450 °C for 30 min.

The characteristic peaks of the CuO were indexed to monoclinic structure and the values are in good agreement with the reported values in the JCPDS card 89-5896. The determined lattice parameters are: $a = 4.683$ Å, $b = 3.424$ Å and $c = 5.129$ Å.

The diffraction peaks of the prepared sample Ag were indexed to cubic structure and could be matched well with the JCPDS card number 03-0921. The calculated lattice parameters are: $a = b = c = 3.914$ Å.

The crystallite sizes were estimated using the Scherrer's formula, and the estimated average crystallite sizes ranged from 9 to 64 nm. No significant peak shifts were observed in the XRD patterns of the coupled systems.

The HRSEM images, as shown in Fig. 2, of the coupled photocatalysts reveal irregularly-shaped particles, which are agglomeration of the tiny spherically shaped particles. The average particle sizes of the isolated spheres were in the range from 25 to 80 nm. The EDX analysis confirmed the elemental composition in the respective coupled photocatalysts.

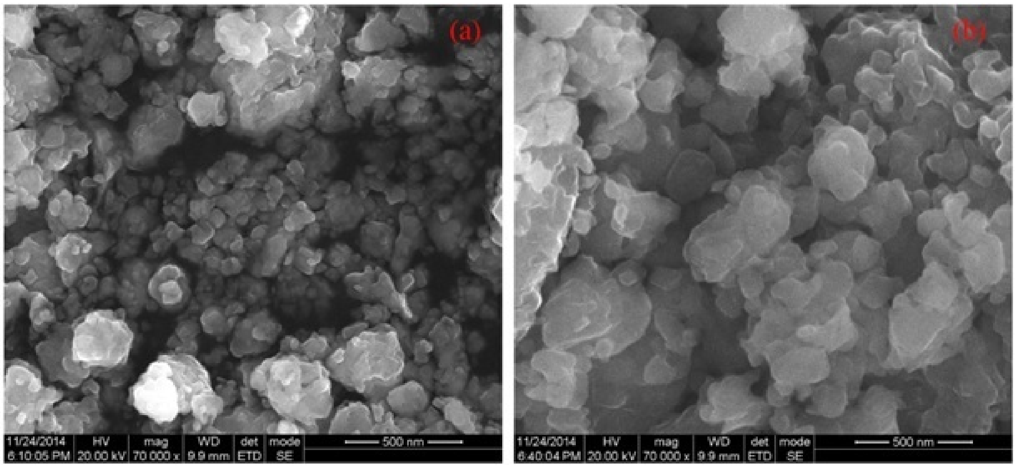

FIG. 2. HRSEM images $TiO_2/Ag/CuO$ at wt%: (a) 80:10:10; (b) 80:15:05

3.2. Optical properties and bandgap energies

UV-Vis Diffuse Reflectance spectrum of the prepared photocatalytic samples TiO_2, $TiO_2/Ag/CuO$ (80:15:05), $TiO_2/Ag/CuO$ (80:10:10) and $TiO_2/Ag/CuO$ (80:05:15) are shown in Fig. 3. The absorption edge of the pure TiO_2 was in the UV region. However, red shifts were observed for the coupled $TiO_2/Ag/CuO$ photocatalysts prepared at three different weight percentages 80:15:05, 80:10:10 and 80:05:15 and their absorption edges have fallen in the visible region.

The estimated optical band gap energies of pure TiO_2 as well as those of the coupled $TiO_2/Ag/CuO$ nanophotocatalysts prepared at three different weight percentages 80:15:05, 80:10:10 and 80:05:15 are shown in Table 1.

TABLE 1. Optical band gap energies of the prepared photocatalysts

Photocatalysts	Band gap
TiO_2	3.3 eV
$TiO_2/Ag/CuO$ (80:05:15)	3.0 eV
$TiO_2/Ag/CuO$ (80:10:10)	2.9 eV
$TiO_2/Ag/CuO$ (80:15:05)	3.0 eV

3.3. Photocatalytic degradation test results

All the photocatalysts were tested for their decoloration efficiency on the methylene blue (MB) dye under visible irradiations and the results are shown in Fig. 4. The photocatalyst $TiO_2/Ag/CuO$ synthesized at 80:10:10 wt % showed best efficiency with more than 75 % of decoloration in 120 minutes under visible light irradiation.

Then the best photocatalyst $TiO_2/Ag/CuO$ (80:10:10) was employed in the degradation of the textile effluent and the results are shown in Fig. 5. More than 80 % decoloration of the textile effluent was achieved in 240 minutes under visible light irradiation.

4. Conclusions

TiO_2, Ag and CuO, and coupled $TiO_2/Ag/CuO$ photocatalysts at three different weight percentages 80:05:15, 80:10:10 and 80:15:05 were synthesized. Their structural, morphological and optical properties were analyzed with various characterization techniques. Among the prepared photocatalysts, $TiO_2/Ag/CuO$ (80:10:10) gave the best decoloration (about 79 %) of MB in 2 hours under visible light irradiation. This is in agreement with the results obtained from the optical property studies. The best photocatalyst effectively degraded the textile effluent with an efficiency of about 82 % of decoloration in 4 hours under visible light irradiation. Inclusion of optimal amount of CuO and Ag was found to modify the band gap significantly and make the photocatalyst active under visible light. The CuO acts as sink for photogenerated electrons, prevents recombination and thus enhances the redox reaction and hence the efficiency of the degradations.

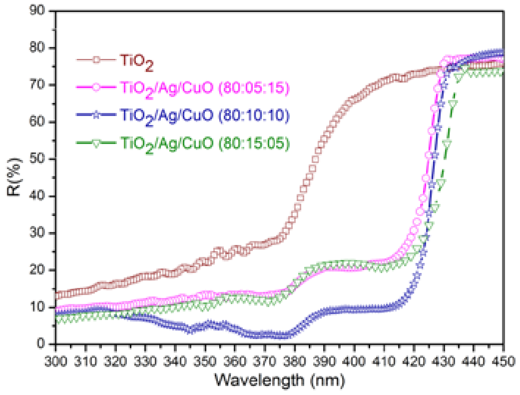

FIG. 3. Diffuse reflectance spectrum of the prepared photocatalysts

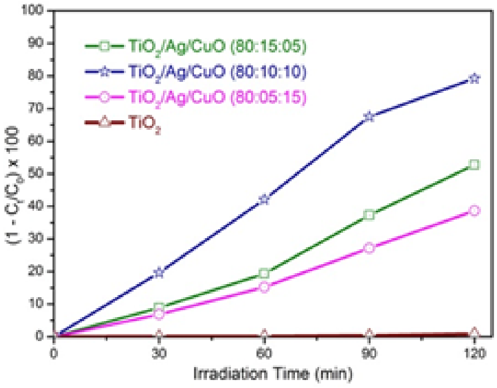

FIG. 4. Degradation profile – Methylene Blue

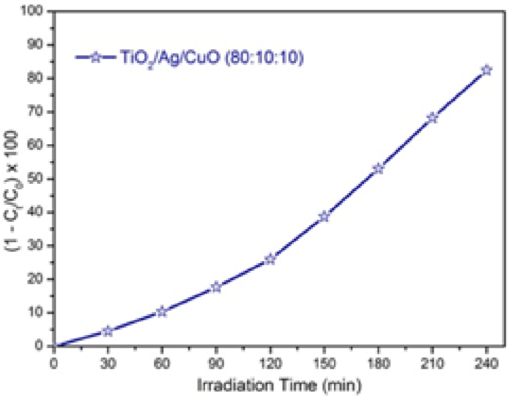

FIG. 5. Degradation profile – Textile Effluent

Acknowledgements

One of the authors, NK, thanks HETC project for the financial support. The authors are thankful to SAIF at IIT Chennai for the HR-TEM and UV-Vis DRS characterization of powder samples.

References

[1] Fujishima A., Honda K. Electrochemical Photolysis of Water at a Semiconductor Electrode. *Nature*, 1972, **238** (5358), P. 37–38.
[2] Hisaindee S., Meetani M.A., Rauf M.A. Application of LC-MS to the analysis of advanced oxidation process (AOP) degradation of dye products and reaction mechanisms. *TrAC Trends in Analytical Chemistry*, 2013, **49**, P. 31–44.
[3] Chequer F.M.D., et al. Analyses of the genotoxic and mutagenic potential of the products formed after the biotransformation of the azo dye Disperse Red 1. *Toxicology in Vitro*, 2011, **25** (8), P. 2054–2063.
[4] Parsons S.A., Williams M. *Advanced Oxidation Processes for Water and Wastewater*. London, UK: IWA Publishing, 2004, 368 p.
[5] Jakob M., Levanon H., Kamat P.V. Charge Distribution between UV-Irradiated TiO$_2$ and Gold Nanoparticles:? Determination of Shift in the Fermi Level. *Nano Letters*, 2003, **3** (3), P. 353–358.
[6] Wood A., Giersig M., Mulvaney P. Fermi Level Equilibration in Quantum Dot?Metal Nanojunctions. *The Journal of Physical Chemistry B*, 2001, **105** (37), P. 8810–8815.
[7] Anh Tuan V., et al. Synthesis and characterization of TiO$_2$ photocatalyst doped by transition metal ions (Fe^{3+}, Cr^{3+} and V^{5+}). *Advances in Natural Sciences: Nanoscience and Nanotechnology*, 2010, **1** (1), P. 015009 (4 p).
[8] Rehman S., et al. Strategies of making TiO$_2$ and ZnO visible light active. *Journal of Hazardous Materials*, 2009, **170** (2–3), P. 560–569.
[9] Qiu R., et al. Photocatalytic activity of polymer-modified ZnO under visible light irradiation. *J. Hazardous Mat.*, 2008, **156** (1–3), P. 80–85.
[10] Saravanan R., et al. Photocatalytic Degradation of Organic Dyes Using ZnO/CeO2 Nanocomposite Material Under Visible Light. *Advanced Materials Research*, 2012, **584** (1), P. 381–385.
[11] Karthikeyan N., Narayanan V., Stephen A. Effect of Annealing on Photocatalytic Degradation of Azo Dye by TiO$_2$/CuO Binary Nanostructured Materials. 4th Int. Symp. for Research Scholars on Metallurgy, Materials Science and Engineering. *ISRS*, 2012.
[12] Karthikeyan N., Narayanan V., Stephen A. Synthesis and Characterization of Coupled ZnO/Ag/CuO Nanomaterials for Photocatalytic Degradation of Organic Dye under UV irradiation. *Int. J. Inn. Res. Sci. & Eng.*, 2014, **2** (spl), P. 74–79.

NANOSYSTEMS: PHYSICS, CHEMISTRY, MATHEMATICS, 2016, 7 (4), P. 699–702

Temperature influence study on copper selenide films

V. Rajendran[1], S. Arulmozhi Packiaseeli[2], S. Muthumari[3] and R. Vijayalakshmi[3]

[1]Department of Physics, Vivekananda College, Madurai 625234, India
[2]P. G. & Research Department of Physics, Fatima College, Madurai 625018, India
[3]P. G. & Research Department of Physics, Thiagarajar. College, Madurai 625009, India

rajendran.vvc@gmail.com, ramyarv@rediffmail.com

PACS 74.25 Gz, 64.70 ph, 61.05 Cp **DOI 10.17586/2220-8054-2016-7-4-699-702**

Copper selenide was prepared by film is successfully deposited on a Fluorine-doped Tin Oxide (FTO) substrate by a brush plating technique. The film was uniform, had good adherence to the substrate and was annealed at 300 °C and 500 °C. As the annealing temperature increased, the orientation of the crystallites is more randomized than in the as-prepared film. The structural and optical properties of the film were investigated by XRD, SEM, EDAX, UV-Visible and PL. The XRD pattern indicated that this film was crystalline in the structure.

Keywords: Brush plating, copper selenide, optical properties.

Received: 5 February 2016

Revised: 3 May 2016

1. Introduction

Copper selenide (Cu_2Se) thin films have attracted considerable interest over the last year owing their wide range of applications in optoelectronic devices and solar cells. Copper selenide is an interesting metal chalcogenide semiconductor material. A copper selenide thin film has a direct band gap and is transparent over a wide range of the visible spectrum. It is seen that the photoelectronic and other properties of II–VI class of compound thin films are highly optically-sensitive, which in turn, can severely influence device performance [1]. More progress has been achieved in the fabrication of light emitting diodes, dielectric mirrors and other optically sensitive devices.

Selenium-based alloys are not stable under standard operational conditions because their glass transitions are typically close to room temperature. In order to stabilize these glasses it is common to use an additive which acts as a cross-linking agent and increase the dimensionality of structure and stability of the material [2]. The purpose of present study is to explore and report in detail the structural properties and optical properties of copper selenide thin film prepared by brush plating technique.

2. Experimental procedure

The precursor solution was prepared by stirring 1 g of copper(II) sulfate ($CuSO_4$) and 0.05 gm of selenium dioxide (SeO_2) in 5 ml of distilled water until the powder is totally mixed to provide a saturated solution. The Copper Selenide thin films were prepared by Brush Plating technique. The films were grown on Fluorine doped Tin Oxide (FTO) substrate under optimized conditions. These grown films were uniform, blue in color and showed good adherence to the substrate surface. All chemicals were of AR grade.

The as-deposited films were annealed at 300 °C and 500 °C for about 1 hr. The annealed film was utilized for optical- and structural properties studies.

3. Results and discussion

3.1. XRD Analysis

Figures 1(a) and (b) show the X-ray diffraction pattern of the brush plated copper selenide thin film. The XRD pattern obtained correlated well with the standard JCPDS (06-680) data.

Crystallite size (D) was calculated using Debye-Scherrer's formula [3]:

$$D = 0.94\lambda/\beta\cos\theta,$$

where D is the crystallite size, λ is the wavelength of the k_α line, β is the full width at half maxima (FWHM) in radians and θ is the Bragg's angle. The crystallite grain size increased from 2 – 53 nm as the annealing temperature increased [4]. The observed 'd' values 4.5, 2.2, 2.0, 1.5 Å are in good agreement with the standard 'd' values. Peaks corresponding to (1 1 0), (2 2 0), (3 1 0), (4 0 1) were observed [5].

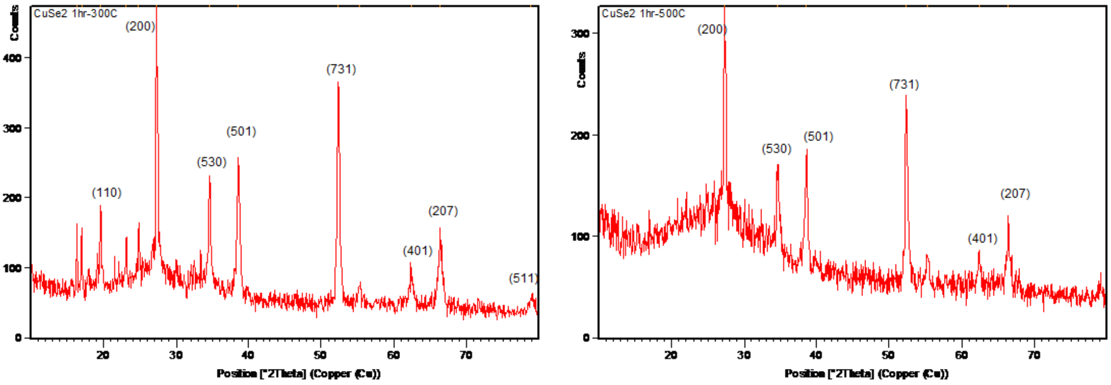

(a) (b)

FIG. 1. XRD pattern of Cu_2Se thin film annealed at 300 °C (a) and 500 °C (b)

3.2. Morphological studies and compositional analysis

Scanning electron microscopy is a convenient tool to study the surface morphology of micro- and nanoscale materials as well as thin films. Fig. 2(a,b) shows the SEM images of CuSe thin films annealed at 300 °C and 500 °C recorded at 20 kV with the magnification 10000 using the instrument JSM-6390. The particle size increased as the annealing temperature increased [6].

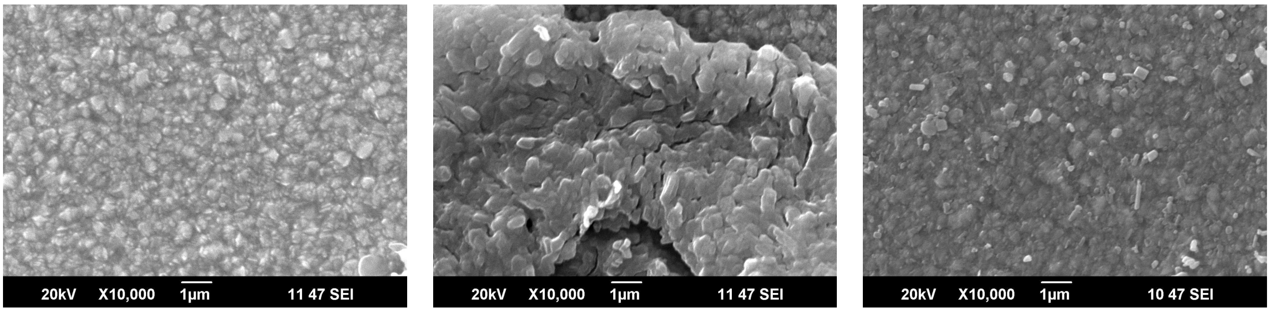

(a) (b) (c)

FIG. 2. SEM image of Cu_2Se as deposited (a); annealed at 300 °C (b) and 500 °C (c)

The EDAX analysis from Fig. 3(a–c) revealed that the presence of copper, selenium, oxygen and other elements like silicon, tin on the FTO substrate. The EDAX spectrum recorded in the binding energy region of 0 – 10 keV showed the presence of copper and selenium in thin films. EDAX analysis of the mass % and atom % of copper selenide films are tabulated in Table 1. EDAX spectrum confirms the presence of copper and selenium in the thin films [7].

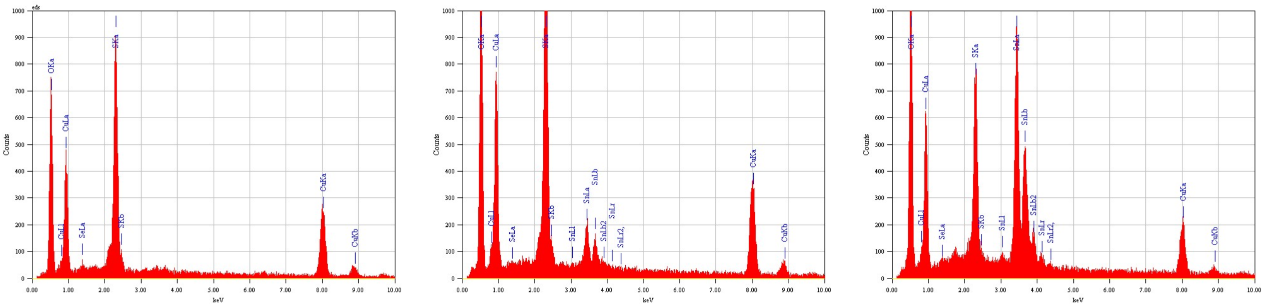

(a) (b) (c)

FIG. 3. EDAX analysis of Cu_2Se as deposited (a); annealed at 300 °C (b) and 500 °C (c)

TABLE 1. Mass and Atom percentage of Cu_2Se annealed at 300 °C and 500 °C

Sample	Mass %		Atom %	
	Copper	Selenium	Copper	Selenium
As-deposited	49.35	1.19	26.23	0.51
Annealed at 300 °C	38.73	0.42	21.78	0.19
Annealed at 500 °C	16.37	0.41	12.89	0.26

3.3. Optical absorption, transmittance and reflectance measurement

The typical optical absorbance, transmittance $T(\%)$ spectra and reflectance spectra of the films prepared using brush plating method are presented in Fig. 4(a–c) respectively for the as-deposited and annealed samples (at 300 °C and 500 °C). Annealing the film at 300 °C and 500 °C resulted in some changes in the optical transmittance and absorbance spectra of the films.

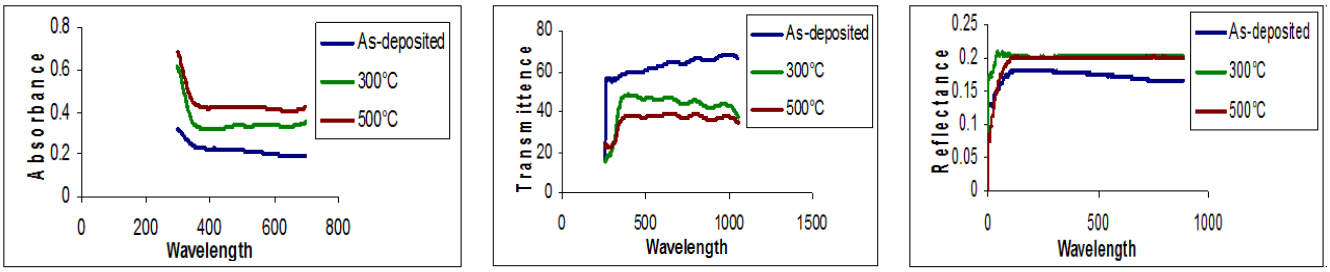

(a) (b) (c)

FIG. 4. Absorption (a), transmittance (b) and reflectance (c) spectra for Cu_2Se

The Egdir values for the samples were as follows: as-deposited – 2.95 eV; 300 °C annealing – 2.86 eV and 500 °C annealing – 2.75 eV. The Egind values were as follows: as-deposited – 2.16 eV; 300 °C annealing – 2.54 eV and 500 °C annealing – 2.38 eV. The indirect band gap values were as follows: re as-deposited – 2.16 eV; 300 °C annealing – 2.54 eV and 500 °C annealing – 2.38 eV. All these optical band gap values are close to those previously obtained for the material used for solar cells, which means that these materials have good utility for this purpose [8].

3.4. Photoluminescence spectrum

The photoluminescence spectra of Cu_2Se thin films are shown in Fig. 5. From the spectra, the photons are excited at a wavelength of 280 nm. As the annealing temperature increases, the intensity of the peak increases. From the spectra, the peaks observed in emission of Cu_2Se thin films are at a wavelength 561 nm [9]. The spectra of the as-deposited Cu_2Se films and the annealed films showed increasing intensity as the annealing temperature increased.

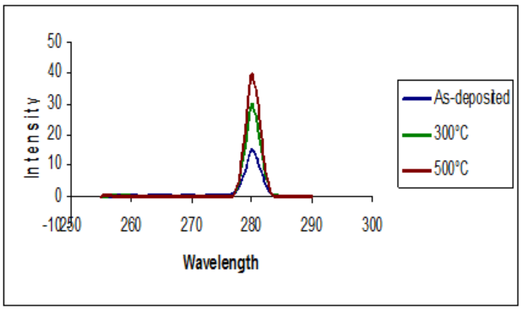

FIG. 5. Excitation Spectra of Cu_2Se

4. Conclusion

Copper Selenide thin films were successfully deposited on FTO substrates by a brush plating technique. The films were uniform and had good aherence to the substrate. The XRD of Copper Selenide films formed a cubic structure. The crystalline size of the films were determined by Scherrer's formula and it increased from 2 – 53 nm as the annealing temperature increased [10]. The energy gap values of the films were determined and compared with the reported one. The emitted and excited wavelength were determined from the photoluminescence spectra. The structural properties, surface morphological studies and chemical composition analysis were investigated and reported.

References

[1] Vipin kumar, Vinod Kumar, Dwivedi D.K. Growth and characterization of zinc telluride thin films for photovoltaic applications. *Physica Scripta*, 2012, **86**, 015604 (4 p.)

[2] Vijayalaksmi R., Chandrasekar L. Bruno, Chandramohan R. Preparation and Characterization of Se-Te-Ag Chalcogenide Thin Film. *Journal of Nanoengineering and Nanomanufacturing*, 2013, **3**, P. 70–72.

[3] Hammad Jamil T.M., Salem K., Harrison R.G. Binding agent affect on the structural and optical properties of ZnO nanoparticles. *Rev. Advanced Material Science*, 2009, **22**, P. 74–80.

[4] Ramesh K., Thanikaikarasan S., Bharathi B. Structural, morphological and optical properties of copper selenide thin films. *International Journal of Chem. Tech. Research*, 2014, **6** (13), P. 5408–5411.

[5] Garcia V.M., Nair P.K., Nair M.T.S. Binding Agent affect on the Structural and Optical Properties of ZnO nanoparticles. *Journal Of Crystal Growth*, 1999, **203**, P. 113–124.

[6] Thi Die Thuy Ung, Quang Liem Nguyen. Structural, Morphological and Optical Properties of Copper Selenide Thin Films. *Adv. Nat. Sci: Nanosci. Nanotechnol.*, 2011, **2**, 045003.

[7] Mehta N., Zulfequar M., Kumar A., Crystallization kinetics of some Se-Te-Ag chalcogenide glasses. *Journal of Optoelectronics and Advanced Materials*, 2004, **6**, P. 441.

[8] Arokiya Mary T., et al. A simple hydrothermal route for synthesizing copper Selenide Nano-Flakes. *Elixir Nanocomposite Materials*, 2012, **50**, P. 10499–10500.

[9] Garcia V.M., Guerrero L., Nair M.T.S., Nair P.K. Effect of thermal processing on optical and electrical properties of copper selenide thin films. *Superficies y Vacio*, 1999, **9**, P. 213–218.

[10] Arulmozhi Packiaseeli S., Rajendran V., Vijayalakshmi R. Structural, optical and morphological study of tungsten selenide thin films. *Nanosystems: Physics, Chemistry, Mathematics*, 2016, **7** (4), P. 703–706.

NANOSYSTEMS: PHYSICS, CHEMISTRY, MATHEMATICS, 2016, 7 (4), P. 703–706

Structural, optical and morphological study of tungsten selenide thin films

S. Arulmozhi Packiaseeli[1], V. Rajendran[2] and R. Vijayalakshmi[3]

[1]P.G. & Research Department of Physics, Fatima College, Madurai, India
[2]Department of Physics, Vivekananda College, Madurai, India
[3]P.G. & Research Department of Physics, Thiagarajar. College, Madurai, India

arulmozhipackiaseeli@gmail.com, ramyarv@rediffmail.com

PACS 68.55-a, 74.25 Gz, 64.70ph, 61.05Cp **DOI 10.17586/2220-8054-2016-7-4-703-706**

Tungsten selenide (WSe_2) film was successfully deposited on FTO substrate by brush plating technique. The film was uniform and well adherent to the substrate and annealed to 300 °C and 500 °C. As the annealing temperature was increased the orientation of the crystallites was more randomized than in the as-prepared film. The structural and optical properties of the film were investigated by XRD, SEM, EDAX, UV-Visible and PL. The XRD pattern indicates that this film was crystallized in the hexagonal structure.

Keywords: WSe thin film, morphology.

Received: 5 February 2016

Revised: 3 May 2016

1. Introduction

Metal Chalcogenide thin films such as tungsten selenide films are promising semiconducting materials suitable for solar cells. Tungsten selenide thin films have band gaps of 2.16 eV $\leq E_g \leq$ 2.65 eV and reasonable overlap with the solar spectrum [1]. Tungsten selenide thin film has direct band gap and is transparent over a wide range of the visible spectrum. It can be seen that the photoelectronic and other properties of class II–VI compound thin films are highly optically sensitive, which in turn can severely influence device performance. More progress has been achieved in the fabrication of light emitting diodes, dielectric mirrors and other optically sensitive devices [2].

2. Experimental procedure

Precursor solution was prepared by magnetically stirring 1 g of tungsten trioxide (WO_3) and 0.05 g of selenium dioxide (SeO_2) with 5 ml of distilled water until the powder was thoroughly mixed to form a homogenous solution. The tungsten selenide thin films were prepared by Brush Plating technique on the FTO (Fluorine doped Tin Oxide) substrate. The as-deposited films were annealed at 300 °C and 500 °C for about 1 hour. The structural optical and morphological properties of the as-deposited and annealed tungsten selenide thin films were studied.

3. Results and discussion

3.1. XRD Analysis

Figure 1(a) shows the XRD pattern of the as-deposited tungsten selenide film on the FTO (Fluorine doped Tin Oxide) substrate. The as-deposited WSe_2 films are amorphous in nature. Fig. 1(b) and 1(c) show the XRD pattern of tungsten selenide films which were annealed at 300 °C and 500 °C respectively. The pattern shows well-defined peaks, suggesting that the films are polycrystalline. Tungsten selenide possesses a hexagonal structure with $a = 3.29$ Å and $b = 12.97$ Å. The XRD pattern obtained correlated well with the standard JCPDS (06-0080) data. Peaks corresponding to (0 0 4), (1 0 2), (1 0 3), (1 0 6), (1 1 0), (1 0 8) were observed. The observed peaks were identified and matched with the reported values [3]. The crystallite grain size in the film was calculated using the Scherer's formula [4]:

$$D = 0.94\lambda/\beta\cos\theta \ \text{(nm)},$$

where D is the crystallite size, λ is the wavelength of the k_α line, β is the full width at half maxima (FWHM) in radians and θ is the Bragg's angle. The crystallite grain size increased from 9 – 11 nm as the annealing temperature was increased [5].

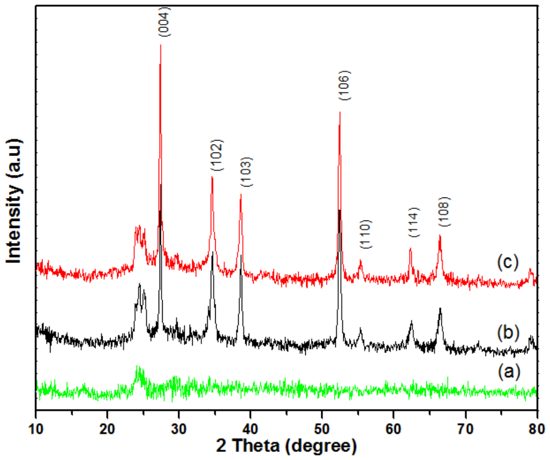

FIG. 1. WSe_2 film as deposited (a); annealed at 300 °C (b) and 500 °C (c)

3.2. Morphological study of tungsten selenide thin films

Figure 2(a-b) shows SEM images of tungsten selenide films. Detailed morphological study of the films was carried out using the JSM-6390 instrument. At 1.500× magnification the film shows a clear picture. When the magnification is increased from 1.500 to 10.000 the flakes type crystals are found. Smooth surface is obtained in the as-deposited film. The particle size was found to increase as the annealing temperature was increased [6].

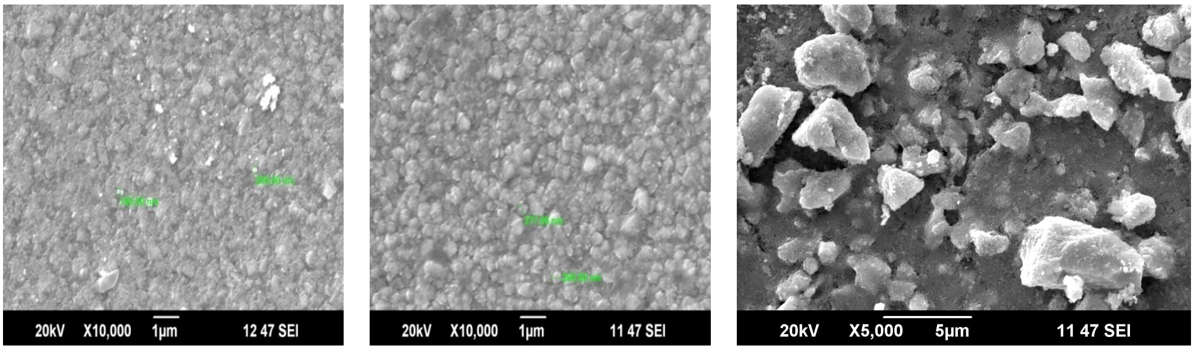

(a) (b) (c)

FIG. 2. As-deposited tungsten Selenide (a); film annealed at 300 °C (b) and 500 °C (c)

3.3. EDAX analysis of tungsten selenide films

The EDAX spectrum was recorded in the binding energy region of 0 – 10 keV Fig. 3(a,b) reveal the presence of tungsten, selenium, oxygen and other elements like silicon, tin on the FTO substrate. EDAX analysis of the elements present, mass % and atom % of tungsten selenide films are also tabulated [7] (Table 1).

TABLE 1. Mass and Atom percentage of WSe_2 annealed at 500 °C and 500 °C

Sample	**Mass %**		**Atom %**	
	Tungsten	**Selenium**	**Tungsten**	**Selenium**
As-deposited	2.16	0.47	1.18	0.6
Annealed at 500 °C	42.37	3.82	23.8	4.99

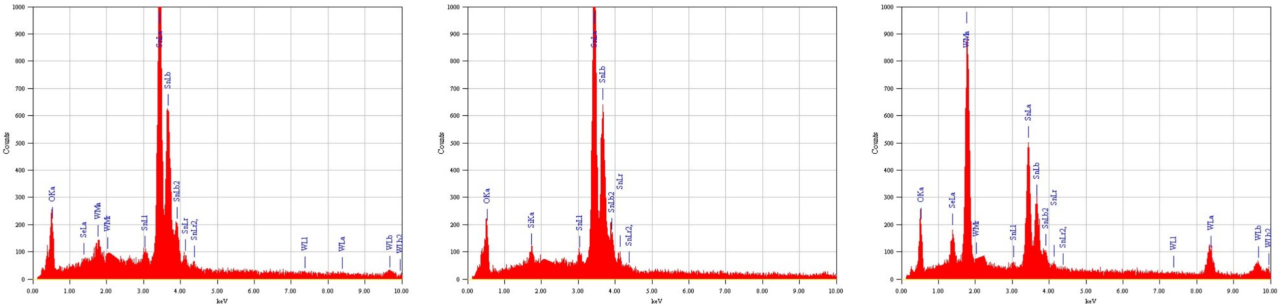

(a) (b) (c)

FIG. 3. WSe_2 as deposited (a); annealed at 300 °C (b) and 500 °C (c)

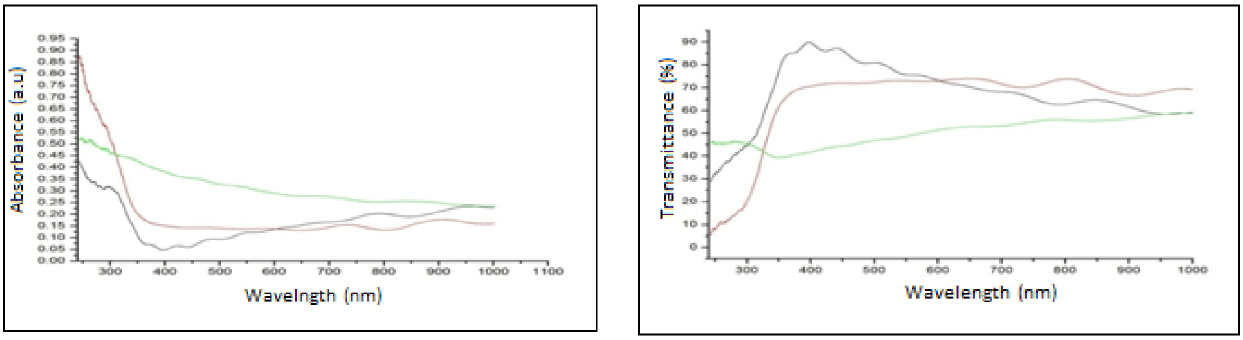

(a) (b)

FIG. 4. Absorption (a) and transmittance (b) spectra for Tungsten Selenide films

3.4. Optical absorption and transmittance measurement

Typical optical absorbance and transmittance T (%) spectra of the films prepared using brush plating method are presented in Fig. 4(a,b) respectively for the as-deposited and annealed samples (at 300 °C and 500 °C). Annealing the film at 300 °C and 500 °C did cause some changes in the optical transmittance and absorbance spectra of the films.

The typical optical absorbance and transmittance spectra of as-deposited and annealed films of tungsten selenide have been recorded and the band gap values for the films were estimated. For this, the transmittance spectra were corrected for the loss due to reflectance. The direct and indirect band gap values were obtained from plots of α_g^2, $\alpha_g^{1/2}$ respectively, against the corresponding photon energy ($h\nu$) values. Table 2 shows band gap energy of Tungsten selenide thin films for as-deposited as well as for the annealed at 300 °C and 500 °C. These optical band gap values are close to that of the already reported materials used in solar cells, which means that these films reveals good optical property necessary for this purpose [8].

TABLE 2. Direct and Indirect band gap of WSe_2

Tungsten Selenide	Direct band gap (eV)	Indirect band gap (eV)
As-deposited film	2.75	2.375
Annealed at 300 °C	2.65	2.20
Annealed at 500 °C	2.48	2.16

3.5. Photoluminescence spectrum

The photoluminescence spectra of the WSe_2 thin films are shown in Fig. 5. From the spectra, the photons are excited at a wavelength of 280 nm. As the annealing temperature increased, the intensity of the peak increased. From the spectra, the peaks observed in the emission spectrum of WSe thin films are at a wavelength of 560 nm.

The spectra of the as-deposited WSe films and the annealed films show an increase in the intensity as the annealing temperature is increased.

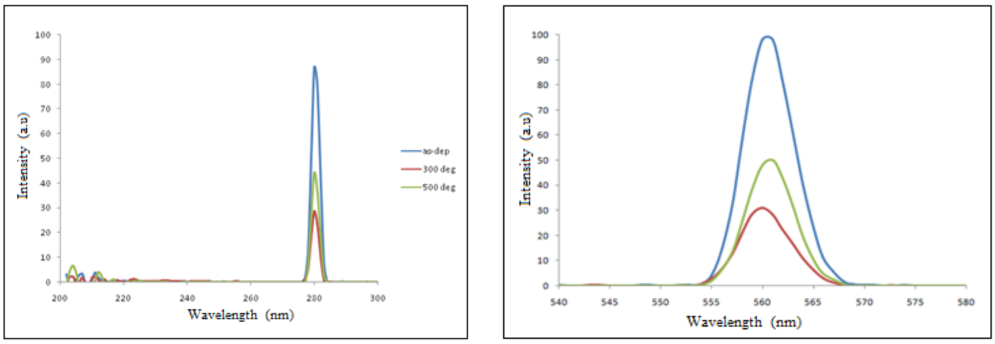

(a) (b)

FIG. 5. Excitation (a) and emission (b) spectra of Tungsten Selenide films

4. Conclusion

Structural and surface morphological studies of tungsten selenide thin films deposited by a brush plating method were carried out with (i) as deposited film, (ii) film annealed at 300 °C and (iii) film annealed at 500 °C. The SEM micrographs reveal changes in the surface morphology from amorphous to polycrystalline at 300 °C and an increase in the size of crystallites when annealed at 500 °C. Also, the EDAX analysis confirmed the presence of tungsten and selenium in the films. Optical characterization has been performed and band gap values were obtained for the films which revealed that the films possessed very good optical properties necessary for the materials used in solar cells [9].

References

[1] Vipin kumar, Vinod Kumar, Dwivedi D.K. Growth and characterization of zinc telluride thin films for photovoltaic applications. *Physica Scripta*, 2012, **86**, P. 015604.

[2] Liu X., Khan B.B., Tikhomirov V.K., Jha A. Semiconducting Chalcogenide Glass III: Applications of Chalcogenide Glasses. *J. Non-Cryst. Solids*, 1999, **294**, P. 256–257.

[3] Salitra G., Hodes G., Klein E., Tenne R. Highly oriented WSe_2 thin films prepared by selenization of evaporated WO_3. *Thin solid films*, 1994, **245**, P. 180–185.

[4] Bari R.H., Ganesan V., Potadar S., Patil L.A. Structural, optical and electrical properties of chemically deposited copper selenide films. *Bull. Mater. Sci.*, 2009, **32**, P. 37–42.

[5] Ramesh K., Thanikaikarasan S., Bharathi B. Structural, Morphological and Optical Properties of Copper Selenide Thin Films. *International Journal of ChemTech Research*, 2014, **6** (13), P. 5408–5411.

[6] Thi Die Thuy Ung, Quang Liem Nguyen. Synthesis and characterization of Fe doped Ti O_2 photocatalyst by the Sol Gel method. *Adv. Nat. Sci: Nanosci. Nanotechnol.*, 2011, **2**, 045003.

[7] Patel P.R., Patel H.S.,et al. Growth, Structural and Electrical Characterization of Tungsten Diselenide crystal. *American Journal of Condensed Matter Physics*, 2013, **3** (1), P. 13–20.

[8] Arokiya Mary T. et al. A simple hydrothermal route for synthesizing copper. *Selenide Nano-Flakes Elixir Nanocomposite Materials*, 2012, **50**, P. 10499–10500.

[9] Rajendran V., Arulmozhi Packiaseeli S., Muthumari S., Vijayalakshmi R. Temperature influence study on the copper selenide films. *Nanosystems: Physics, Chemistry, Mathematics*, 2016, **7** (4), P. 699–702.

NANOSYSTEMS: PHYSICS, CHEMISTRY, MATHEMATICS, 2016, 7 (4), P. 707–710

$ZnO/SnO_2/Zn_2SnO_4$ nanocomposite: preparation and characterization for gas sensing applications

M. Chitra[1], K. Uthayarani[1,*], N. Rajasekaran[2], N. Neelakandeswari[2], E. K. Girija[3], D. Pathinettam Padiyan[4]

[1]Department of Physics, Sri Ramakrishna Engineering College, Coimbatore–641022,
Tamilnadu, India

[2]Department of Chemistry, Sri Ramakrishna Engineering College, Coimbatore–641022,
Tamilnadu, India

[3]Department of Physics, Periyar University, Salem–636011, Tamilnadu, India

[4]Department of Physics, Manonmaniam Sundaranar University, Abhishekapatti,
Tirunelveli–627012, Tamilnadu, India

*uthayaranik@gmail.com

PACS 81.07.-b **DOI 10.17586/2220-8054-2016-7-4-707-710**

Zinc oxide (ZnO) / Tin oxide (SnO_2) / Zinc stannate (Zn_2SnO_4) nanocomposite is prepared via hydrothermal route followed by calcination. The nanocomposite is characterized by X–ray powder diffraction, Fourier Transform Infrared spectroscopy and UV spectroscopy techniques. The nanocomposite's morphology and the elemental composition is recorded using field emission scanning electron microscopy and energy dispersive X–ray spectroscopy analysis. The nanorods dispersed in the matrix of nanoparticles increases the surface active sites for gas adsorption and this material would be explored as a potential candidate for gas sensing applications at room temperature with quick response and recovery in the near future.

Keywords: zinc oxide, tin oxide, zinc stannate, hydrothermal.

Received: 5 February 2016

Revised: 26 April 2016

1. Introduction

A hybrid nanomaterial comprised of zinc oxide (ZnO) and tin oxide (SnO_2) act as multi-component system in which two or more of its combinations result in the enhancement of functional properties. Both ZnO and SnO_2 are well-known wide direct band gap ($E_g = 3.37$ eV and 3.6 eV at 300 K respectively) semiconductors and both serve as potential candidates in the field of gas sensors, solar cells, optoelectronic devices, LED, lithium ion batteries and so on. Recent investigations also state that the addition of a secondary component oxide in the form of the composite inhibits the grain growth of the host material [1] and these coupled oxides with different band gap widths are the effective approaches to enhance the storage capacity, photocatalytic activity, sensing of gases etc., [2] Voluminous reports are available for synthesizing such composites with unique hierarchical morphologies [3]. In this present work, $ZnO/SnO_2/Zn_2SnO_4$ composite is prepared via a hydrothermal route and it is characterized with various state-of-the art techniques and is reported herein.

2. Experimental details

0.1 M aqueous zinc chloride and stannous chloride solution together with glyoxylic acid monohydrate ($C_2H_2O_3{\cdot}H_2O$) was prepared. Ammonium hydroxide was added dropwise under constant stirring at room temperature to adjust the pH to 9. The gel was then transferred into a Teflon – lined stainless – steel autoclave and maintained at 160 °C for 3 h. Aerogel was collected, washed with absolute ethanol and deionized water several times and dried in air. The product obtained was calcined at 600 °C for 3 h.

The X-ray powder diffraction (XRD) pattern of the sample was carried out using PANalyticalX'Pert PRO diffractometer with Cu-Kα radiation (λ= 1.54 Å) in 2θ ranging from 20 °–80 °. The crystalline nature of the samples and the identification of different phases were accomplished by comparing the XRD pattern with standard data provided by the International Center for Diffraction data (ICDD). The lattice parameters were calculated by least squares method and the average crystallite size (D) was calculated using the Scherrer formula:

$$D(nm) = \frac{K\lambda}{\beta\cos\theta}, \tag{1}$$

where K is a constant (app 0.9 assuming the particles are spherical), λ is the wavelength of CuKα radiation (1.54056×10^{-10} m), β is full width at half maximum (FWHM) (in radian) and θ is the angle of diffraction (in °). The surface morphology of the sample was examined using ZEISS ultrafield emission scanning electron microscope (FE-SEM). The elemental composition analysis was carried out using an energy dispersive X-ray (EDAX) spectrometer (Oxford EDS INCA PENTA FETX3) attached with FE-SEM. Fourier Transform Infrared (FT-IR) spectra of the samples were recorded in the 4000 – 400 cm^{-1} region using a Perkin Elmer RX1 FT-IR spectrometer by KBr pellet technique. UV-visible spectrum was obtained using JASCO – UV VIS spectrophotometer.

3. Results and discussion

Figure 1 shows the XRD pattern of the as prepared sample. The peaks obtained in the XRD pattern matches both the hexagonal wurtzite structured ZnO(ICDD No:36-1451) and tetragonal structured SnO_2 (ICDD No: 41-1445).

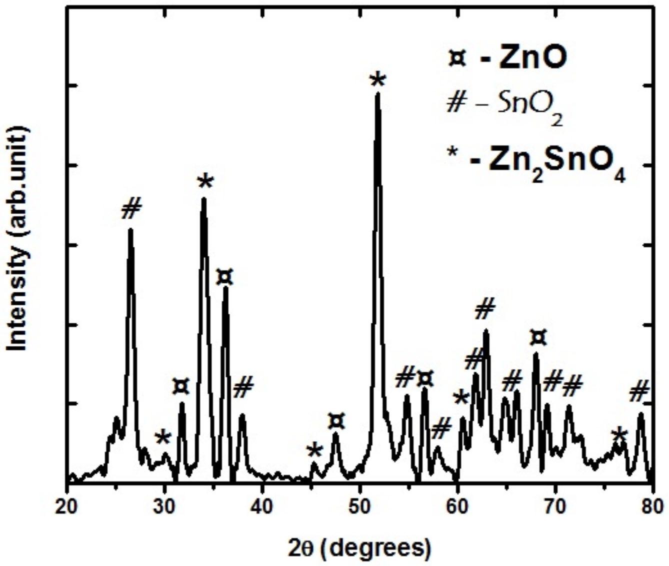

FIG. 1. XRD pattern of $ZnO/SnO_2/Zn_2SnO_4$ nanocomposite material

In this context, only negligible variation in the lattice parameters occurs for both the phases, which suggests that Zn^{2+} ions might not have been substituted into the SnO_2 lattice due to its larger ionic radius ($Zn^{2+} = 0.79$ Å and $Sn^{4+} = 0.68$ Å). In addition to these two individual oxides, two sharp peaks at (311) and (422) of the secondary phase corresponding to the spinel Zn_2SnO_4 (ICDD No: 24-1470) were observed. This reveals the polycrystalline nature of the composite material and is also supported by the formation of SnO_2 nanoparticles amidst the ZnO nanorods in the FeSEM image. The diffractogram displays a preferential orientation to the ZnO reflection at $2\theta \sim 36.195°$, SnO_2 reflection at $2\theta \sim 26.476°$ and Zn_2SnO_4 reflections at $2\theta \sim 34.290°$ and 51.796°. The existence of these three phases for an equimolar (1:1) mixture of Zn/Sn nanocomposite at a higher calcination temperature is supported by the reports of Wang et al [1], Ruvini Dharmadasa et. al. [2]. The crystallite size of the composite material comprising the peaks of ZnO, SnO_2 and Zn_2SnO_4 were calculated using the Scherrer formula is around 30 nm, 29 nm and 21 nm respectively. The observed smaller crystallite size of 27 nm would enhance the sensitivity of the composite material towards gases.

Fe–SEM image of the composite material in Fig. 2(a) depicts both the smaller spherical and larger hexagonal structured nanoparticles clouded amidst the nanorods. The hexagonally-faceted nanorods of length 105 nm and diameter 30 nm correspond to ZnO. The spherical-shaped nanoparticles of grain size around 25 nm correspond to the SnO_2 nanoparticles. The formation of hexagonal shaped nanoparticles of about 20 nm is due to the existence of the secondary phase Zn_2SnO_4 which inhibits the growth of ZnO nanorods. The presence of Zn (26.79%), Sn (28.81%) and O (44.40%) observed from the EDAX analysis (Fig. 2(b)) also supports the equimolar mixture of the precursors. The nanorods in the matrix of the nanoparticles would increase the surface area of the composite material which might provide more surface active sites for the adsorption of gas molecules.

The FT-IR spectrum of the composite material is shown in Fig. 3. The strong absorbance band around 3524 cm^{-1} corresponds to the stretching vibration (H-O-H) and a peak around 1515 cm^{-1} corresponds to the

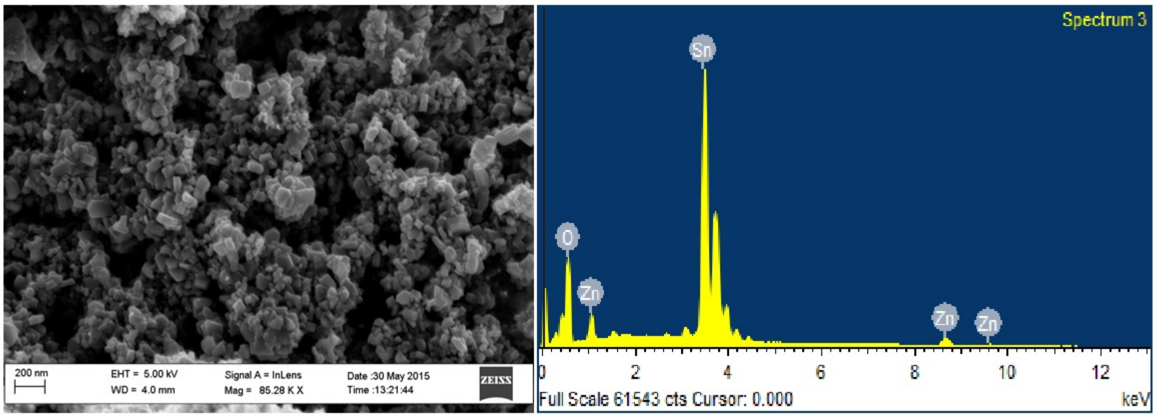

FIG. 2. (a) Fe–SEM image of $ZnO/SnO_2/Zn_2SnO_4$ nanocomposite material; (b) EDAX spectrum of $ZnO/SnO_2/Zn_2SnO_4$ nanocomposite material

bending vibrations (O-H) between oxygen and hydrogen atoms of the bound water. The absorption bands at 664.89, 866.81 and 1696.90 cm^{-1} are due to the vibration of M–O or M–O–M groups in ZnO, SnO_2 and Zn_2SnO_4 [4]. The results obtained by FT-IR analysis further confirm the formation of the composite and thus agree with the results obtained in XRD analysis.

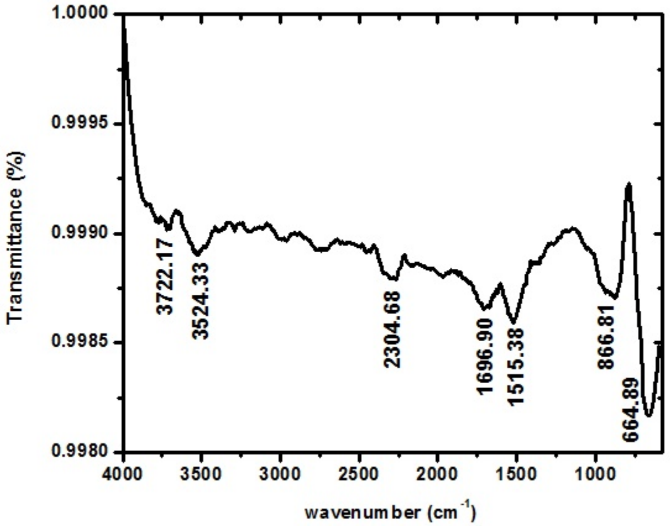

FIG. 3. FT–IR spectrum of $ZnO/SnO_2/Zn_2SnO_4$ nanocomposite material

Figure 4 shows the UV–Vis absorption spectrum of the composite material measured in the wavelength range of 200–800 nm. The absorption band edges were observed around 223 nm, 226 nm and 376 nm which correspond to the characteristic bands of SnO_2, Zn_2SnO_4 and ZnO respectively. Investigations done on such equimolar mixture of Zn/Sn composites obtain similar kind of absorption edge for the nanoparticles ranging from 40–70 nm. The reported band gap values of ZnO, SnO_2 and Zn_2SnO_4 are 3.37 eV, 3.65 eV and 3.6 eV respectively. The band gap value of the composite material calculated using the Tauc plot (shown in Fig. 5) is 3.7 eV. The smaller band gap value obtained by the composite material is attributed to the synergistic effect of the material.

4. Conclusion

$ZnO/SnO_2/Zn_2SnO_4$ nanocomposite has been successfully synthesized via a hydrothermal route followed by calcination. The formation of the composite was confirmed by XRD and FT–IR. Fe–SEM image revealed the presence of SnO_2 nanoparticles among the ZnO nanorods. The secondary phase Zn_2SnO_4 in the material inhibited the growth of nanorods, resulting in a larger surface area.

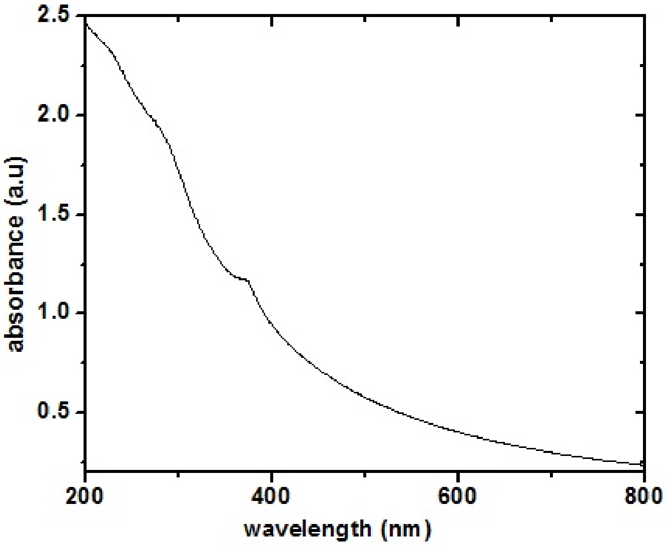

FIG. 4. UV–Vis spectrum of $ZnO/SnO_2/Zn_2SnO_4$ nanocomposite material

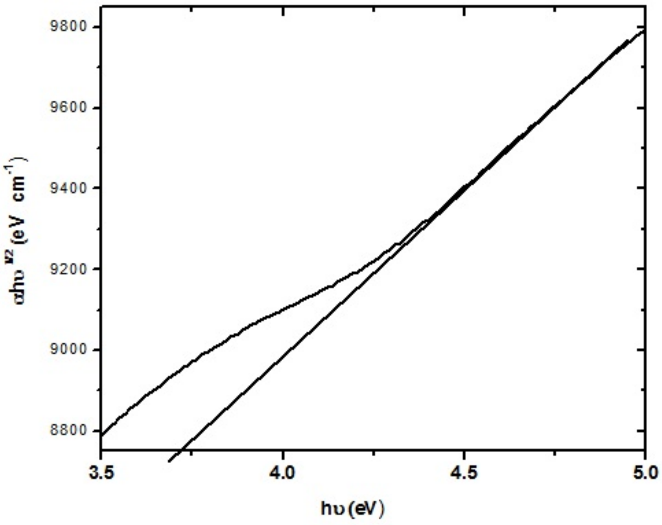

FIG. 5. Tauc plot of $ZnO/SnO_2/Zn_2SnO_4$ nanocomposite material

References

[1] Chen L., Bai S., Zhou G., Li D., Chen A., Chung C.L. Synthesis of $ZnO–SnO_2$ nanocomposites by microemulsion and sensing properties of NO_2. *Sensors and Actuators B*, 2008, **134**, P. 360–366.

[2] Tiekun J., Junwei Z., Fang F., Zhao D., Weimin W. Zhengyi Fu., Fancheng M. Synthesis, characterization, and photocatalytic activity of Zn-Doped SnO_2/Zn_2SnO_4 coupled nanocomposites. *International Journal of Photoenergy*, 2014, 197824.

[3] Ruvini D., Asif A., Tahir, K.G., Upul W. Single step growth and characterization of zinc Oxide, tin Oxide and composite ($Zn_xSn_{1\text{-}x}O_y$) nanoplate and nanocolumn Electrodes. *J. Am. Ceram. Soc.*, 2011, **94**(10), P. 3540–3546.

[4] Guang S., Saisai Z., Yanwei L. Solvothermal synthesis of Zn_2SnO_4 nanocrystals and their photocatalytic properties. *International Journal of Photoenergy*, 2014, 580615.

NANOSYSTEMS: PHYSICS, CHEMISTRY, MATHEMATICS, 2016, 7 (4), P. 711–723

Inhibition of corrosion of mild steel in well water by TiO_2 nanoparticles and an aqueous extract of May flower

P. Nithyadevi[1], R. Joseph Rathish[2], J. Sathiya Bama[1], S. Rajendran[3,*], R. Maria Joany[4], M. Pandiarajan[1],
A. Anandan[5]

[1]PG and Research Department of Chemistry, GTN arts College, Dindigul–624005, India

[2]PSNA College of Engineering and Technology, Dinidgul, India

[3]Corrosion Research Centre, Department of Chemistry, RVS Educational Trust's Group of Institutions, Dindigul–624005,India

[4]Sathyabama University, Chennai, India

[5]SKV Higher Sec School, Kandampalayam–637201, India

wmanonithi@gmail.com, *susairajendran@gmail.com

PACS 81.07.-b **DOI 10.17586/2220-8054-2016-7-4-711-723**

Titanium dioxide nanoparticles have been used to control corrosion of mild steel in well water in the absence and presence of an aqueous May flower extract. As the concentration of TiO_2 increases, the inhibition efficiency also increases. 100 ppm of TiO_2 offers 84 % inhibition efficiency. The addition of 10mlof May flower extract enhances the inhibition efficiency to 95 %. Adsorption of TiO_2 on the metal surface follows Langmuir adsorption isotherm. Polarization study reveals that the flower extract-TiO_2 system functions as mixed type of inhibitor, controlling both anodic and cathodic reactions. AC impedance spectra reveal the formation of a protective film on the metal surface. This technology may find application in cooling water systems and concrete technology.

Keywords: corrosion inhibition, nanoparticles, TiO_2, flower extract, *Delonix regia*, adsorption isotherm.

Received: 5 February 2016

Revised: 9 April 2016

1. Introduction

Nanotechnology is an emerging field through which new productions on nano scale can be manufactured. Producing a new generation of textiles which possess antimicrobial properties using nanoparticles has attracted a great deal of attention from both scientists and consumers in recent years [1,2]. Furthermore, metal nanoparticles show unique properties due to their peculiar electronic configuration, very large surface area and high amount of surface atoms [3]. For instance, metal nanoparticles show a broad absorption band in the visible region of the electromagnetic spectrum [4]. Some amazing properties of metals are used in order to improve the photocatalytic activities of semiconductors, such as TiO_2 and SiO_2, which are among the most efficient ones, resulting in better photocatalytic properties, even under visible rays [5]. Some noble metals, such as Ag [6], Au [7] and Pd [8] have stood the test of time in the field of producing nanocomposites.

Several nanoparticles have been used as corrosion inhibitors. As the particle size decreases, the inhibition efficiency increases because the surface area covered by the nanoparticles on the metal's surface increases. Nano-TiO_2 particles have improved the corrosion resistance of carbon steel [9], Ni-base alloys [10], aluminum surface [11]. A TiO_2 nanoparticle coating has been used to prevent biofilm formation in water and wastewater installations. Copper nanoparticles have improved the corrosion inhibition efficiency of carbon steel. Titanium dioxide (TiO_2) is a very promising metal oxide which has been widely studied as a photocatalyst for organic synthesis [12] and environmental cleaning processes [13]. Recent applications, based on the photocatalysis and photoactivity of TiO_2, include antifouling, antibacterial, deodorizing and self-cleaning functions [14]. In close connection with the developments in academic research, TiO_2 photocatalysis technology has also become more attractive in industrial applications due to its effectiveness, availability, low cost and chemical stability [15].

In this work, TiO_2 nanoparticles were prepared using commercially available titanyl chloride solution and characterization studies by SEM, EDS. The corrosion resistance of mild steel in well water in the presence of titanium dioxide nanoparticles and an aqueous extract of may flower (*Delonix regia)* by weight loss method, polarization study and AC impedance spectra.

2. Experimental methods

2.1. Preparation of TiO_2 nano particles

Stage1: 50 g of titanium tetrachloride of AR grade was chilled in a freezer overnight and placed in a 500 ml flask. To this, 250 ml of deionized ice water was added drop-wise while continuously shaking the flask. The reaction produced an aqueous titanyl chloride.

Stage 2: The titanyl chloride solution was then added dropwise to a solution of 10 ml glycolic acid (Merck, 70 %) in a flask. Deionized water was added dropwise until a total volume of 300 ml was reached, while continuously shaking the flasks.

Stage 3: The precursor solution was then allowed to stand for 15 days at room temperature, until white precipitates formed. The precipitates were filtered using a pressure filtration unit and then washed with water and methanol [16].

2.2. SEM and EDAX spectra

A few drops of the solution containing TiO_2 nanoparticles were dried on a glass plate. The solid mass was used for recording SEM and EDAX. SEM and EDAX were recorded in field Emission Scanning Electron Microscopy (FESEM-SUPRA 5S)-(ARLZEISS, GERMANY).

2.3. Preparation of the specimen

Mild steel specimens (0.026 % S, 0.06 % P, 0.4 % Mn, 0.1 % C, and the rest iron) of the dimensions 1.0 cm ×4.0 cm × 0.2 cm were polished to a mirror finish and degreased with trichloroethylene and used for the weight loss method and surface examination studies.

2.4. Preparation of May flower extract

An aqueous extract of May flower (*Delonix regia*) was prepared by grinding 10 g of flower using sterile mortar and pestle, filtered through three layers of muslin cloth and make up to 100 ml using double distilled water. This aqueous extract was used as corrosion inhibitor. The image of May flower are shown in Fig. 1.

FIG. 1. May flower

2.5. Determination of corrosion rate

The weighed specimens in triplicate were suspended by means of glass hooks in 100 ml of well water containing various concentration of TiO_2 nanoparticles in the presence and absence of may flower extract (FE) for one day. The specimens were taken out, washed in running water, dried, and weighed. From the change in weights of the specimens, corrosion rates were calculated using the following relationship:

$$CR = [(Weight\ loss\ in\ mg)/(Area\ of\ the\ dspecimens\ in\ dm^2 \times Immersion\ periods\ in\ days)]\ mdd. \quad (1)$$

Corrosion inhibition efficiency (IE %) was then calculated using the equation:

$$I.E. = 100[1 - (W_2/W_1)]\%, \quad (2)$$

where, W_1 – corrosion rate in the absence of the inhibitor, and W_2 – corrosion rate in the presence of the inhibitor.

2.6. Potentiodynamic polarization

Polarization studies were carried out in a CHI – Electrochemical workstation with impedance, Model 660A. A three-electrode cell assembly was used. The three electrode assembly is shown in Fig. 2. The working electrode was mild steel. A saturated calomel electrode (SCE) was the reference electrode and platinum was the counter electrode. From the polarization study, corrosion parameters such as corrosion potential (E_{corr}), corrosion current (I_{corr}) and Tafel slopes (anodic = ba and cathodic =bc) and Linear polarization resistance (*LPR*) were calculated. The scan rate (V/S) was 0.01 and the hold time at (Efcs) was zero and quit time(s) was two.

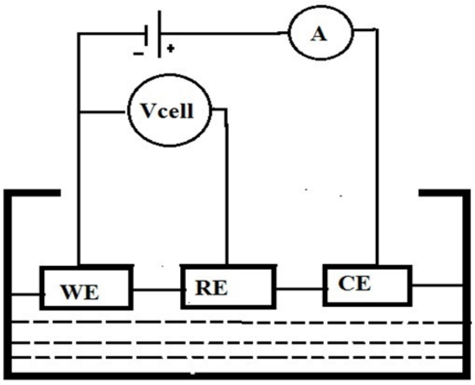

FIG. 2. Circuit diagram of three-electrode cell assembly. WE- working electrode (mild steel), RE-Reference electrode (saturated calomel electrode (SCE)), CE- Counter electrode (platinum)

2.7. AC impedance spectra

AC impedance spectral studies were carried out in a CHI – Electrochemical workstation with impedance, Model 660A. A three-electrode cell assembly was used. The working electrode was mild steel. A saturated calomel electrode (SCE) was the reference electrode and platinum was the counter electrode. The real part (Z') and imaginary part (Z") of the cell impedance were measured in ohms at various frequencies. Values of the charge transfer resistance (R_t) and the double layer capacitance (C_{dl}) were calculated.

3. Results and Discussion

3.1. Characterization of TiO_2 nanoparticles

The TiO_2 nanoparticles have been synthesized. The SEM image of the TiO_2 nanoparticles is shown in Fig. 3. The quantitative results for TiO_2 are shown in Fig. 4.

3.2. Analysis of EDS

EDAX spectrum of TiO_2 nanoparticles is shown in Fig. 5. The data derived from the spectra are given in Table 1. The processing option during recording the spectrum was normalized (all elements were analyzed). The number of iterations was 3. The following standards were used: carbon – $CaCO_3$; oxygen – SiO_2; titanium – Ti. The size of TiO_2 nanoparticles is shown in Fig. 6. The size of TiO_2 nanoparticles was shown to range from 70 – 90 nm.

TABLE 1. Date derived from EDAX

Element	Weight%	Atomic%
O K	9.03	22.90
Ti K	90.97	77.10
Totals	100.00	

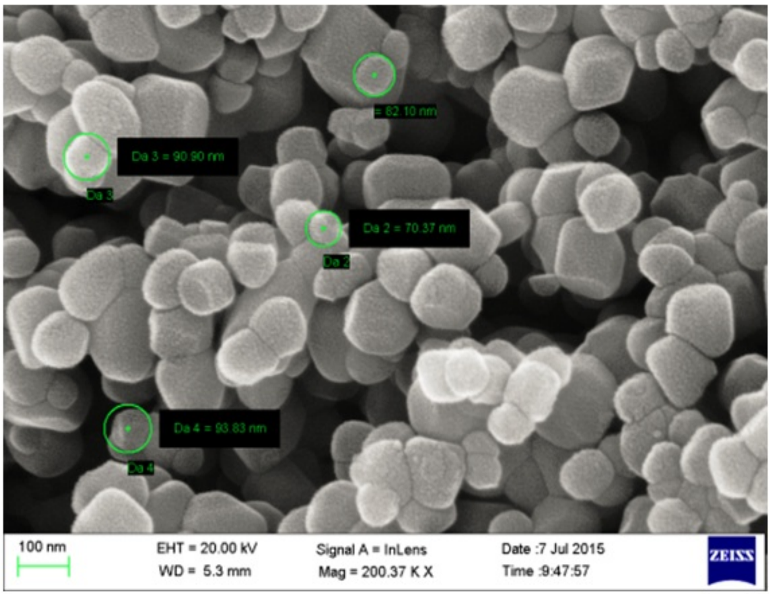

FIG. 3. The SEM image of TiO_2 nanoparticles

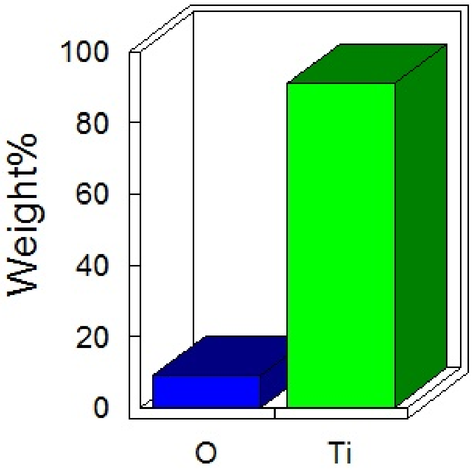

FIG. 4. The quantitative results of TiO_2 nanoparticles

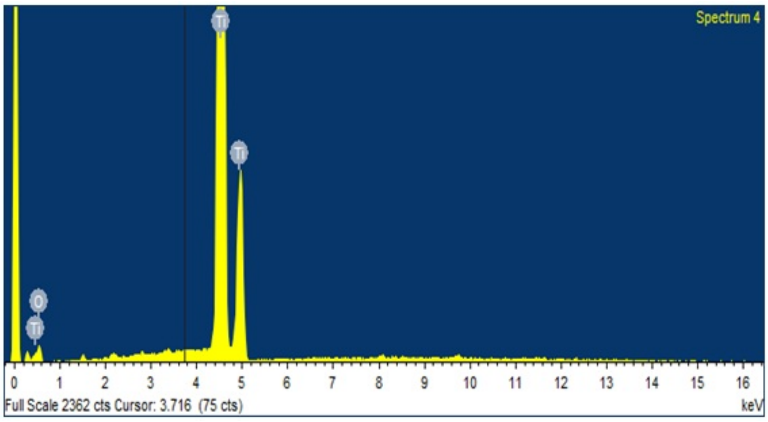

FIG. 5. EDAX spectrum of TiO_2 nanoparticles

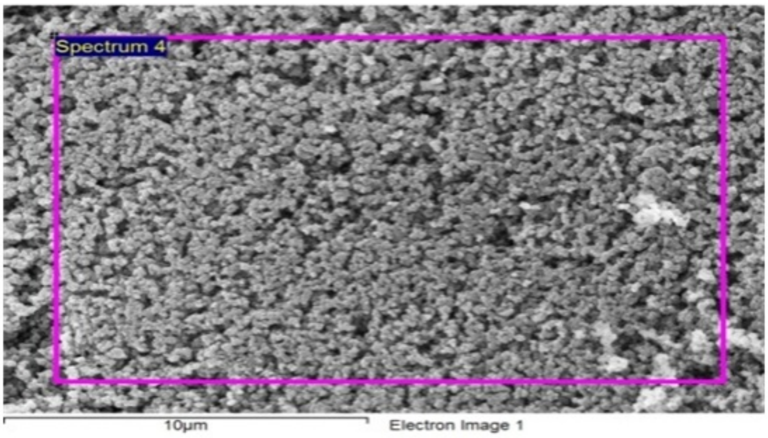

FIG. 6. The size of TiO_2 nanoparticles

4. Weight loss method

4.1. Corrosion inhibition by TiO_2 system

Corrosion rates (CR) of mild steel immersed in well water (WW) in the absence and presence of TiO_2 and the inhibition efficiencies (IE) obtained by weight loss method are given in Table 2. It was observed that when 100 ppm of TiO_2 was added to well water, the corrosion rate decreases to a great extent; and an inhibition efficiency of 80 % was obtained. This is due to the adsorption of TiO_2 nanoparticles on the metal's surface. As the concentration of TiO_2 increases, the corrosion rate decreases and the inhibition efficiency increases (Fig. 7) [17–20].

TABLE 2. Corrosion rates (CR) of mild steel immersed in well water (WW) in the absence and presence of TiO_2 and the inhibition efficiencies (IE) obtained by the weight loss method

TiO_2 Ppm	CR mdd	IE %
0	23.45	-
0	13.93	41
40	11.26	52
60	7.50	68
80	6.80	71
100	4.69	80

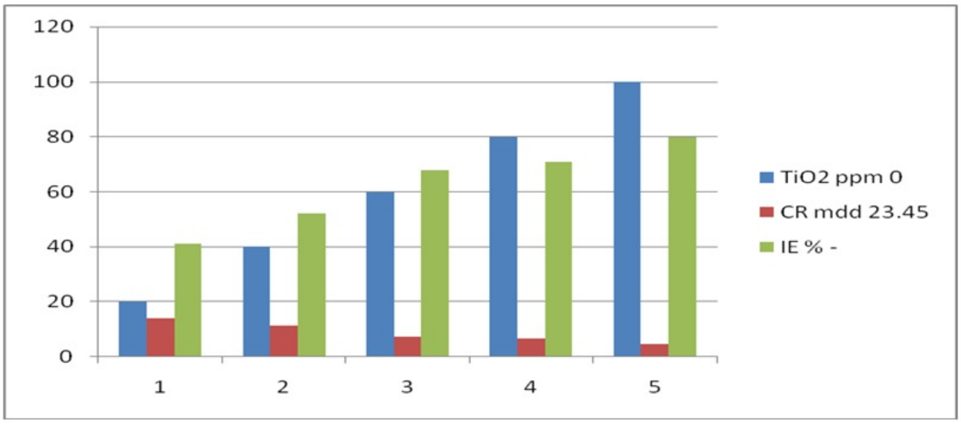

FIG. 7. Correlation between concentration of TiO_2, corrosion rate and inhibition efficiency

4.2. Corrosion inhibition by May flower extract (FE) system

Corrosion rates (CR) of mild steel immersed in well water (WW) in the absence and presence of May flower extract and the inhibition efficiencies (IE) obtained by weight loss method are given in Table 3. It was observed that when 10 ml of flower extract was added to well water, the corrosion rate decreases significantly and an inhibition efficiency of 84 % was obtained. This is due to the adsorption of active principles of May flower extract on the metal surface. As the concentration of flower extract increases, the corrosion rate decreases and the inhibition efficiency increases. (Fig. 8).

TABLE 3. Corrosion rates (CR) of mild steel immersed in well water (WW) in the absence and presence of May flower extract and the inhibition efficiencies (IE) obtained by weight loss method

FE ml	CR mdd	IE %
0	23.45	-
2	12.66	46
4	10.55	55
6	7.97	66
8	6.10	74
10	3.75	84

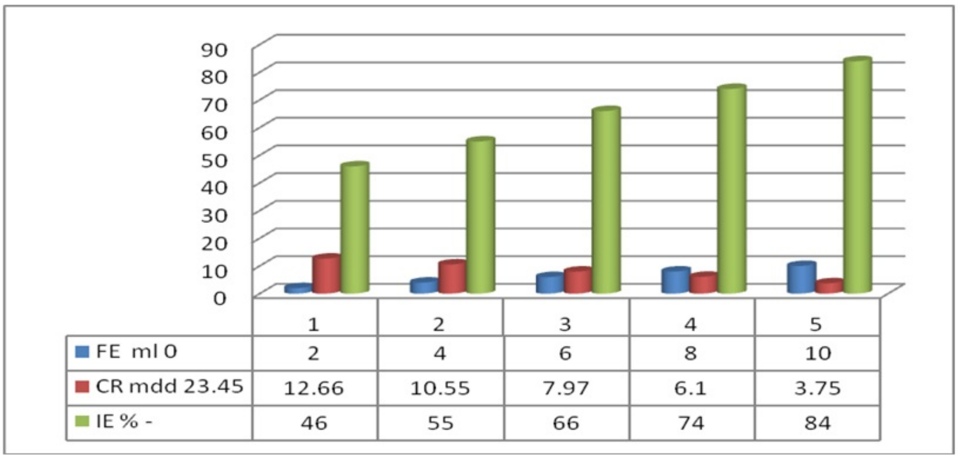

FIG. 8. Correlation between concentration of May flower extract, corrosion rate and Inhibition Efficiency (IE)

4.3. Corrosion inhibition by WW+ TiO_2 100 ppm + 10 ml of May FE System

Corrosion rates (CR) of mild steel immersed in well water (WW) in the absence and presence of TiO_2 and an aqueous extract of May flower extract (FE) and the inhibition efficiencies (IE) obtained by weight loss method are given in Table 4. It was observed that when 100 ppm of TiO_2 was added to well water, the corrosion rate significantly decreased, and an inhibition efficiency of 80 % was obtained. This is due to the adsorption of TiO_2 nanoparticles on the metal surface. When 10 ml of flower extract was added to well water, the corrosion inhibition efficiency was 84 %. When both 100 ppm of TiO_2 and 10 ml May flower extract were added, the IE was 95 %. Hence, one can conclude that the WW+ TiO_2 100 ppm + 10 ml of FE system offers the best inhibition efficiency. TiO_2 is adsorbed on the metal surface and offers corrosion protection by preventing water molecules and aggressive ions from reaching the metal surface. The active principles of FE are adsorbed on the TiO_2 layers. These layers are hydrophobic in nature and prevent water molecules reaching the metal surface (Fig. 9).

5. Adsorption isotherm for TiO_2 system

The adsorption of inhibitor molecules (TiO_2 ppm) obeys Langmuir Adsorption Isotherm (Fig. 10). A graph was made by plotting C vs C/θ, where C is concentration of inhibitor and θ is surface coverage. A linear plot

TABLE 4. Corrosion rates (CR) of mild steel immersed in well water (WW) in the absence and presence of TiO_2 and an aqueous May flower extract (FE) and the inhibition efficiencies (IE) obtained by weight loss method

System	**CR mdd**	**IE %**
WW	23.45	-
WW+$TiO_2$100 ppm	4.71	80
WW+10ml of FE	3.77	84
WW+$TiO_2$100 ppm + 10ml of FE	1.18	95

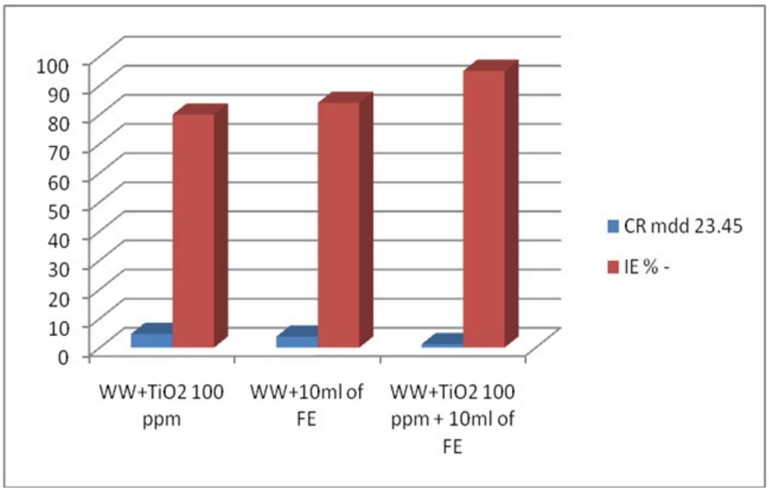

FIG. 9. Correlation between corrosion rates and inhibition efficiencies for various systems

was obtained with R^2 value of 0.980. This indicated that the adsorption of molecules on the metal surface obeyed the Langmuir adsorption isotherm. The slope was 0.940 and intercept was 33.88. The Langmuir constant, K (calculated from the relation Intercept = log K), was found to be 7.59×10^{33}.

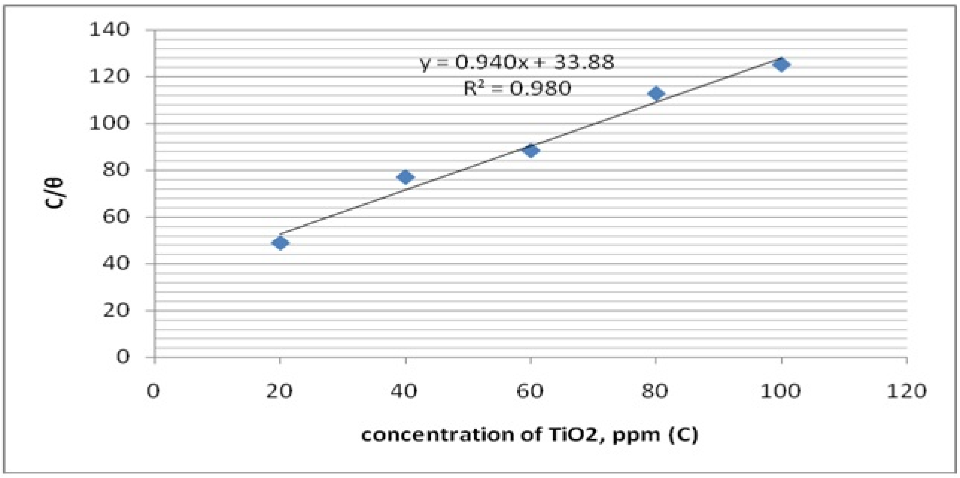

FIG. 10. Langmuir adsorption isotherm for TiO_2 system

Since the Langmuir adsorption isotherm is obeyed, it implies that:

- The adsorption of a single adsorbate onto a series of equivalent sites on the surface of the solid.
- The surface containing the adsorbing sites is perfectly flat plane with no corrugations (assuming an homogeneous surface).

- The adsorbing molecule adsorbs into an immobile state.
- All sites are equivalent.
- Each site can hold at most one molecule of inhibitor (monolayer coverage only).
- There are no interactions between adsorbed molecules on adjacent sites.
- The formation of Langmuir monolayers by adsorption onto a surface dramatically reduces the entropy of the molecular system

5.1. Adsorption isotherm for May flower system

The adsorption of inhibitor molecules (May flower extract in ml) obey Langmuir Adsorption Isotherm (Fig. 11). A graph was made by plotting C vs C/θ, where C is concentration of inhibitor and θ is surface coverage. A linear plot was obtained with R^2 value of 0.970. This indicated that the adsorption of molecules on the metal surface obeyed the Langmuir adsorption isotherm. The slope was 0.933 and the intercept was 3.088. The Langmuir constant, K (calculated from the relation Intercept = log K) was found to be 1225×10^3.

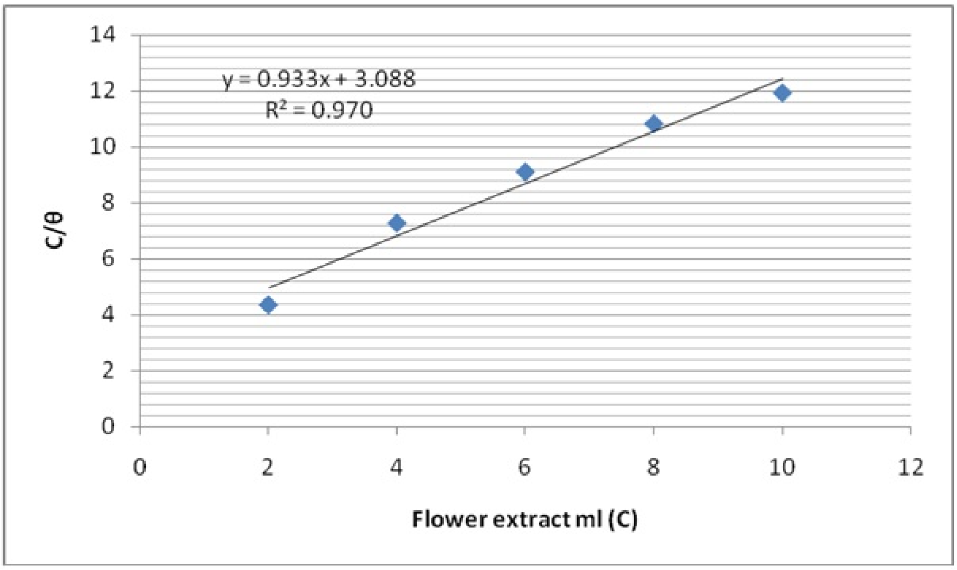

FIG. 11. Langmuir adsorption isotherm for May flower system

6. Potentiodynamic polarization study

Electrochemical analyses, such as Polarization study and AC impedance spectra, have been used to investigate the corrosion resistance of metals [20–25].

In the polarization study, if corrosion resistance increases, linear polarization Resistance (LPR) value increases and corrosion current decreases. In the present study, the corrosion resistance of mild steel immersed in well water in the presence and absence of an aqueous May flower extract and TiO_2 has been investigated by a potentiodynamic polarization study (Fig. 12). The corrosion parameters such as corrosion potential (Ecorr), Tafel slopes (bc = cathodic, ba = anodic), LPR values and corrosion current (Icorr), derived from the TAFEL plots, are given in the Table 5.

When mild steel was immersed in well water (WW), the corrosion potential was −631 mV vs SCE, the LPR value was 7249 ohm cm^2 and the corrosion current was 5.268×10^{-6} A/cm^2.

It is interesting to note that when mild steel was immersed in well water containing 100 ppm of TiO_2, the corrosion resistance of mild steel increased. This was due to the presence of TiO_2 nanoparticles in the medium. The nanoparticles were adsorbed onto the metal surface, forming a protective film. Hence, corrosion resistance increased. This was revealed by the fact that when the mild steel was immersed in WW containing TiO_2, the LPR value increased from 7249 ohm cm^2 to 8350 ohm cm^2. The corrosion current value decreased from 5.268×10^{-6} A/cm^2 to 1.587×10^{-6} A/cm^2.

When mild steel was immersed in WW+10 ml of FE + system, it was inferred that the corrosion resistance of mild steel increased. This was revealed by the fact that, in presence of flower extract, the LPR value was high (30994 ohm cm^2); the corrosion current decreased to 1.045×10^{-6} A/cm^2 and the corrosion potential shifted

TABLE 5. Corrosion parameters of mild steel immersed in well water (WW) in the absence and presence of TiO_2 and an aqueous flower extract (FE), obtained by polarization study

System	**E_{corr} mV vs SCE**	**b_c mV/decade**	**b_a mV/decade**	**LPR ohm cm^2**	**I_{corr} A/cm^2**
WW	−631	202	155	7249	5.268×10^{-6}
WW+TiO_2 100 ppm	−663	221	120	8350	1.587×10^{-6}
WW+10 ml of FE	−670	199	119	30994	1.045×10^{-6}
WW+TiO_2 100 ppm + 10 ml of FE	−641	186	165	36770	1.035×10^{-6}

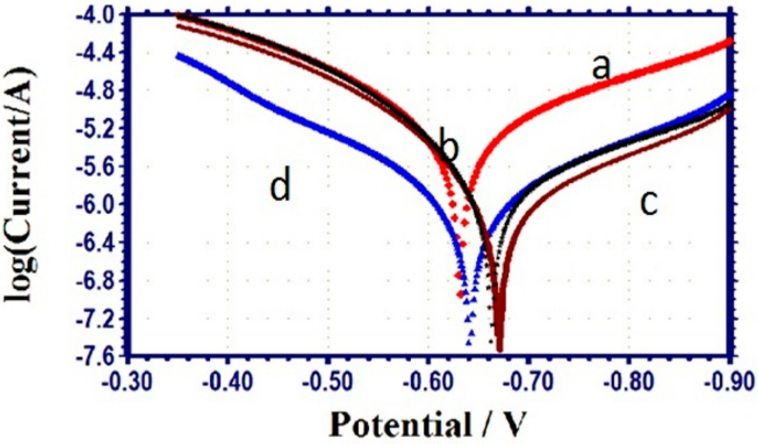

FIG. 12. Polarization curves of mild steel immersed in various test solutions (a) WW, (b) WW+TiO_2 100 ppm, (c) WW+10 ml of FE, (d) WW+TiO_2 100 ppm + 10 ml of FE

to the cathodic side (from −631 to −641 mV vs SCE). This means that the cathodic reaction was controlled predominantly. The active principle present in the flower extract forms a protective film on the metal surface. The transfer of electrons from the metal to the bulk of the system was prevented. Because of the necessity of electrons, the cathodic reaction, which involves the interaction of electrons with oxygen and water, is minimized, thus, the formation of hydroxide ions is reduced.

When mild steel was immersed in theWW+10 ml of FE + TiO_2 100 ppm system, the corrosion resistance of mild steel further appeared to be further increased. This is revealed by the fact that, in presence of flower extract, the LPR value was very high (36770 ohm cm^2); the corrosion current decreased to 1.035×10^{-6} A/cm^2 and the corrosion potential shifted to the cathodic side (from −631 to −670 mV vs SCE). This means that the cathodic reaction was controlled predominantly. The active principle present in the May flower extract forms a protective film on the metal surface. The transfer of electrons from the metal to the bulk of the system was prevented. Because of the need for electrons, the cathodic reaction, which involves the interaction of electrons with oxygen and water, is limited, thus, the formation of hydroxide ions is reduced. However, when compared with the WW+10 ml of FE system, (−670 mV vs SCE), the shift is anodic (−641 mV vs SCE). This shift revealed that in presence of TiO_2, the anodic reaction is also controlled. Moreover, when compared with −631 mV vs SCE, this shift is very small. So it can be considered that the "WW+10 ml of FE + TiO_2 100 ppm system" functions as a mixed inhibitor system, controlling both the anodic and cathodic reactions. **Thus, the polarization study leads one to the conclusion that the corrosion resistance of mild steel in various test solutions decreases in the order:**

WW+$TiO_2$100 ppm+10 ml of FE system>WW+10 ml of FE>WW+$TiO_2$100 ppm>WW

From the data, one can conclude that the WW+$TiO_2$100 ppm + 10ml of FE system offers better inhibition efficiency than other systems.

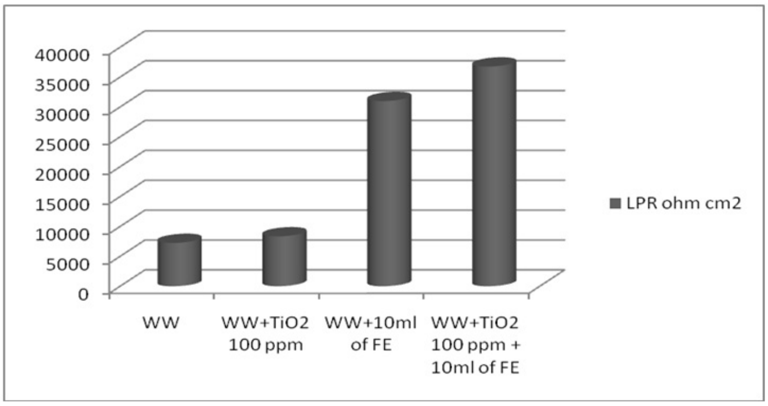

FIG. 13. Comparison of LPR values of various systems

6.1. AC impedance spectra

AC impedance spectra have been used to investigate the corrosion resistance of metals. When corrosion resistance increases, the charge transfer resistance values (R_t) increase, impedance values increase and double layer capacitance values (c_{dl}) decrease [26–30]. AC impedance spectra of mild steel immersed in various test solution are shown in Figs. 14 – 17. Nyquist plots are shown in (Fig. 14), and Bode plots are shown in Fig. 15 – 17. The corrosion parameters are given in Table 6.

TABLE 6. Corrosion parameters of mild steel immersed in well water (WW) in the absence and presence of TiO_2 and an aqueous May flower extract (FE), obtained by AC impedance spectra

System	R_t ohm cm^2	C_{dl} F/cm^2	Impedance Log(z/ohm)
WW	181	2.78×10^{-8}	2.543
WW+$TiO_2$100 ppm	782	0.639×10^{-8}	3.152
WW+10 ml of FE	1021	0.490×10^{-8}	3.251
WW+$TiO_2$100 ppm + 10 ml of FE	1080	0.463×10^{-8}	3.261

It was observed from Table 6 that when the inhibitor (TiO_2 100 ppm) was added to well water, the charge transfer resistance (R_t) increased from 181 Ω cm^2 to 782 Ω cm^2. The C_{dl} value decreased from 2.78×10^{-8} F/cm^2 to 0.639×10^{-8} F/cm^2 and the impedance value increased from 2.543 to 3.152. These results lead one to conclude that a protective film was formed on the metal surface. Nanoparticles of TiO_2 have adsorbed on the metal surface forming protective film. The surface becomes hydrophobic, hindering water molecules and aggressive ions from reaching the surface, thus protecting the metal from corrosion.

When the inhibitor (10 ml of may flower extract) was added to well water, the charge transfer resistance (R_t) increased from 181Ω cm^2 to 1021 Ω cm^2, the C_{dl} value decreased from 2.78×10^{-8}F/cm^2 to 0.490×10^{-8} F/cm^2 and the impedance value increased from 2.543 to 3.251. These results would seem to indicate that a protective film was formed on the metal surface. This film is more compact and hydrophobic than the previous case, which is why the R_t value of this system is higher than that of the previous system.

It was observed that the WW+$TiO_2$100 ppm + 10 ml of FE system is more corrosion resistant than the previous system because for this system, the R_t value increases to 1080 Ω cm^2 and the C_{dl} value decreases to 0.463×10^{-8} F/cm^2 and the impedance value increases to 3.261. It seems that the flower extract and TiO_2 particles are adsorbed jointly on the metal surface and thus form a better protective film. Thus, AC impedance spectra lead to the conclusion that corrosion resistance of mild steel in various test solutions decreases in the following order:

WW+TiO_2 100 ppm+10 ml of FE system>WW+10 ml of FE>WW+TiO_2 100 ppm>WW.

The WW+TiO_2 100 ppm + 10 ml of FE system offers better inhibition efficiency than other systems. This view is in agreement with the polarization study results.

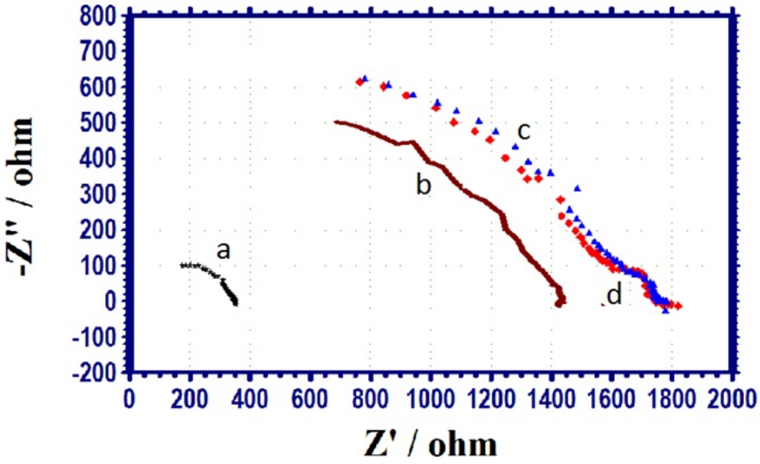

FIG. 14. AC impedance spectra (Nyquist Plots) of mild steel immersed in various test solutions (a) WW, (b) WW+TiO_2 100 ppm, (c) WW+10 ml of FE, (d) WW+TiO_2 100 ppm + 10 ml of FE

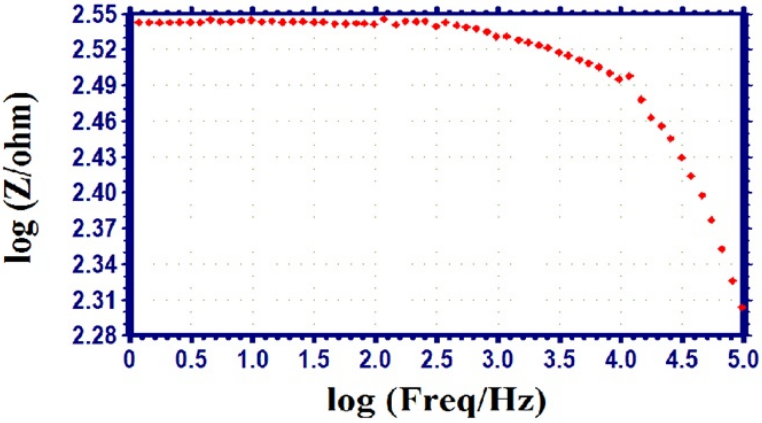

FIG. 15. AC impedance spectrum (Bode Plot- impedance) of mild steel immersed in well water (a) WW

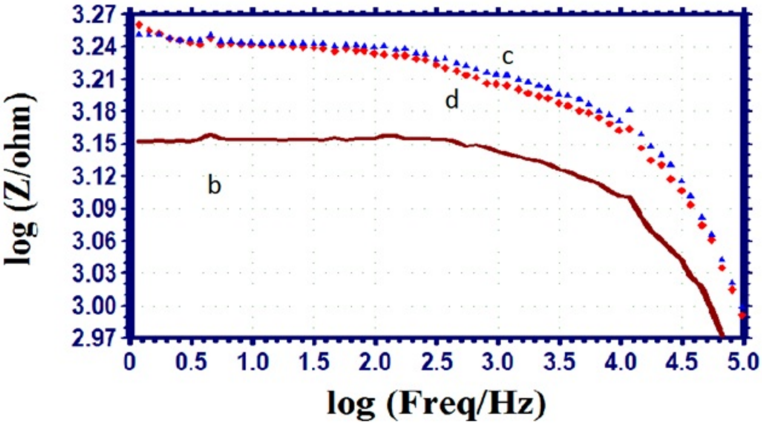

FIG. 16. AC impedance spectra (Bode Plots-impedance) of mild steel immersed in various test-solutions (b) WW+TiO_2 100 ppm, (c) WW+10 ml of FE, (d) WW+TiO_2 100 ppm + 10 ml of FE

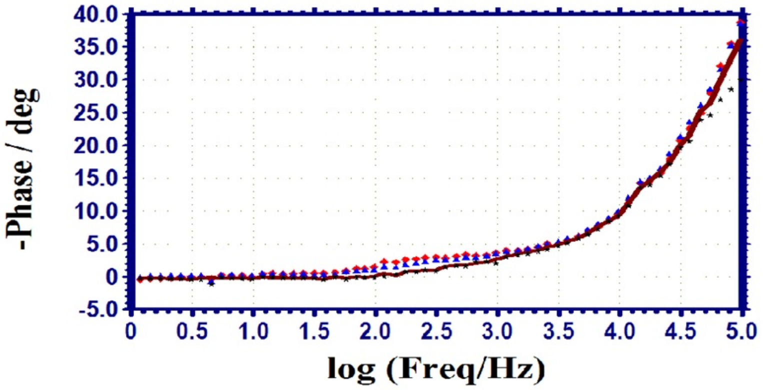

FIG. 17. AC impedance spectra (Bode Plots-phase angle) of mild steel immersed in various test Solutions. black line – WW, grey line – WW+ TiO_2 100 ppm, blue line – WW+ 10 ml of FE, red line – WW+TiO_2 100 ppm + 10 ml of FE

7. Conclusion

The present study leads to the following conclusions:

- Titanium dioxide nanoparticles, along with an aqueous may flower extract has been synthesized successfully.
- The formulation consisting of 100 ppm of TiO_2 nanoparticles and 10 ml may flower extract afforded a 95 % IE for mild steel immersed in well water.
- Polarization study reveals that 100 ppm of TiO_2 nanoparticles and 10 ml may flower extract functions as mixed inhibitor system, controlling both anodic and cathodic reactions.
- AC impedance spectra reveal that the formation of protective film on the metal's surface.

Acknowledgement

The authors are thankful to their respective management and Defence Research and Development Organisation, New Delhi.

References

[1] Lee H.J., Yeo S.Y., Jeong S.H. Antribacterial effect of nanosized silver colloidal solution on textile fabrics. *J. Master. Sci*, 2003, **38**, P. 219–2204.

[2] Alimohammadi F. *Stabilization of silver nanoparticles and antibacterial characterization on the cotton surface against washing*. M.Sc Thesis, Islamic Azad University Tehran South Brach, 2009.

[3] Aiken J.D., Finke R.G. A review of modern transition-metal nanoclusters: their synthesis, characterization, and applications in catalysis. *J. Mol. Catal, A:Chem*, 1999, **145**, P. 1–44.

[4] Liu R., Chen H., Hu S. Synthesis and characterization of nanometals with coreshell structure. *China Particuol*, 2004, **2**(4), P. 160–163.

[5] Sung-Suh H.M., Choi J.R., Hah H.J., Koo S.M., Bae Y.C. Comparison of Ag deposition effects on the photo catalytic activity of nanoparticle TiO_2, under visible and UV light irradiation. *J. Photochem. Photobiol. A.*, 2004, **163**, P. 37–44.

[6] Valentine Rupa A., Manikandan D., Divaker D., Sivakumar T. Effect of deposition of Ag on TiO_2 nanoparticles on the photodegradation of Reactive Yellow-17. *J. Hazard, Mater.*, 2007, **147**, P. 906–913.

[7] Uddin M.J., Cesano F., Scarano D., Bonino F., Agostini G., Spoto G., Bordiga S., Zecchina A. Cotton textile fibers coated by Au/TiO_2 films: Synthesis characterization and self-cleaning properties. *J. Photochem. Photobiol. A.*, 2008, **199**, P. 64–72.

[8] Sclafant A., Herrmann J.M. Influence of metallic silver and of platinum-silver bimetallic deposits on the photocatalytic activity of titania (anatase and rutile) inorganic and aqueous media. *J. Photochem. Photobiol. A.*, 1998, **113**, P. 181–188.

[9] Deyab M.A., Keera S.T. Effect of nano-TiO_2 particles size on the corrosion resistance of alkyl coating. *Chemistry and Physics*, 2014, **146**(3), P. 406–411.

[10] Kim K.M., Lee E.H., Hur D.H. Corrosion behavior on Ni-base alloys applied with Nano-TiO_2 in high temperature caustic water. *Current Nanoscience*, 2014, **10**(1), P. 89–93.

[11] Liu T., Qiang L. Research on inhibition marine microbial adherence of a novel nano-TiO_2 coating on aluminium. *Advanced Materials Research*, 2012, **557-559**, P. 1687–1690.

[12] Sakata T., Kawai T., Hashimoto K. Catalytic Properties of Ruthenium Oxide on n-Type Semi-conductors under Illumination. *J. Phys. Chem.*, 1984, **88**, P. 2344–2350.

[13] Fu X.Z., Zeltner W.A., Anderson M.A. Photocatalytic Generation of H_2 from Seawater. *Appl. Catal.,* 1995, **B6**, P. 209–220.

[14] Sopyan I., Watanabe M., Murasawa S., Hashimoto K., Fujishima A. A film-type photocatalyst incorporating highly active TiO_2 powder and fluororesin binder: photocatalytic activity and long-term stability. *J. Electroanal. Chem.*, 1996, **415**, P. 183–186.

[15] Zhang X., Fujishima A., Alexei M.J., Emeline V. Murakami T. Double-Layered TiO_2-SiO_2. Nanostructured Films with Self-Cleaning and Antireflective Properties. *J.Phys Chem*, 2006, **B110**, P. 25142–25148.

[16] Zhou et al. Titanium dioxide nanoparticles and nanoparticle suspensions and methods of making the same. US Patent 7326399 B2, 2008.

[17] Hansoon C.M. Volume Relationship for C-S-H Formation Based on General Concepts. *Cem. Concr. Res*, 1984, **14**, P. 574.

[18] Nakayama N., Obuchi A. Inhibitory effects of 5-aminouracil on cathodic reactions of steels in saturated $Ca(OH)_2$ solution. *Corros. Sci.*, 2003, **45**, P. 2075–2092.

[19] Manivannan M., Rajendran S. Investcation of inhibitive action of urea-Zn^{2+} system in the corrosion control of carbon steel in sea water. *International of Engineering science and Technology*, 2011, **3**, P. 19–23.

[20] Johnsirani V., Sathiyabama J., Rajendran S, Shanthi T., Muthumegala T.S., Krishnaveni A. Inhibitive action of malachite green-Zn^{2+} system. *Bulgarian Chemical Communication*, 2012, **44**, P. 41–51.

[21] Epshiba R., Peter Pascal Regis A., Rajendran S. Inhibition Of Corrosion Of Carbon Steel In A Well Water By Sodium Molybdate – Zn^{2+} System. *Int. J. Nano. Corr. Sci. Engg.*, 2014, **1**(1), P. 1–11.

[22] Kavitha N., Manjula P. Corrosion Inhibition of Water Hyacinth Leaves, Zn^{2+} and TSC on Mild Steel in neutral aqueous medium. *Int. J. Nano. Corr. Sci. Engg.*, 2014, **1**(1), P. 31–38.

[23] Nagalakshmi R., Nagarajan L., Joseph Rathish R., Santhana Prabha S., Vijaya N., Jeyasundari J., Rajendran S. Corrosion Resistance of SS316l In Artificial Urine In Presence Of D-Glucose. *Int. J. Nano. Corr. Sci. Engg.*, 2014, **1**(1), P. 39–49.

[24] Angelin Thangakani J., Rajendran S., Sathiabama J., M.Joany R. Joseph Rathis R., Santhana Prabha S. Inhibition of Corrosion of Carbon Steel In Aqueous Solution Containing Low Chloride Ion By Glycine – Zn^{2+} System. *Int. J. Nano. Corr. Sci. Engg.*, 2014, **1**(1), P. 50-62.

[25] Nithya A., Shanthy P., Vijaya NJoseph Rathish. R., Santhana Prabha S., Joany R.M., Rajendran S. Inhibition of Corrosion of Aluminium By An Aqueous Extract of Beetroot (Betanin), *Int. J. Nano Corr. Sci. Engg.*, 2015, **2**(1), P. 1–11.

[26] Gowrani T., Manjula P., Nirmala Baby C. Manonmani, Sudha K.N., Vennila R. Thermodynamical Analysis of MBTA on The Corrosion Inhibition of Brass In 3 % NaCl Medium. *Int. J. Nano. Corr. Sci. Engg.*, 2015, **2**(1), P. 12–21.

[27] Namita K., Johar K., Bhrara R., Epshiba R., Singh G. Effect Of Polyethoxyethylene N, N, N‘ 1, 3 Diamino Propane on The Corrosion of Mild Steel In Acidic Solutions. *Int. J. Nano Corr. Sci. Engg.*, 2015, **2**(1), P. 22–31.

[28] Christy Catherine Mary A., Rajendran S., Hameed Al-Hashem, Joseph Rathish R., Umasankareswari T., Jeyasundari J. Corrosion Resistance Of Mild Steel In Simulated Produced Water In Presence Of Sodium Potassium Tartrate. *Int. J. Nano Corr. Sci. Engg.*, 2015, **2**(1), P. 42–50.

[29] Sangeetha M.,Rajendran S., Sathiyabama J., Umasankareswari T., Krishnaveni A., Joany R.M., *Int. J. Nano. Corr. Sci. Engg*, 2015, **2**(3), P. 14–21.

[30] Nithya Devi P., Sathiyabama J., Rajendran S. Joseph Rathish R., Santhana Prabha S. Influence of citric acid-Zn^{2+} System on Inhibition of Corrosion of Mild Steel in Simulated Concrete Pore Solution. *Int. J. Nano Corr. Sci. Engg.*, 2015, **2**(3), P. 1–13.

NANOSYSTEMS: PHYSICS, CHEMISTRY, MATHEMATICS, 2016, 7 (4), P. 724–727

Cashew nut shells as source of chemicals for preparation of chalcogenide nanoparticles

E. B. Mubofu[1,*], S. Mlowe[1,2], N. Revaprasadu[2]
[1]Chemistry Department, University of Dar es Salaam, P.O. Box 35061, Dar es Salaam, Tanzania
[2]Chemistry Department, University of Zululand, Private Bag X1001, KwaDlangezwa, 3886, South Africa
*ebmubofu@gmail.com, ebmubofu@udsm.ac.tz, sixb2809@gmail.com, RevaprasaduN@unizulu.ac.za

PACS 81.07.-b **DOI 10.17586/2220-8054-2016-7-4-724-727**

Cashew nut shell wastes produced in cashew nut processing factories cause environmental problems. Currently, these wastes are being converted to a variety of bio-based chemicals and functional materials. Cashew nut shells (CNS) produce cashew nut shell liquid (CNSL), a dark reddish brown viscous liquid (*ca.* 30 – 35 wt. %) which is extracted from the soft honeycomb of the CNS. CNSL offers multitude interesting possibilities for the synthesis of speciality chemicals, high value products and polymers due to their functionalities. Our recent research have demonstrated that CNSL constituents can be transformed into diverse functional chemicals. This contribution will report on how cashew nut shells (an agro waste from cashew nut processing factories) have been employed to produce anacardic acid capped chalcogenide nanoparticles.

Keywords: anacardic acid, cashew nut shell liquid, chalcogenide, nanoparticles.

Received: 5 February 2016

Revised: 7 May 2016

1. Introduction

Metal chalcogenides quantum dots (QDs) or semiconducting nanocrystals are interesting due to their highly refined chemistry, availability, and super tunable optical and electronic properties suitable for variety of applications in different fields, such as photovoltaics, light-emitting devices, environmental sciences and nanomedicine [1–7]. Recently, increasing concern about the environment has led researchers to focus on 'green chemistry', i.e. the utilization of nontoxic chemicals, environmentally benign solvents and renewable materials. The aforementioned are some of the key issues that merit important consideration in a green synthesis strategy. In order to reduce the environmental and health effects associated with nanoparticle synthesis, greener synthetic routes are being investigated [8, 9]. Green chemistry aims at addressing ways to reduce environmental and health impacts of chemical production [10]. In the field of nanotechnology, green synthesis involves three key issues; "utilization of non-toxic chemicals, environmentally benign solvents, and renewable materials" [11].

Recently, researchers have begun using green renewable chemicals for the generation of inorganic nanostructures and materials. These chemicals have shown the capability to control architectures of materials at nanoscale level. Castor oil and ricinoleic acid [12], olive oil and oleic acid [13–16] and anacardic acid [17, 18] are some of the green chemicals that have been used as capping agents to fabricate nanoparticles. In the present communication, we extend our earlier work using cashew nut shell liquid extracts for the synthesis of metal chalcogenides (Cadmium and lead sulfide, selenide and telluride) nanoparticles via a solution-based technique. Synthetic methods based on naturally occurring resources not only provide an alternative, friendly means of obtaining these metal chalcogenides nanoparticles, but also have a well-defined size and morphology. The use of cashew nut shell liquid and its isolate, anacardic acid (Fig. 1), in nanoparticle synthesis is associated with their chemical structures, easy availability, non-toxicity, low cost, non-food competition, high boiling point and high viscosity.

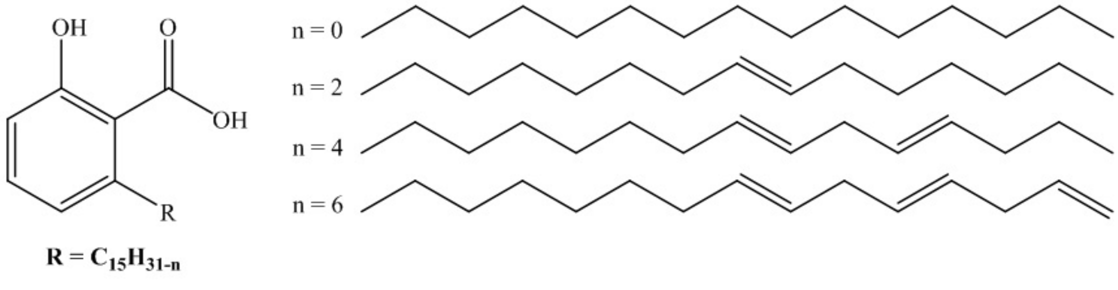

FIG. 1. Structure of Anacardic acids [19]

2. Experimental procedure

The chemical reduction and thermolysis route has been employed in this work. The cashew nut shell liquid and its isolate, anacardic acid, were extracted using a procedure reported by Paramashivappa *et al.* [20] with slight modifications reported by Lucio *et al.* [21]. Other chemicals, characterizations and procedures are similar to our earlier publications [17, 18]. The reaction scheme is shown in Fig. 2. The as-synthesized particles were characterized by TEM and HRTEM techniques.

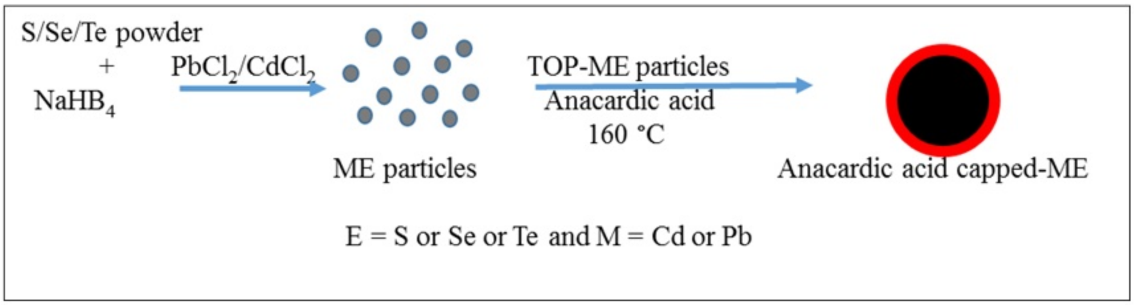

FIG. 2. Reaction scheme for the synthesis of anacardic acid-capped ME nanoparticles

2.1. Results and discussion

The morphology of the metal chalcogenide nanoparticles was studied by transmission electron microscopy (TEM). A typical TEM micrograph of the cadmium chalcogenide nanoparticles is given in Fig. 3. Fig. 3(a) shows anisotropic shaped anacardic acid-capped CdS nanoparticles, synthesized at 160 °C with average width of 11.8±2.4 nm and length 32.6±4.2 nm. CdSe (Fig. 3b) displayed uniform rod-shaped nanocrystals with a narrow size distribution on the TEM grid. A similar trend was observed for CdTe nanoparticles, showing rod shaped particles with an average width of 16.3±3.0 nm and length 48.4±4.5 nm (Fig. 3(c)). There is almost an equal inter-particle distance of approximately 3 nm for the CdSe and CdTe particles as observed from the TEM images.

The TEM image of the as-synthesised anacardic acid capped PbS (Fig. 4(a)) consists of small undefined spherical like particles with an average size of 9.8±1.8 nm. PbSe nanocrystals revealed the formation of small triangle-shaped particles with an average size of 12.6±3.1 nm (Fig. 4(b)). The presence of interspersed particles supports the fact that the formation of nanocrystals may be due to the influence of anacardic acid. While for PbTe nanoparticles (Fig. 4(c)), rod shaped and some cubic shaped particles, typical for PbTe [22] were formed. Rods of width 11.9 nm and length 37.8 nm and cubes of 20.9 nm were estimated.

3. Conclusion

Cadmium and lead chalcogenide (ME where M = cadmium or lead and E = S, Se or Te) nanoparticles have been successfully synthesized using anacardic acid as a coordinating solvent. The TEM studies reveal a mosaic-like pattern for all samples. Furthermore, monodispersed spherical to cubic shaped PbE nanoparticles were obtained. The results reveal that anacardic acid could be an effective and potential capping agent in the synthesis of metal chalcogenide nanoparticles. The method utilized an inexpensive and non-toxic naturallyoccurring acid as a capping agent which proved to be a good choice for high quality, monodispersed nanoparticles.

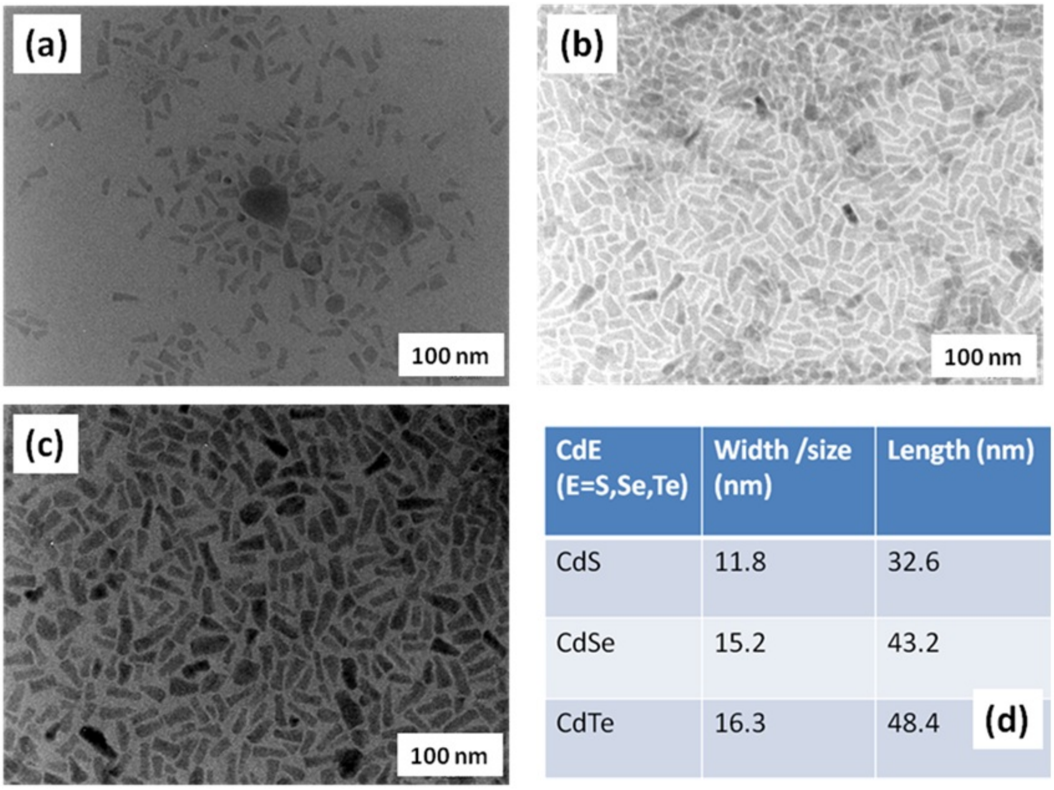

CdE (E=S,Se,Te)	Width /size (nm)	Length (nm)
CdS	11.8	32.6
CdSe	15.2	43.2
CdTe	16.3	48.4

FIG. 3. TEM images of anacardic acid capped CdS (a), CdSe (b) and CdTe (c), and table showing their sizes (d) synthesized at 160 °C

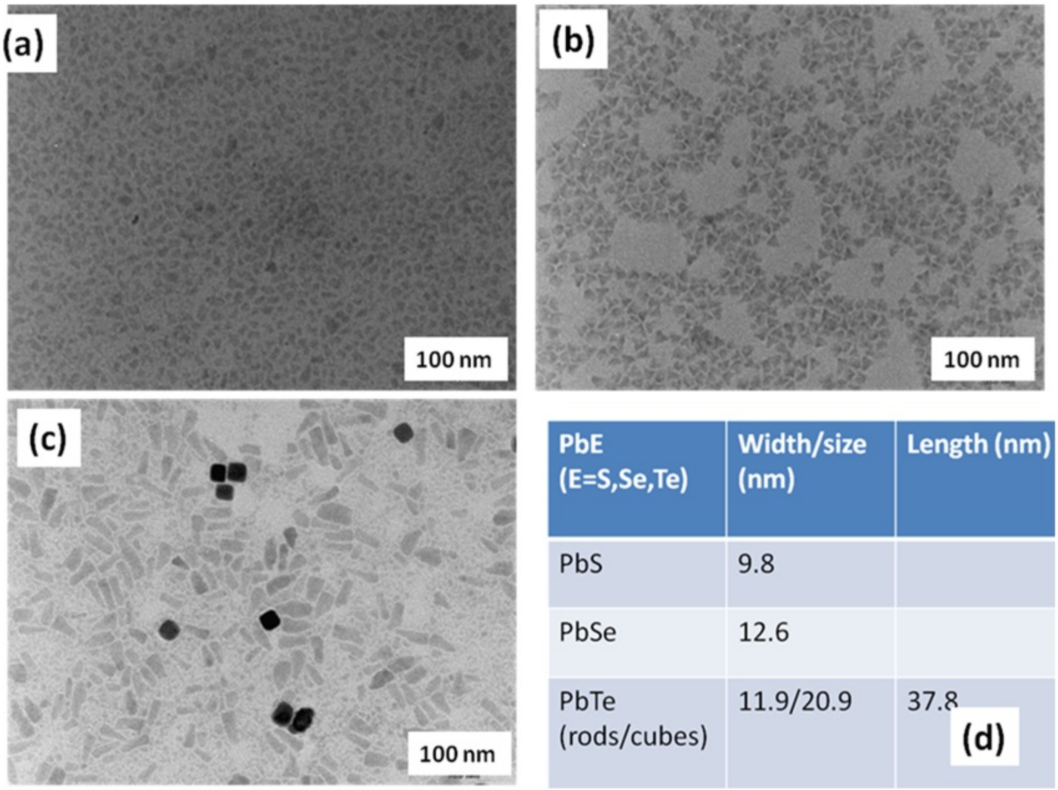

PbE (E=S,Se,Te)	Width/size (nm)	Length (nm)
PbS	9.8	
PbSe	12.6	
PbTe (rods/cubes)	11.9/20.9	37.8

FIG. 4. TEM images of anacardic acid capped PbS (a), PbSe (b) and PbTe (c), and table showing their sizes (d) synthesized at 160 °C

References

[1] Fan F-J., Wu L., Yu S-H. Energetic I–III–VI_2 and I_2–II–IV–VI_4 nanocrystals: synthesis, photovoltaic and thermoelectric applications. *Energy Environ. Sci.*, 2014, **7**, P. 190–208.

[2] Lewis D.J., Kevin P., Bakr O., Muryn C.A., Malik M.A. and O'Brien P. Routes to tin chalcogenide materials as thin films or nanoparticles: a potentially important class of semiconductor for sustainable solar energy conversion. *Inorg. Chem. Front.*, 2014, **1**, P. 577–598.

[3] Min Y., Moon G.D., Kim C-E., Lee J-H., Yang H., Soon A., Jeong U. Solution-based synthesis of anisotropic metal chalcogenide nanocrystals and their applications. *J. Mater. Chem. C*, 2014, **2**, P. 6222–6248.

[4] Santra P.K., Kamat P.V. Tandem-Layered Quantum Dot Solar Cells: Tuning the Photovoltaic Response with Luminescent Ternary Cadmium Chalcogenides. *J. Am. Chem. Soc.*, 2013, **135**(2), P. 877–885.

[5] Pan Z., Mora-Seró I., Shen Q., Zhang H., Li Y., Zhao K., Wang J., Zhong X., Bisquert J. High-Efficiency "Green" Quantum Dot Solar Cells. *J. Am. Chem. Soc.*, 2014, **136**(25), P. 9203–9210.

[6] Kaewsaneha C., Tangboriboonrat P., Polpanich D., Eissa M., Elaissari A. Janus Colloidal Particles: Preparation, Properties, and Biomedical Applications. *ACS Appl. Mater. Interfaces*, 2013, **5**(6), P. 1857–1869.

[7] Akhtar J., Malik M.A., O'Brien P., Wijayantha K.G.U., Dharmadasa R., Hardman S.J.O., Graham D.M., Spencer B.F., Stubbs S.K., Flavell W.R., Binks D.J., Sirotti F., El Kazzi M., Silly M. A greener route to photoelectrochemically active PbS nanoparticles. *J. Mater. Chem.*, 2010, **20**, P. 2336–2344.

[8] Da Silva E.C., Da Silva M.G., Meneghetti S.M., Machado G., Alencar M.A., Hickmann J.M., Meneghetti M.R. Synthesis of Colloids Based on Gold Nanoparticles Dispersed in Castor Oil. *J Nanopart Res.*, 2008, **10**, P. 201–208.

[9] Devendran P., Alagesan T., Ravindran T.R., Pandian K. Synthesis of Spherical CdS Quantum Dots Using Cadmium Diethyldithiocarbamate as Single Source Precursor in Olive Oil Medium. *Current Nanoscience.*, 2014, **10**, P. 302–307.

[10] Paul A., Warner T., John C. *Green Chemistry: Theory and Practice*. Oxford [England], New York: Oxford University Press, 1998.

[11] Raveendran P., Fu J., Wallen S.L. Completely "Green" Synthesis and Stabilization of Metal Nanoparticles. *J. Am. Chem. Soc.*, 2003, **125**, P. 13940–13941.

[12] Kyobe J.W., Mubofu E.B., Makame Y.M.M., Mlowe S., Revaprasadu N. CdSe quantum dots capped with naturally occurring biobased oils. *New J. Chem.*, 2015, DOI: 10.1039/C5NJ01460C.

[13] Nyamen L.D., Revaprasadu N., Ndifon P.T. Low temperature synthesis of PbS and CdS nanoparticles in olive oil. *Mater. Sci. Semicond. Process.*, **27**, P. 191–196, 2014.

[14] Devendran P., Alagesan T., Ravindran T.R., Pandian K. Synthesis of spherical CdS quantum dots using cadmium diethyldithiocarbamate as single source precursor in olive oil medium. *Curr. Nanosci.*, 2014, **10**, P. 302.

[15] Sapra S., Rogach A.L., Feldmann J. Phosphine-free synthesis of monodisperse CdSe nanocrystals in olive oil. *J. Mater. Chem.*, 2006, **16**, P. 3391–3395.

[16] Chen J., Song J.L., Sun X.W., Deng W.Q., Jiang C.Y., Lei W., Huang J.H., Liu R.S. An oleic acid-capped CdSe quantum-dot sensitized solar cell. *Appl. Phys. Lett.*, 2009, **94**, P. 153115. doi: 10.1063/1.3117221.

[17] Mlowe S., Pullabhotla V.S.R., Mubofu E.B., Ngassapa F.N., Revaprasadu N. Low temperature synthesis of anacardic acid capped cadmium chalcogenide nanoparticles. *Int. Nano. Lett.*, 2014, **4**, P. 106.

[18] Mlowe S., Pullabhotla V.S.R., Mubofu E.B., Ngassapa F.N., Nejo A.A., O'Brien P., Revaprasadu N. Lead chalcogenides stabilized by anacardic acid. *Mater. Sci. Semicond. Process.*, 2013, **16**, P. 263–268.

[19] Tyman J.H.P. Long-chain phenols. V. Gas chromatographic analysis of cashew nut-shell liquid. (Anacardium occidentale). *J. Chromatog*, 1975, **111**, P. 285–292.

[20] Paramashivappa R., Kumar P.P., Vithayathil P.J., Rao A.S. Novel method for isolation of major phenolic constituents from cashew (Anacardium occidentale L) Nut Shell Liquid. *J. Agric. Food Chem.*, 2001, **49**, P. 2548–2551.

[21] Lucio P.L.L., Santos C.O., Romeiro L.A.S., Costa A.M., Ferreira J.R.O., Cavalcanti B.C., Moraes O.M., Costa-Lotufo L.V., Pessoa C., Santos M.L. Synthesis and cytotoxicity screening of substituted isobenzofuranones designed from Anacardic acids. *Eur. J. Med. Chem.*, 2010, **45**, P. 3480–3489.

[22] Mokari T., Zhang M., Yang P. Shape, size, and assembly control of PbTe nanocrystals. *J. Am. Chem. Soc.*, 2007, **129**, P. 9864–9865.

NANOSYSTEMS: PHYSICS, CHEMISTRY, MATHEMATICS, 2016, 7 (4), P. 728–731

Investigation on the preparation and properties of nanostructured cerium oxide

G. Jayakumar, A. Albert Irudayaraj*, A. Dhayal Raj, M. Anusuya

PG & Research Department of Physics, Sacred Heart College, Tirupattur, Vellore District,
Tamil Nadu, India

*gjayaphysics@gmail.com

PACS 61.46.-w **DOI 10.17586/2220-8054-2016-7-4-728-731**

Cerium oxide (CeO_2) nanoparticles were successfully synthesized by the hydrothermal method with different reaction times. The synthesized CeO_2 nanoparticles were characterized by Powder X-Ray diffraction (XRD), Scanning Electron Microscopy (SEM), UV-Vis spectroscopy and FTIR spectroscopy. The effects of the reaction time on the structure and morphology of the prepared samples were investigated using XRD and SEM. The XRD studies reveal that the ceria nanoparticles have face-centered cubic structure. The SEM images reveal that the prepared Ceria nanoparticles are an aggregated form of spherical nanoparticles and the particle size decreases with increasing reaction time. FTIR analysis confirms the presence of CeO_2 in the prepared samples. UV-Vis spectral studies show that the UV cut off wavelength decreases and the optical band gap increases with increased reaction time. Photoluminescence (PL) studies indicate that the PL emission of both the samples occurs at 683 nm, however, the emission intensity increases with longer reaction times.

Keywords: ceria nanoparticles, hydrothermal method, photoluminescence.

Received: 8 February 2016

Revised: 10 May 2016

1. Introduction

Cerium oxide (CeO_2) is a refractory material possessing cubic fluorite crystal structure [1,2]. It is one of the most reactive rare earth metal oxides due to its oxygen storage capacity (OSC), oxygen deficiency, and electronic conductivity. It has promising applications in fuel cells, oxygen sensors and mechanical polishing. It also has utility as an ultraviolet blocking agent, luminescent material and photocatalyst. Ceria nanoparticles can be prepared by methods such as hydrothermal [3], reverse micelles, micro-emulsion [4], homogeneous precipitation [5] etc. The main objective of this research paper is studying the effect of reaction time on the structural and optical properties of nanostructured cerium oxide prepared by the hydrothermal method.

2. Experimental

2.1. Synthesis

All the reagents used in the synthesis process were of analytical grade purity and used without any further purification. In the synthesis process, 0.274 g of ammonium ceric nitrate ($(NH_4)_2Ce(NO_3)_6$) was dissolved in 5 ml distilled water and 0.499 g of Sodium hydroxide (NaOH) was dissolved in 25 ml distilled water. These two solutions were mixed and the mixture was stirred for 30 min. To the resultant precursor solution obtained, 0.1808 g of urea ($CO(NH_2)_2$) dissolved in 10 ml of distilled water, was added. The solution was transferred to a Teflon-lined autoclave which was maintained at 200°C for 24 hours. The autoclave was allowed to cool down naturally and to reach the room temperature. The final product was collected from the autoclave and washed several times with distilled water and ethanol. The product was dried at 80°C for 6 hours. The dried sample was calcined at 400°C for 2 hrs.

$$CO(NH_2)_2 + 3H_2O \rightarrow 2NH_4^+ + 2OH^- + CO_2\uparrow$$

$$NH_4^+ + OH^- \leftrightarrow NH_3\cdot H_2O \leftrightarrow H_2O + NH_3\uparrow$$

$$(NH_4)_2Ce(NO_3)_6 + 4NaOH \xrightarrow{200^\circ C} Ce(OH)_4 + 4NaNO_3 + 2NH_3\uparrow + 2NO_3 + H_2\uparrow$$

$$Ce(OH)_4\cdot xH_2O \xrightarrow{80^\circ C} Ce(OH)_4 + xH_2O\uparrow$$

$$Ce(OH)_4 \xrightarrow{400^\circ C} CeO_2 + 2H_2O\uparrow$$

2.2. Characterizations

The XRD measurements were carried out using Rigaku X-ray diffractometer with CuKα (λ = 1.54187 Å) radiation in the range of 10 – 80 ° at room temperature. The surface morphology of the particles was studied by scanning electron microscope.The optical transmittances of the samples were studied by Varian Cary 50 UV-Visible spectrophotometer in the range 200 – 800 nm. The FTIR spectra were recorded in the range of 400 – 4000 cm^{-1} by PERKIN ELMER SPECTRUM II FTIR spectrometer. The photoluminescence spectra were obtained by PERKIN ELMER LS45 fluorescence spectrophotometer using excitation wavelength of 343 nm.

3. Results and discussions

3.1. XRD analysis

The powder XRD patterns of CeO_2 nanoparticles prepared with different reaction times are shown in Fig. 1. The peaks are indexed using JCPDS card #34-0394. Both 12 hour and 24 hour CeO_2 samples have Face Centered Cubic structure with lattice parameters $a = b = c = 5.411$ Å and $\alpha = \beta = \gamma = 90$ °. The diffraction peaks found at 28.27, 33.09, 47.34, 53.36, 69.26 and 76.75 ° showed a broadening effect, which suggests the formation of nanosized CeO_2. The absence of impurities indicates that pure CeO_2 is synthesized by the hydrothermal method. The average crystallite sizes (D) of the CeO_2 nanoparticles prepared with different reaction times, were calculated using the Debye-Scherrer equation:

$$D = \frac{K\lambda}{\beta \cos\theta},$$

where λ is the wavelength of the CuKα radiation, D is the crystallite size, K is a constant and its value is taken as 0.9, θ is the diffraction angle and β is the full-width half maximum (FWHM). The average crystallite size decreased slightly from 3.9 nm to 3.6 nm as the reaction time increased from 12 to 24 hours. The decrease of crystallite size with increasing reaction time was also confirmed from SEM images.

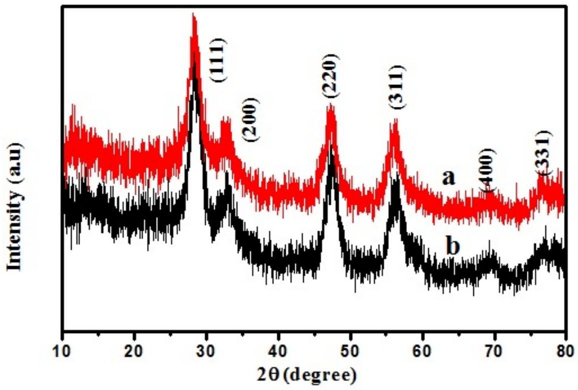

FIG. 1. XRD spectra of the CeO_2 nanoparticles prepared at (a) 24 hours and (b) 12 hours

3.2. FTIR spectra

The FTIR spectra of CeO_2 nanoparticles prepared by hydrothermal method with different reaction times are shown in Fig. 2. The band below 700 cm^{-1} is due to the Ce–O stretching vibrations [6–8].

3.3. UV-Visible spectra

The optical properties of synthesized CeO_2 were examined by UV-Visible spectrophotometer and the results are depicted in Fig. 3. The UV cutoff wavelength of the 12 hour sample was 349 nm, while the UV cutoff wavelength of the 24 hour sample was 343 nm. Additionally, the UV-Visible spectra showed no other peak related with impurities and structural defects, which confirmed that the synthesized nanoparticles are pure CeO_2. The band gap energy of 12 hour sample was 3.54 eV, whereas the band gap energy for the 24 hour sample was found to be 3.67 eV. As the reaction time increased, the band gap energy increased while the crystallite size decreased.

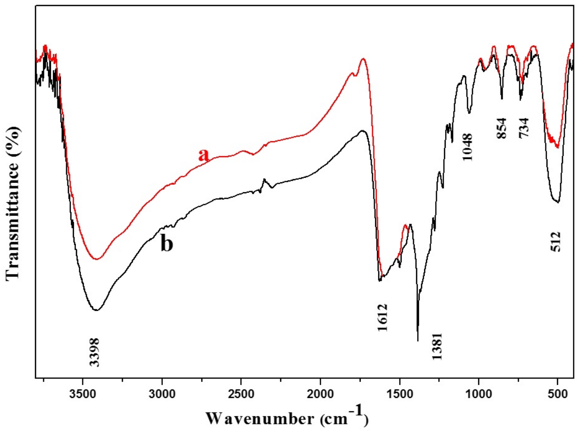

FIG. 2. FTIR spectra of the CeO_2 nanoparticles prepared at (a) 24 hours and (b) 12 hours

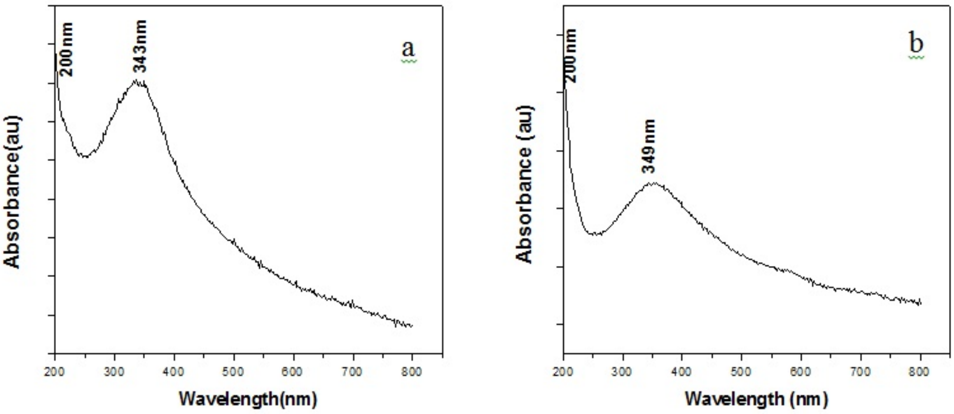

FIG. 3. UV-Vis spectra of the CeO_2 nanoparticles prepared at (a) 24 hours and (b) 12 hours

3.4. Scanning electron microscopy

The SEM images of the CeO_2 nanoparticles prepared by hydrothermal method with different reaction times are shown in Fig. 4. The CeO_2 nanoparticles prepared with 12 hours reaction time had sphere-like structure with an average particle size of 78 nm. The CeO_2 nanoparticles prepared with 24 hours reaction time also had sphere-like structure with an average particle size of 63 nm. Hence, it may be said that the change in the reaction time does not lead to any change in the shape of the CeO_2 nanoparticles, however, the change in the reaction time definitely had an effect on the particle size. The particle size decreased with additional reaction time.

3.5. Photoluminescence studies

The PL spectra of the CeO_2 nanoparticles prepared with different reaction time are shown in Fig. 5. The samples were excited by 343 nm wavelength, and the emission wavelength of these samples was obtained at approximately 683 nm. This emission peak corresponds to red-light. The emission intensity increased from 110.8 a.u to 132.6 a.u with longer reaction times.

4. Conclusions

CeO_2 nanoparticles were successfully synthesized by hydrothermal method and were analyzed by XRD, FTIR, SEM, UV-Visible spectroscopy and photoluminescence measurements. The studies indicate that the reaction time has an effect on the particle size and hence on the optical properties of CeO_2 nanoparticles. The CeO_2 nanoparticles prepared at 24 hours exhibited smaller particle size. The XRD studies revealed that they have face centered cubic structure and have the average grain size of 3.6 nm. From the SEM studies, the average particle size of CeO_2 nanoparticles prepared at 24 hours was found to be 63 nm. The UV-visible spectroscopic studies and PL studies

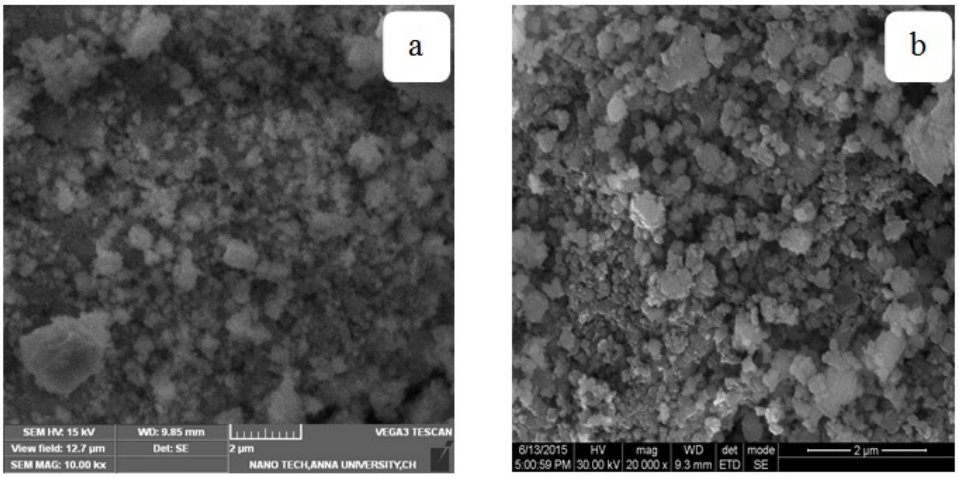

FIG. 4. SEM images of the CeO_2 nanoparticles prepared at (a) 24 hours and (b) 12 hours

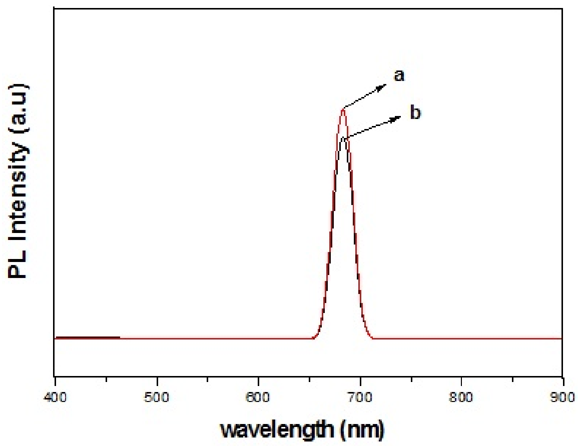

FIG. 5. PL spectra of CeO_2 nanoparticles prepared at (a) 24 hours and (b) 12 hours

reveal that the CeO_2 nanoparticles prepared at 24 hours have a lower UV cut off wavelength, wider optical transmission range and higher PL emission intensity; i.e. it has better optical properties.

References

[1] Kang H.S., Kang Y.C., Koo H.Y., Ju S.H., Kim D.Y., Hong S.K., Sohn J.R., Jung K.Y., Park S.B. Nano-sized ceria particles prepared by spray pyrolysis using polymeric precursor solution. *Journal of Materials Science and Engineering B*, 2006, **127**, P. 99–104.

[2] Jayakumar G., Albert Irudayaraj A., Dhayal Raj A., Magimai Antoni Raj D., Daniel Lawrence D. Comparative studies on Cerium Phosphate and Cerium Oxide Nanoparticles. *Journal of Chem. Tech Research*, 2015, **7**(3), P. 1385–1391.

[3] Masui T., Fujiwara K., Machida K., Adachi G. Characterization of cerium (IV) oxide ultrafine particles prepared by reversed micelles. *Journal of Chem. Mater.*, 1997, **9**, P. 2197–2204.

[4] Chen H., Chang H. Homogeneous precipitation of cerium dioxide nanoparticles in alcohol/water mixed solvents. *Colloids and Surfaces A: Physicochem. Eng. Aspects*, 2004, **242**, P. 61–69.

[5] Khan S.B., Faisal, Mohammed Rahman M., Jamal A. Exploration of CeO_2 nanoparticles as a chemi-sensor and photo-catalyst for environmental applications. *Science of the total Environment*, 2011, **409**, P. 2987–2992.

[6] Wang G., Mu Q., Chen T., Wang Y. Synthesis, characterization and photoluminescence of CeO_2 nanoparticles by a facile method at room temperature. *Journal of Alloys and Compounds*, 2010, **493**, P. 202–207.

[7] Bo Liu, Bingbing Liu, Li, Zepeng Li Q, Ran Liu, Xu Zou, Wei Wu, Wen Cui, Zhao dong Liu, Dongmei Li, Bo Zou, Tian Cui, Guangtian Zou. Solvothermal synthesis of monodisperse self-assembly CeO_2 nanospheres and their enhanced blue-shifting in ultraviolet absorption. *Journal of Alloys and Compounds*, 2010, **503**, P. 519–524

[8] Kumar E., Selvarajan P., Muthuraj D. Synthesis and characterization of CeO_2 nanocrystals by solvothermal route. *Journal of Materials Research*, 2013, **16**, P. 269–276.

NANOSYSTEMS: PHYSICS, CHEMISTRY, MATHEMATICS, 2016, 7 (4), P. 732–739

Polyaniline-Titanium dioxide composite as humidity sensor at room temperature

S. Kotresh[1], Y. T. Ravikiran[1,*], H. G. Raj Prakash[2], S. C. Vijaya Kumari[3]

[1]Department of PG Studies and Research in Physics, Government Science College, Chitradurga 577501, India

[2]Department of Physics, JNN College of Engineering, Shivamogga 577204, India

[3]Department of Physics, SJM College of Arts, Science and Commerce, Chitradurga 577501, India

*ytrcta@gmail.com

PACS 81.07.Pr **DOI 10.17586/2220-8054-2016-7-4-732-739**

In the present work, Polyaniline (PANI) and Polyaniline-Titanium dioxide (PANI-TiO_2) composite have been synthesized separately by chemical polymerization of aniline without/with TiO_2. Characteristic absorption bands of PANI and TiO_2 in the composite were confirmed by FT-IR studies, indicating the interaction of PANI with TiO_2. Comparative study of XRD patterns of PANI and the composite confirmed superficial deposition of PANI on TiO_2 and the average size of the composite particle was found to be 25 nm. The aggregated granular porous morphology of the composite was confirmed by its SEM image. The composite's sensing response to humidity at room temperature was tested and was found to be 84.21 % in the range 25 % – 95 % RH. The response and recovery time of the composite at 95 % RH were measured to be 60s and 100s respectively and its sensing stability over a period of one month was also confirmed.

Keywords: polyaniline composites, humidity sensor, sensitivity, stability.

Received: 9 February 2016

Revised: 26 April 2016

1. Introduction

In recent years, nanocomposites have evolved as the most sought after materials in various fields such as sensors, super capacitors, catalysis, light emitting diodes and fuel cells because they offer flexibility in terms of tuning their electrical and mechanical properties for best synergetic effects [1–5]. Thus, reliable fabrication of devices using these materials by cost effective methods is a major concern of many researchers. One such method is the incorporation of metal/metal oxides into the conducting polymers via a chemical or electrochemical route [6–12].

With the advancement of moisture-sensitive technologies and the increasing awareness for quality of life issues, humidity sensing has gained in importance in various areas like medicine, agriculture and electronic industries [13]. With the rapid advances in technology, increasing efficiency, reducing cost, reliability and miniaturization for fabrication of sensors are the major concerns in any research. In recent years, conducting polymer based sensors have become more favorable over metal oxide based sensors in terms of increased sensitivity, simple processing and their room temperature operation [14]. Among all conducting polymers, PANI is the most preferred because of its unique characteristics, such as tunable electrical and chemical properties, easy processing and low costs [15]. Recently, PANI based metal oxide composites have been found to be more advantageous in terms of enhanced humidity sensitivity and such composites have been studied by many researchers. Electrospun PANI composite nanofibers have shown good sensitivity to humidity with a good recovery and response time as reported by Q. Lin *et al.* [16]. M.T.S. Chani *et al.* Studied the humidity sensitivity of an orange dye PANI composite film by impedance measurements and have showed a uniform change in impedance for humidity values ranging from 30 – 90 % RH [17]. Room temperature humidity sensing of PANI-PVA composite has been studied by Y. Li and others, and they showed that the sensitivity of the composite increases with increased impedance from 10 – 90 % RH and has both quick response and recovery times [18]. K. C. Sajjan et al. have reported better humidity sensing response for a PANI-Cr_2O_3 composite over the range 20 – 95 % RH [19]. S.C. Nagaraju et al. have reported good humidity sensing response for PANI-Pr_2O_3 composites in the range 10 – 90 % RH [20]. In this work, we have attempted to fabricate a low cost humidity sensing device made of PANI-TiO_2 composite which can be easily prepared and operable at room temperature. We preferred TiO_2 with PANI for the composite because it is a white n-type transition metal oxide semiconductor with a wide band gap (3.0 – 3.2 eV) and has a large dielectric constant ($\sim$100) [21,22]. This compound's compatible physical properties were considered favorable for use in fiber optics, photovoltaics, gas sensors, biocompatible materials, electrolytic capacitors and dye sensitized solar cells [21].

In this work, PANI and PANI-TiO_2 composite were synthesized by a cost effective, simple in situ chemical polymerization method and were structurally characterized using FTIR, XRD and SEM techniques. Based on these studies, humidity sensitivity of the composite's film prepared by spin coating technique was tested and analyzed. Its stability, recovery and response time have also been studied. Both processability and sensing studies were carried out at room temperature.

2. Experimental

2.1. Materials

Aniline ($C_6H_5NH_2$) (99.5 %), ammonium persulfate [$(NH_4)_2S_2O_8$] (98 %), hydrochloric acid (HCl) (34.5%) and titanium dioxide (TiO_2) (99.5 %), all of analytical grade reagents were purchased from s.d. Fine Chemicals, Mumbai, India. Aniline monomer was doubly distilled before use.

2.2. Preparation of PANI-TiO_2 composite

The method of preparation of pure PANI and the PANI-TiO_2 composite at room temperature is as follows; firstly, a solution of 6.7 ml of aniline monomer in 60 ml 1M HCl was prepared. It was added to 180 ml of deionized water in which 0.67 g of TiO_2 powder was previously dispersed. Then adsorption of aniline on TiO_2 was facilitated by sonication of the above mixture. Then 7.5 g of $(NH_4)_2S_2O_8$ in 60 ml deionized water was added dropwise into the above mixture with continuous stirring for 30 min and then allowed to polymerize for 8 – 10 hrs. The reaction product was collected by centrifugation and washed successively with deionized water and acetone until a clear precipitate was obtained which was dried in vacuum until it turned dark green.

2.3. Characterization of the samples

The FTIR spectra of pristine PANI, PANI-TiO_2 composite and TiO_2 were recorded using Nicolet 750 FT-IR spectrometer in KBr medium at room temperature. The X-ray diffraction pattern of each sample was obtained by employing Siemens D-5000 powder X-Ray diffractometer with CuKα source radiation of wavelength 1.54×10^{-10} m. SEM images of PANI and the composite samples were recorded using a Hitachi S-520 scanning electron microscope.

2.4. Humidity sensing measurements

The experimental set up used for humidity sensing measurements has been described previously in our literature [23]. A film of the composite was prepared by dissolving the composite powder in m-cresol and then coating it on a glass plate using spin coating unit (Make: Delta Scientific Pvt. Ltd, India, Model: Delta Spin I). Then, interdigitated silver electrodes were printed on it and it was then placed in a specially designed glass chamber well equipped for maintaining required relative humidity. The chamber was tightly closed at the top with a cork. One end of these electrodes were connected to the film by passing through the cork while the other ends were connected to a digital LCR meter (Make: Hioki, Japan, Model: 3532-50) which recorded the impedance changes before and after exposing the sample to humidity at a selected frequency of 100 Hz. The relative humidity in the chamber was varied using saturated salt solutions and monitored using humidity meter (Mextech-DT-615).

3. Results and discussion

3.1. Fourier transform infrared spectroscopy

FT-IR analysis was used to examine the composite structure after polymerization. The FT-IR spectra of TiO_2, PANI and PANI-TiO_2 composite are shown in Fig. 1.

The FT-IR spectrum of pure TiO_2(Fig. 1(c)) shows strong absorption bands at 648 cm^{-1} and 419 cm^{-1} which are the characteristic vibrations of TiO_2. These are respectively assigned to the Ti-O-Ti stretching vibration and for Ti-O and Ti-O-Ti combined stretching vibrations and all these results agreed with the published literature [24].

In the FT-IR spectrum of pristine PANI (Fig. 1(b)), the absorption bands at 3419 cm^{-1}, 1600 cm^{-1}, 1498 cm^{-1}, 1299 cm^{-1}, 1147 cm^{-1} and 880 cm^{-1} are attributed to the PANI chain. These are respectively assigned to O-H stretching of absorbed water, the C=C stretching of quinoid ring, the C=C stretching of benzenoid ring, the C-N stretching of imine and secondary amine of PANI backbone, the C-H stretching in-plane bending vibration and the 1,4 coupling of aromatic ring and all these have agreed well with the pattern published in the literature [25,26].

The FT-IR spectrum of the composite sample (Fig. 1(a)), exhibited characteristic absorption bands at 3425 cm^{-1}, 1630 cm^{-1}, 1497 cm^{-1}, 1299 cm^{-1}, 1136 cm^{-1}, 896 cm^{-1}, 611 cm^{-1} and 419 cm^{-1}, which are associated with the characteristic vibrations of both PANI and TiO_2 but with a small shift are due to the interaction of oxygen ions of TiO_2 and nitrogen atoms of PANI macromolecules present in the composite [27].

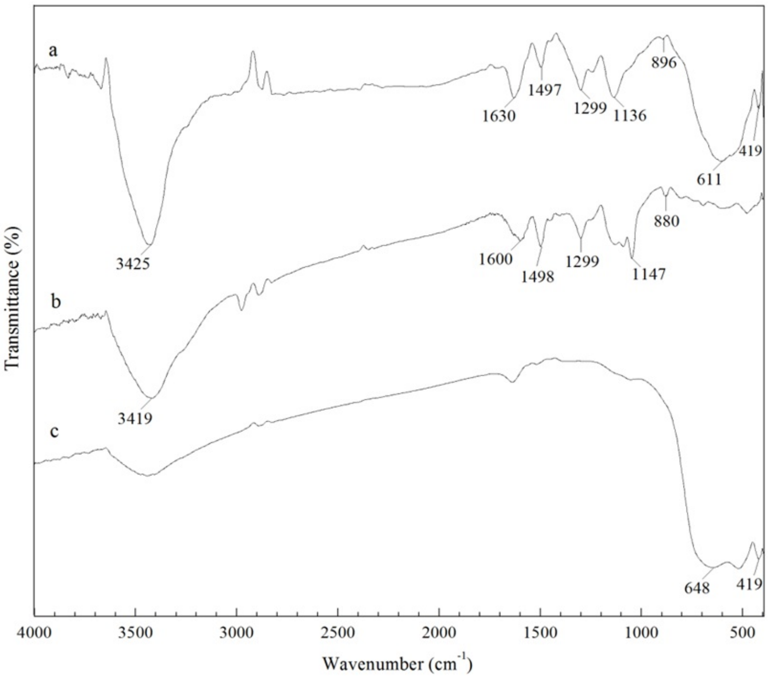

FIG. 1. Fourier transform infrared spectra of (a) PANI-TiO$_2$ composite (b) Pristine PANI and (c) TiO$_2$

3.2. X-ray diffraction

The XRD patterns of PANI, PANI-TiO$_2$ composite and that of TiO$_2$ with assigned *hkl* values are shown in Fig. 2. The XRD pattern of pristine PANI (Fig. 2(a)), reveals some degree of crystallinity with the appearance of broad peaks corresponding to (100) and (110) planes [JCPDS No. 53-1718] in the region 2θ = 15 – 25 ° similar to those reported in our earlier literature [**?**, 28] The XRD pattern of TiO$_2$ (Fig. 2(c)) clearly shows peaks corresponding to the planes (110) (101) (200) (111) (210) (211) (220) (002) (310) and (112) in the range 2θ = 20 – 70 ° and the peaks when compared with JCPDS No. 870710 were confirmed to be of rutile TiO$_2$. The same pattern for TiO$_2$ has also been confirmed in previous literatures [29, 30].

Comparison of XRD patterns of PANI, TiO$_2$ and the PANI-TiO$_2$ composite (Fig. 2(b)) indicates predominance of TiO$_2$ in the composite, the rutile phase (110) of TiO$_2$ has remained while the broad weak peaks of PANI have disappeared. All these suggest that there is interaction between PANI and TiO$_2$ and that TiO$_2$ has restricted the growth of PANI chains hampering its crystalline behavior. So it can be concluded that PANI has just deposited on TiO$_2$ and has no effect on the crystalline behavior of TiO$_2$. Similar study has been reported in earlier literature [30].

Applying the Scherrer formula [31] using Eq. (1) to the most prominent sharp peak at 28 °, we obtained the size of the crystallite t to be 25 nm:

$$t = \frac{k\lambda}{b\cos\theta}, \tag{1}$$

where b is the breadth in radians, θ is the Bragg angle and λ is the wavelength of radiation. The coefficient k normally takes a value close to 0.9.

3.3. Scanning electron microscopy

The morphology of TiO$_2$, PANI and PANI-TiO$_2$ composite are shown in Fig. 3. The morphology of pristine PANI shown in Fig. 3(a) is an agglomerated granular structure with uniform surface. The morphology of the composite (Fig. 3(b)) shows predominance of TiO$_2$ particles, their surface being covered by PANI, which agrees very well with the results obtained by XRD studies.

The Scanning electron micrograph of TiO$_2$ shown in Fig. 3(c) reveals aggregated granular morphology and agrees well with the SEM images in previously reported studies [32].

The average grain size D_{Avr} of the composite material calculated using Mendelson's formula [33] given by Eq. (2) is 25 nm:

$$D_{Avr} = \frac{1.56 \times C_L}{M' N_i}, \tag{2}$$

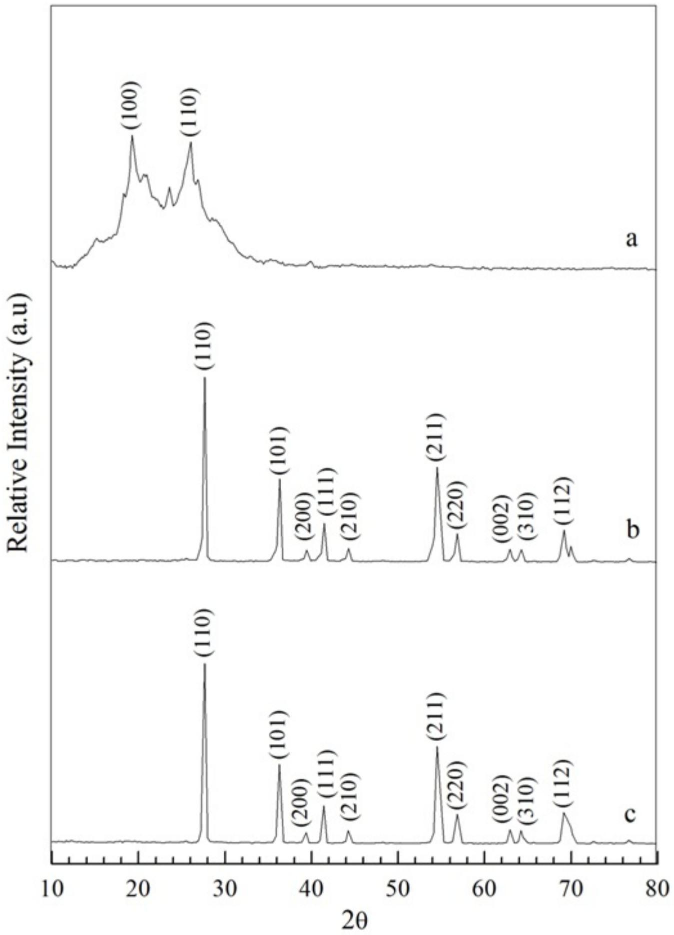

FIG. 2. X-ray diffraction spectra of (a) Pristine PANI (b) PANI-TiO_2 composite and (c) TiO_2

where C_L is the total length of the test line used, N_i is the number of intercepts and M' is the magnification of the photograph.

3.4. Humidity sensing response studies

The sensing response of the composite for various % RH are measured at 100 Hz using fractional base line manipulation method [34] using Eq. (3):

$$S_H = \frac{Z_0 - Z_{RH}}{Z_0} \times 100 \tag{3}$$

where Z_0 is the impedance of the sample before exposure to moisture (dry air with 25 % RH) and Z_{RH} is the impedance at various % RH.

The sensing response characteristic curve of the composite thus obtained by the above method is shown in Fig. 4. It can be seen that the composite is sensitive and its response is linear in the 25 – 95 % RH range with a maximum sensing response of 84.21 %. This linear response of the composite in this range with increasing humidity may be attributed to the following probabilities: (i) At low RH mobility of TiO_2 ions in the composite is restricted due to curling up of polymer chains. As humidity increases, polymer chain uncurls and becomes aligned by absorbing water molecules paving way for faster hopping of charge carriers, resulting in increased sensing response of the composite [21,35]. (ii) Porosity of the polymers as revealed by SEM studies may facilitate absorption of water molecules as RH increases causing a decrease in the impedance of the composite [13].

Efficiency of the composite as a sensing device was studied by measuring its response and recovery times [36]. Humidity sensing response and recovery characteristic curve of the composite at 100 Hz is shown in Fig. 5. For the purposes of our study, two chambers, one with 25 % RH and another with 95 % RH were maintained separately. The response time of 60 s was recorded when the sample was moved from 25 % RH to 95 % RH and a recovery

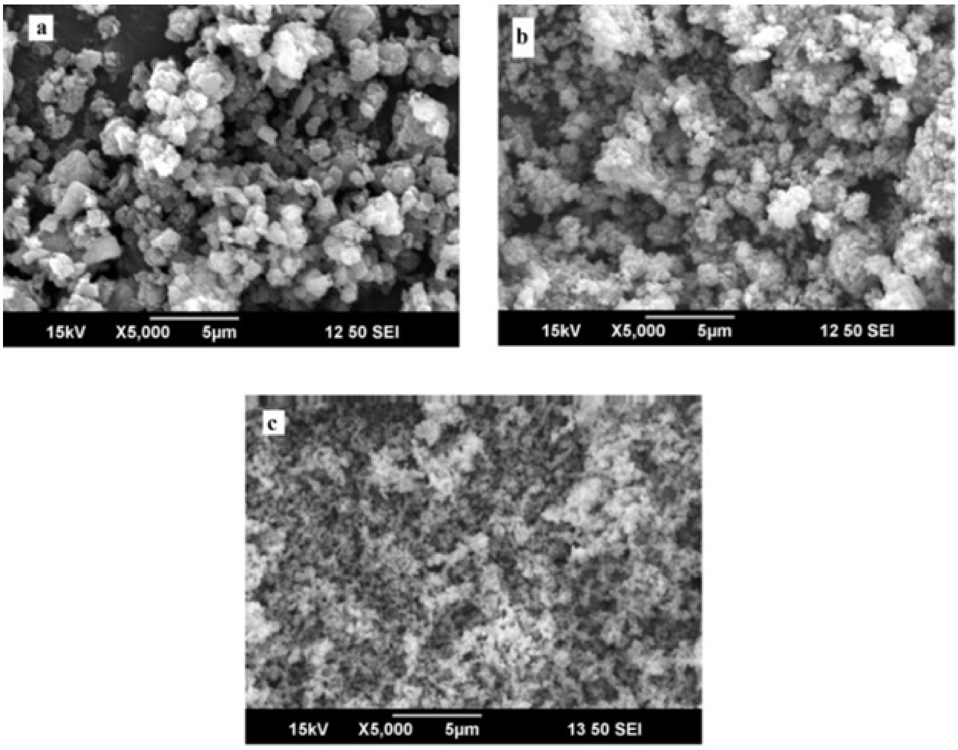

FIG. 3. Scanning electron micrographs of (a) Pristine PANI (b) PANI-TiO_2 composite and (c) TiO_2

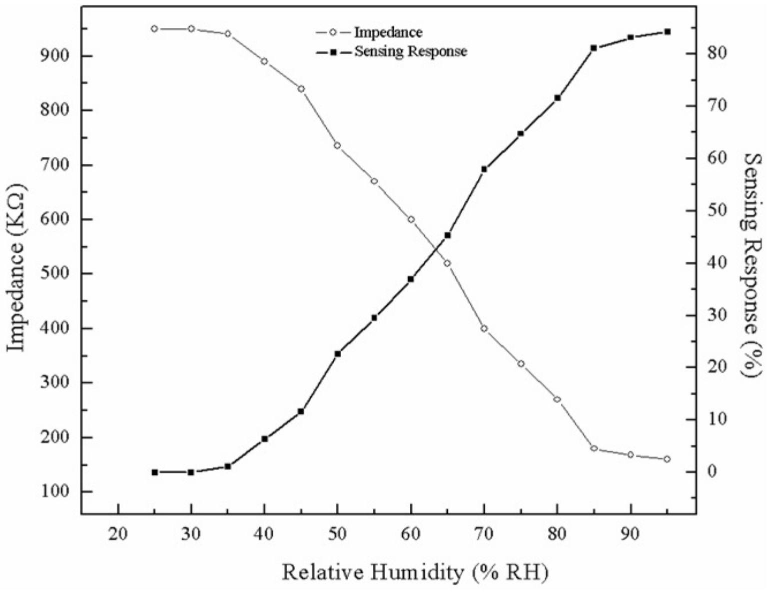

FIG. 4. Variation of sensing response and Impedance with relative humidity at 100 Hz

time of 100 s was recorded when the sample was moved from 95 % RH to 25 % RH, switching time being 1s in both the cases, establishing that the composite can become a good humidity sensing device.

To examine the practical viability of the composite for use as a sensor, variation of sensing response at 55 % RH and at 95 % RH at a frequency of 100 Hz after every one week for one month was studied [37]. The results presented in the graph shown in Fig. 6 suggest stable sensing ability both during adsorption and desorption with a negligible degradation of 3 % in sensing response. This finding suggests that the composite, apart from being a good sensor, is also stable and so it can be practically feasible to utilize it in a sensor device.

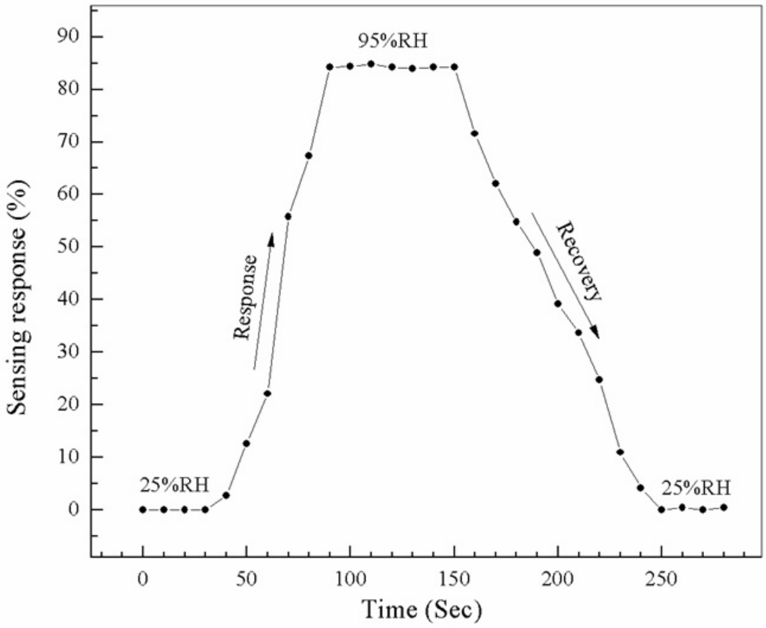

FIG. 5. Response and recovery characteristic curves of PANI-TiO_2 composite at 100 Hz

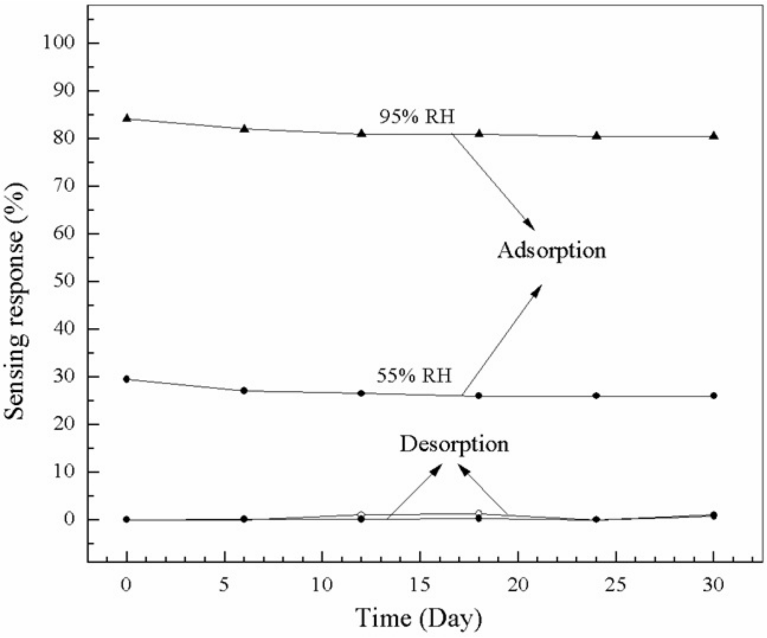

FIG. 6. Stability of PANI-TiO_2 composite at 100 Hz

4. Conclusions

The PANI-TiO_2 composite synthesized by simple chemical polymerization method showed a room temperature sensing response of 84.21 % in the range 25 % – 95 % RH. The sensing response of the composite film prepared by cost effective spin coating method was measured using LCR meter at a selected frequency of 100 Hz. The efficiency of the composite as a sensor was also confirmed with a recorded response time of 60s and a recovery time of 100s. The composite has shown stable sensing ability over a period of one month. All these results show that the composite has the potential to become an efficient humidity sensing device operable at room temperature besides being easily prepared and cost effective.

Acknowledgement

The author is thankful to the University Grants Commission, New Delhi, for their financial support provided under major research project (41-917/2012 (SR) dated: 23/07/2012), to carry out this work. The Author wishes to acknowledge SAIF, Cochin, for providing facility for characterization of the samples. The author is also thankful to Commissioner, Department of Collegiate Education, Government of Karnataka and Principal Prof. C.M. Vivekananda, Government Science College, Chitradurga for their encouragement and support to carry out this research work.

References

[1] Tang W., Peng L., Yuan C., Wang J., Mo S., Zhao C., Yu Y., Min Y., Epstein A.J. Facile synthesis of 3D reduced grapheme oxide and its Polyaniline nanocomposites for super capacitor application. *Synth. Met.*, 2015, **202**, P. 140–146.

[2] Bahloul A., Nessark B., Briot E., Groult H., Mauger A., Zaghib K., Julien C.M. Polypyrrole-covered MnO_2 as electrode material for supercapacitor. *J. Power Sources.*, 2013, **240**, P. 267–272.

[3] Rajesh., Ahuja T., Kumar D. Recent progress in the development of nano-structured conducting polymers/nanocomposites for sensor applications. *Sens. Actuators B.*, 2009, **136**, P. 275–286.

[4] Memjoglu F., Bayrakceken A., Tuba Oznuluer T., Metin A.K. Synthesis and characterization of polypyrrole/carbon nanocomposite as a catalyst support for fuel cell applications. *Int. J. Hydrogen Energy.*, 2012, **37**, P. 16673–16679.

[5] Shin S., Kim S., Kim Y. H., Kim S. Enhanced performance of organic light-emitting diodes by using hybrid anodes composed of polyaniline and conducting polymer. *Curr. Appl. Phys.*, 2013, **13**, P. S144–S147.

[6] Ali Y., Vijay K., Sonkawade R.G., Shirsat M.D., Dhaliwal A.S. Two-step electrochemical synthesis of Au nanoparticles decorated Polyaniline nanofiber. *Vacuum*, 2013, **93**, P. 79–83.

[7] Ali Y., Kashma S., Kumar V., Sonkawade R.G., Dhaliwal A.S. Polypyrrole microspheroidals decorated with Ag nanostructure: Synthesis and their characterization. *Appl. Surf. Sci.*, 2013, **280**, P. 950–956.

[8] Ali Y., Vijay K., Sonkawade R.G., Dhaliwal A.S. Effect of swift heavy ion beam irradiation on Au–Polyaniline nanocomposite films. *Vacuum*, 2013, **90**, P. 59–64.

[9] Kadam S.B., Datta K., Ghosh P., Kadam A.B., Khirade P.W., Kumar V., Sonkawade R.G., Gambhire A.B., Lande M.K., Shirsat M.D. Improvement of ammonia sensing properties of poly(pyrrole)–poly (n-methylpyrrole) nanocomposite by ion irradiation. *Appl. Phys.*, A 2013, **100**, P. 1083–1088.

[10] Ghoreishi K.B.,Yarmo M.A., Nordin N.M., Samsudin M.W. Enhanced catalyst activity of WO_3 using polypyrrole as support for acidic esterification of Glycerol with Acetic Acid. *J. Chem.*, 2013, article ID 264832, P. 1–10.

[11] Lee S.B., Lee S.M., Lee S., Chung D.W. Preparation and characterization of conducting polymer nanocomposite with partially reduced grapheme oxide. *Synth. Met.*, 2015, **201**, P. 61–66.

[12] Kanwal F., Siddiqi S.A., Batool A., Imran M., Mushtaq W., Jamil T. Synthesis of polypyrrole–ferric oxide (Ppy–Fe_2O_3) nanocomposites and study of their structural and conducting properties. *Synth. Met.*, 2011, **161**, P. 335–339.

[13] Ramaprasad A.T., Rao V. Chitin-polyaniline blend as humidity sensor. *Sens. Actuat. B*, 2010, **148**, P. 117–125.

[14] Zeng F.W., Liu X., Diamond D., Lau K.T. Humidity sensors based on Polyaniline nanofibres. *Sens. Actuat. B*, 2010, **143**, P. 530–534.

[15] MaDiarmid A.G. Semiconducting and metallic polymers: The fourth generation of polymeric materials. *Synth. Met.*, 2002, **125**, P. 11–22.

[16] Lin Q., Li Y., Yang M. Highly sensitive and ultrafast response surface acoustic wave humidity sensor based on electrospunpolyaniline/poly (vinyl butyral) nanofibres. *Anal. Chim. Acta.*, 2012, **748**, P. 73–80.

[17] Chani M.T.S., Karimov K.S., Khalid F.A., Abbas S.Z., Bhatty M.B. Orange dye polyaniline composite based impedance humidity sensors. *Chin. Phys.*, 2012, **22**, P. 010701.

[18] Li Y., Deng C., Yang M. Novel surface acoustic wave-impedance humidity sensor based on composite of polyaniline and poly (vinyl alcohol) with a capacity of detecting low humidity. *Sens. Actuators, B*, 2012, **143**, P. 7–12.

[19] Sajjan K.C., Roy A.S., Parveen A., Khasim S. Analysis of DC and AC properties of a humidity sensor based on polyaniline-chromium oxide composites. *J Mater Sci: Mater Electron.*, 2014, **25**, P. 1237–1243.

[20] Nagaraju S.C., Aashis S. Roy., Prasanna Kumar J.B., Anilkumar K.R., Ramagopal G. Humidity sensing properties of surface modified Polyaniline metal oxide composites. *J. Eng.*, 2014, 8 pages.

[21] Vlazan P., Ursu D.H., Moisesc C.I., Miron I., Sfirloaga P., Rusu E. Structural and electrical properties of TiO_2/ZnO core-shell nanoparticles synthesized by hydrothermal method. *Mater. Charact.*, 2015, **101**, P. 153–158.

[22] Marinel S., Choi D.H., Heuguet R., Agarval D., Lanagan M. Broadband dielectric characterization of TiO_2 ceramics sintered through microwave and conventional processes. *Ceram. Int.*, 2013, **39**, P. 299–306.

[23] Kotresh S., Ravikiran Y.T., Vijayakumari S.C., Raj Prakash H.G., Thomas S. Polyaniline niobiumpentoxide composite as humidity sensor at room temperature. *Adv. Mater. Lett.*, 2015, **6**, P. 641–645.

[24] Ba-Abbad M.M., Kadhum A.A.H., Abu B.M., Takriff M.S., Sopian K. Synthesis and catalytic activity of TiO_2 nanoparticles for photochemical oxidation of concentrated chlorophenols under direct solar radiation. *Int. J. Electrochem. Sci.*, 2012, **7**, P. 4871–4888.

[25] Quillard S., Louarn G., Lefrant S., MacDiarmid A.G. Vibrational analysis of polyaniline: A comparative study of leucoemeraldine, emeraldine, and pernigraniline bases. *Phys. Rev. B: Condens. Matter.*, 1994, **50**, P. 12496–12508.

[26] Wang P.C., Dan Y., Liu L.H. Effect of thermal treatment on conductometric response of hydrogen gas sensors integrated with HCl-doped Polyaniline nanofibers. *Mater. Chem. Phys.*, 2014, **144**, P. 155–161.

[27] Nasirian S., Moghaddam H.M. Hydrogen gas sensing based on polyaniline/anatase titania nanocomposite. *Int. J. Hydrogen Energ.*, 2014, **89**, P. 630–642.

[28] Ravikiran Y.T., Kotresh S., Vijayakumari S.C., Thomas S. Liquid petroleum gas sensing performance of polyaniline carboxymethyl cellulose composite at room temperature. *Curr. Appl. Phys.*, 2014, **14**, P. 960–964.

[29] Nasirin S., Moghaddam H.M. Effect of different titania phases on the hydrogen gas sensing features of polyaniline/TiO_2 nanocomposite. *Polymer*, 2014, **55**, P. 1866–1874.

[30] Li X., Chen W., Bian C., He J., Xu N., Xue G. Surface modification of TiO_2 nanoparticles by polyaniline. *Appl. Surf. Sci.*, 2003, **217**, P. 16–22.

[31] Patterson A.L. The scherror formula for x-ray particle size determination. *Phys. Rev. B*, 1939, **56**, P. 978–982.

[32] Marija B.R., Milica V.M., Dejan S.M., Edin H.S., Gordana N.C.M., Maja M.R., Zoran V.S. Influence of TiO_2 nanoparticles on formation mechanism of PANI/TiO_2 nanocomposite coating on PET fabric and its structural and electrical properties. *Surf. Coat. Technol.*, 2015, **278**, P. 38–47.

[33] Mendelson M.I. Average grain size in polycrystalline ceramics. *J. Am. Ceram. Soc.*, 1969, **52**, P. 443–446.

[34] Sen T., Shimpi N.G., Mishra S., Sharma R. Polyaniline/γ-Fe_2O_3 nanocomposite for room temperature LPG sensing. *Sens. Actuat. B*, 2014, **190**, P. 120–126.

[35] Lin W.D., Chang H.M., Wu R.J. Applied novel sensing material graphene/Polypyrrole for humidity sensor. *Sens. Actuat. B*, 2013, **181**, P. 326–331.

[36] Qi Q., Zhang T., Wang S., Zheng X. Humidity sensing properties of KCl-doped ZnO nanofibers with super-rapid response and recovery. *Sens. Actuat. B*, 2009, **137**, P. 649–655.

[37] Zhang Y., Zheng X., Zhang T., Gong L., Dai S., Chen Y. Humidity sensing properties of the sensor based on $Bi_{0.5}K_{0.5}TiO_3$ powder. *Sens. Actuat. B*, 2010, **147**, P. 180–184.

NANOSYSTEMS: PHYSICS, CHEMISTRY, MATHEMATICS, 2016, 7 (4), P. 740–746

Zinc oxide-palladium material an efficient solar-light driven photocatalyst for degradation of congo red

Karuppannan Rokesh[1], Kulandaivel Jeganathan[2], Kandasamy Jothivenkatachalam[1,*]

[1]Department of Chemistry, Anna University – BIT Campus, Tiruchirappalli–620024, Tamil Nadu, India

[2]Centre for Nanoscience and Nanotechnology, School of Physics, Bharathidasan University, Tiruchirappalli–620024, Tamil Nadu, India

*jothivenkat@yahoo.com

PACS 81.07.-b **DOI 10.17586/2220-8054-2016-7-4-740-746**

Zinc oxide - palladium nanocomposite material (ZnO-Pd)$_{NCM}$ was prepared and then characterized by UV-Vis spectroscopy, photoluminescence spectroscopy, X-ray diffraction analysis, energy dispersive X-ray analysis and field emission-scanning electron microscopy. The photocatalytic performance of (ZnO-Pd)$_{NCM}$ was investigated by degradation of Congo red under solar light irradiation. Zinc oxide modified with palladium metal could greatly enhance its photocatalytic activity and effectively degraded by Congo red dye.

Keywords: zinc oxide, palladium, nanocomposite, photocatalyst, congo red, degradation.

Received: 11 February 2016

Revised: 23 April 2016

1. Introduction

Dyes from textile industries strongly pollute water resources and produce serious environmental problems. Photocatalysis is an efficient technique to remove the dyes in waste water [1]. Nanostructured semiconductors and their composite materials have been preferred as catalyst (photocatalyst) for the photocatalysis process [2, 3]. Zinc oxide (ZnO) is a wide band gap (3.37 eV) semiconductor material; it is used as one of the efficient photocatalyst and photoelectrocatalyst [4–6]. This compound can be prepared by several techniques with collection of different morphologies and sizes. The nanostructured ZnO and ZnO–metal nanocomposite materials have been found huge attention in the field of photocatalysis [7–9], because of their high surface-volume ratio, stability and surface charge (SPR effect of metal nanoparticles). The metal support with ZnO to increase the photoexcited electrons-hole charge separation, transfer process and decreases the electron-hole recombination rate. Moreover, metal increases the adsorption of pollutant on catalyst surfaces afterwards improved its photocatalytic oxidation and reduction process [10, 11]. Once the ZnO-Pd nanocomposite material was prepared, it was characterized and its photocatalyic activity was investigated by degradation of Congo red dye under solar light.

2. Materials and methods

2.1. Materials

The materials such as zinc acetate dihydrate, palladium acetate, hydrazine hydrate and were obtained from Merck, and sodium borohydride, congo red were purchased from S. D. Chemicals, Mumbai.

2.2. Preparation of ZnO-Pd nanocomposite material

ZnO nanomaterial was prepared by simple microwave assisted technique. A 100 ml mixture of 0.05 M aq. zinc acetate and 0.2 M aq. Hydrazine hydrate was stirred for 30 min then subjected to microwave irradiation 15 min. The obtained white precipitate was washed, centrifuged and calcined at 200 °C for 2 hrs. Then, the prepared ZnO and palladium acetate precursor was added to an aqueous solution with 100:2.5 weight percentage and stirred for few hrs. Then, freshly prepared sodium borohydride solution was added to afford ZnO-Pd nanocomposite material.

2.3. Characterization

The prepared ZnO and (ZnO-Pd)$_{NCM}$ materials absorbance spectra were recorded using a Shimadzu UV-2550 UV-Vis spectrometer. Photoluminescence was recorded using JASCO-FP-6500 spectrofluorometer. The crystalline nature of prepared materials was studied by XRD pattern using a Bruker Advance with Cu Kα radiation. The morphology and elemental composition of the samples were recorded by Carl Zeiss FE-SEM and Bruker EDX instruments.

2.4. Photocatalytic study

The photocatalytic experiment was carried out by photodegradation of Congo red (CR) under solar light irradiation. A 20 mg of prepared ZnO and ZnO-Pd composites material was suspended into 50 ml of Congo red (CR) 25 ppm aq. solution. Then the dye solution was exposed to solar light irradiation in open air condition, time between 11 am to 2 pm with continuous aeration. Subsequently, at a given time interval 3 ml aliquots were collected and centrifuged. The degradation process was monitored and confirmed by UV-Vis absorbance spectroscopy by measuring its absorption.

3. Results and discussion

3.1. Optical property

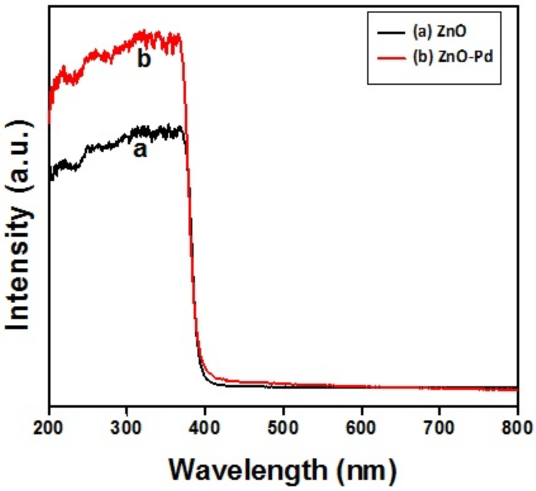

FIG. 1. UV-Diffuse reflectance spectra of (a) ZnO (b) (ZnO-Pd)$_{NCM}$

The UV-DRS measurement reveals that the band energy and optical properties of semiconductors materials. UV-DRS spectra of the ZnO and (ZnO-Pd)$_{NCM}$ samples were measured at room temperature and are shown in Fig. 1. The prepared ZnO and (ZnO-Pd)$_{NCM}$ showed strong absorption below 400 nm in near-UV spectral region, confirming the wide band of ZnO semiconductor material. The (ZnO-Pd)$_{NCM}$ does not show any absorption in the visible region due the particle size and amount of Pd in the composite is much less. Moreover, the (ZnO-Pd)$_{NCM}$ have existed higher absorbance intensity than bare ZnO in UV region, which indicates that the Pd improves the quantum efficiency of the ZnO material [12].

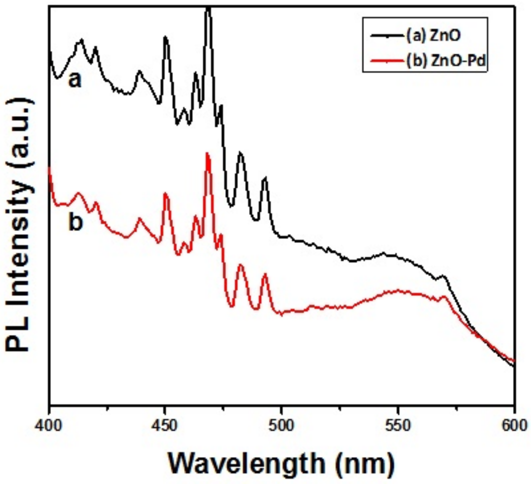

FIG. 2. Photoluminescence spectra (a) ZnO (b) (ZnO-Pd)$_{NCM}$

The PL spectra showed wide band emission at visible region (Fig. 2). This extended emission is due to the recombination of photogenerated electron-hole and oxygen vacancy sites in the materials. The ZnO and (ZnO-Pd)$_{NCM}$ where observed weak emission at 468 nm due to band edge free excitons. The blue and green emission peaks were observed around 520–580 nm for the prepared samples due to presence of oxygen vacancies in the material's surface [13]. The emission intensity of ZnO decreased with the addition of palladium metal because of the Pd trapped excited electrons from the zinc oxide.

3.2. Crystalline properties

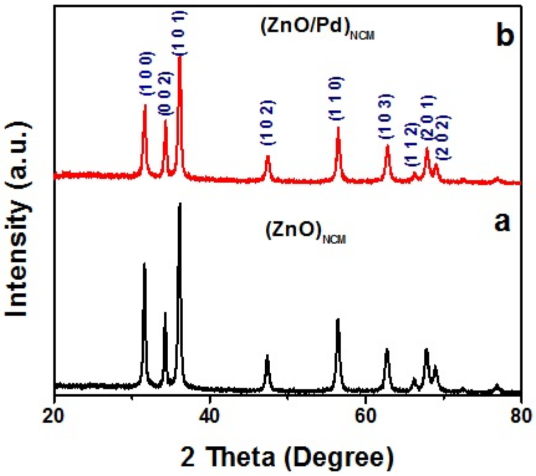

FIG. 3. XRD pattern of (a) ZnO and (b) (ZnO-Pd)$_{NCM}$

The XRD pattern of ZnO and (ZnO-Pd)$_{NCM}$ composite material is shown in Fig. 3. All the diffraction peaks in XRD are confirmed that the prepared ZnO in hexagonal wurtzite structure (JCPDS No. 36-1451). The diffraction peaks of palladium was not observed in (ZnO-Pd)$_{NCM}$ due to the very minimum percentage of Pd present in the composite [13, 14]. The absence of any other peak in XRD is confirmed that the prepared materials are highly pure.

3.3. Morphology and elemental analysis

The morphology and elemental composition of synthesized materials were studied by FE-SEM and EDX analysis is shown in Fig. 4. The synthesized ZnO and ZnO-Pd composite material displays flower buds-like morphology with average size about 1 to 2 μm (Fig. 4(a,c)). The spherical like Pd nanoparticles are deposited on ZnO surface can be confirmed by FE-SEM image. The ZnO buds have exhibited rough surface which formed by the agglomeration of small nanoparticles. EDX analysis provided the elemental composition of the materials is shown in Fig. 4(b,d). In Fig. 4(d) the spectrum confirms that the Zn, O and Pd elements are present in the composite material, as evidence for formation of (ZnO-Pd)$_{NCM}$. The absence of any other elemental peaks in EDX spectrum confirmed that the as-synthesized materials were very pure.

3.4. Photocatalytic study

The photocatalytic experiment was carried out by photodegradation of Congo red (CR) under solar light irradiation. The effect of different parameters such as catalyst loading, solution pH and dye concentration on photodegradation efficiency were evaluated using ZnO and (ZnO-Pd)$_{NCM}$ [15, 16].

The experiment was carried out by 25 ppm (mg/l) of CR in aqueous solution in the presence of 20 mg/50 ml of ZnO and (ZnO-Pd)$_{NCM}$ photocatalysts. The percentage of degradation was significantly increased for the zinc oxide - palladium nanocomposite and nearly attained maximum degradation efficiency of 100 % in 3 hrs under solar irradiation. The result displays that the photocatalytic activities of (ZnO-Pd)$_{NCM}$ are higher than that of ZnO, shown in Fig. 5. Because the palladium metal acts as electron sink, it therefore enhanced the electron-hole charge separation and reduced the charge recombination process. This process promotes the hydroxide radical and superoxide radical generation [12, 13, 16]. These generated active radicals are the effective degradation agents for the CR dye molecules.

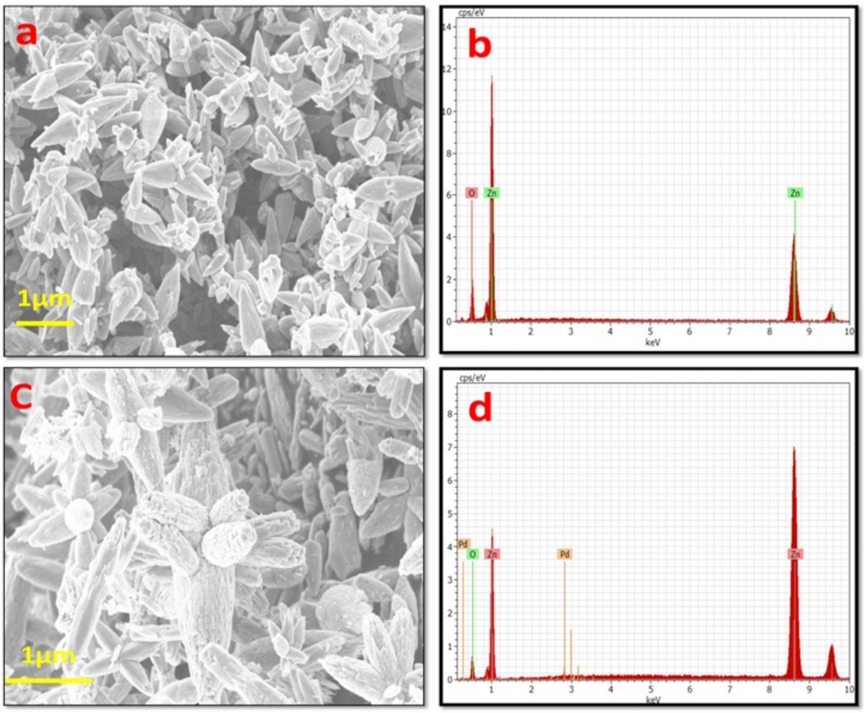

FIG. 4. FE-SEM and EDX spectrum of ZnO (a,b) and (ZnO-Pd)$_{NCM}$ (c,d)

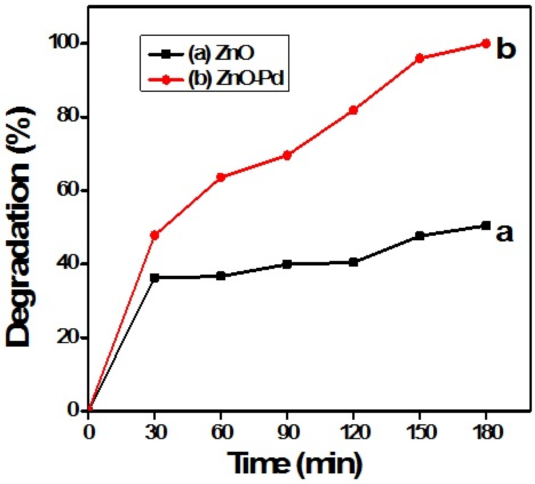

FIG. 5. The photocatalytic degradation of congo red (25 ppm) using (a) ZnO and (ZnO-Pd)$_{NCM}$ using 20 mg/50 ml

3.4.1. Effect of the catalyst loading. This experiment was carried out using different amounts of (ZnO-Pd)$_{NCM}$ (5 to 40 mg/50 ml) catalyst and dye concentration 25 ppm. In Fig. 6, the results showed that the photodegradation efficiency was increased with increasing amounts of catalyst and the maximum efficiency was observed at 20–40 mg of catalyst loading In this case, 20 mg/50 ml catalyst amount was found to have the highest photodegradation efficiency with lower catalyst loading and it's also consider as the optimum amount of catalyst. In general, the amount of catalyst is proportional to the generation of number of active radical such as OH and $O2^{-}$ which rapidly degrade the adsorbed dye molecules. A catalyst at higher loading increases the total active sites of the catalyst but dye molecules is constant at fixed concentration. Hence, the optimum amount of catalyst is enough for the efficient degradation of CR at above optimum concentration [17, 18].

3.4.2. Influence of pH. The influence of initial dye pH value on the degradation efficiency of CR was investigated is shown in Fig. 7. The pH of dye solution was adjusted using dilute sulfuric acid or dilute sodium hydroxide.

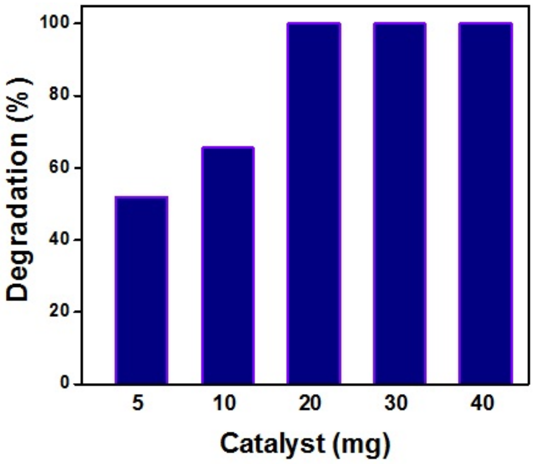

FIG. 6. Photocatalytic degradation of of congo red (25 ppm) using $(\text{ZnO-Pd})_{NCM}$ with different amount of catalyst

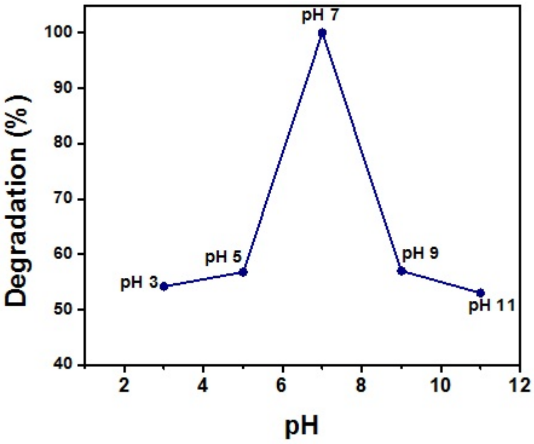

FIG. 7. Effect of dye solution pH on the photocatalytic degradation of congo red (25 ppm) using $(\text{ZnO-Pd})_{NCM}$ 20 mg/50 ml

The result showed that the higher degradation efficiency was observed at neutral pH (pH 7). On the other hand, the degradation efficiency decreased at both acidic and basic pH. From that result the photocatalytic degradation of CR is favorable at neutral pH in presence of $(\text{ZnO-Pd})_{NCM}$ [17–19].

3.4.3. Effect of the initial dye concentration. The effect of initial concentration of CR dye on photodegradation activity was studied by varying the CR dye concentration from to 10 to 40 ppm (Fig. 8). The degradation efficiency of Congo red was high with increased dye concentration up to 25 ppm, however, after that, the degradation efficiency was decreased. This may be due to competition of adsorption between dye molecules and catalyst surface. At higher dye concentrations, the number of dye molecules is high, but the available active sites on the catalyst surface are constant, hence the fixed catalyst amount occupies a fixed number of active sites. Hence, it is possible to have a constant amount of dye molecule adsorption and degradation and it is not enough to degrade a large number of dye molecules (higher concentration) [16–19].

3.4.4. Photocatalytic mechanism. Photocatalytic mechanism of ZnO-Pd nanocomposite for degradation of Congo red is shown in Fig. 9. When sunlight is exposed to the ZnO-Pd nanocomposite, it undergoes photoexcitation followed by electron movement to the conduction band (CB) and the holes are generated in the valence band (VB) of ZnO. The photoinduced holes are captured by surrounding water molecules, producing hydroxyl radicals (OH). Then, the photoinduced electrons can be trapped by oxygen molecules on the catalyst surface and formed superoxide radicals $(O2^{-})$. Afterward, the generated free radicals effectively degraded the CR dye molecules in aqueous solution. Moreover, the electron-hole can be recombining together during the light irradiation and this process is effectively prevented by palladium metal on zinc oxide's surface. At the time, the metal nanoparticle

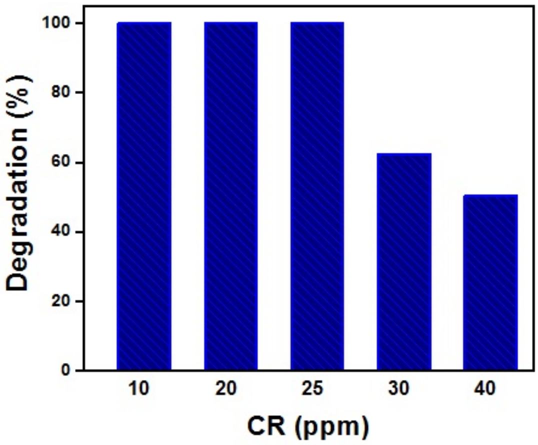

FIG. 8. Effect of initial congo red concentration on the photocatalytic degradation of congo red using $(\text{ZnO-Pd})_{NCM}$ 20 mg/50 ml

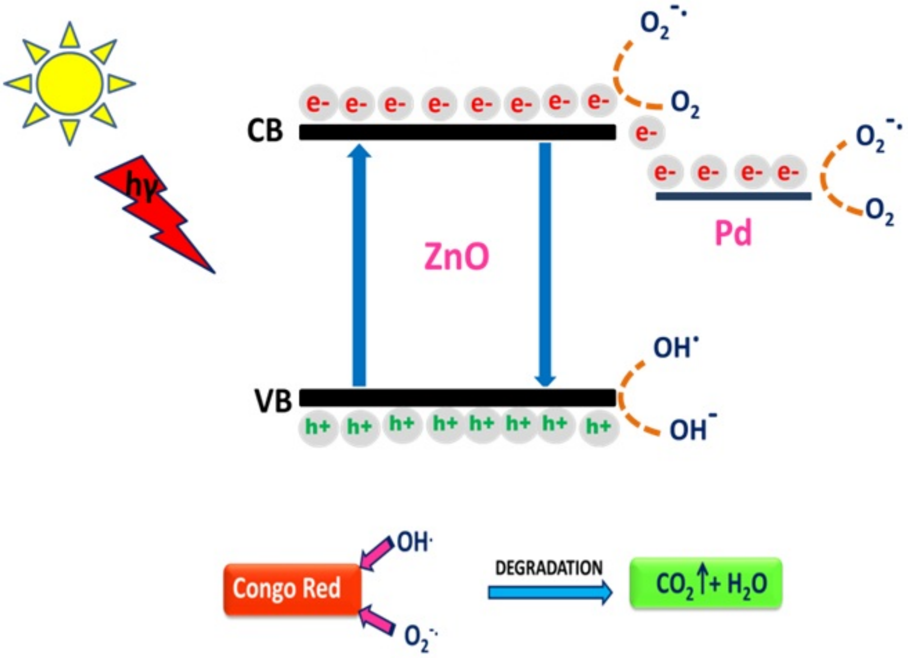

FIG. 9. Photocatalytic mechanism for ZnO-Pd nanocomposite-catalyzed degradation of Congo red

traps the surface electron from conduction band of ZnO and transfers it to oxygen molecules adsorbed on the catalyst surface [12, 13, 20].

4. Conclusion

ZnO and ZnO-Pd nanocomposite materials have been successfully synthesized and characterized by UV-DRS, PL, XRD, EDX and FE-SEM. The UV-DRS displayed the optical properties and PL spectra explained the photochemical charge separation and transfer properties of the materials. The XRD pattern confirmed crystalline nature and EDX analysis confirmed the elemental composition of the materials. The FE-SEM showed the surface morphology of ZnO and ZnO-Pd nanocomposite materials. The photocatalytic activity of $(\text{ZnO-Pd})_{NCM}$ was investigated by the decomposition of Congo red under solar light irradiation. The zinc oxide-palladium nanocomposite material exhibited efficient photocatalytic activity due to synergic effect of palladium and promote the photocatalytic degradation of Congo red.

References

[1] Paola A.D., Lopez E.G., Marci G., Palmisano L. A survey of photocatalytic materials for environmental remediation. *J. Hazard. Mater.*, 2012, **3-29**, P. 211–212.

[2] Hu X., Li G., Yu J.C. Design, fabrication, and modification of nanostructured semiconductor materials for environmental and energy application. *Langmuir*, 2010, **26**(5), P. 3031–3039.

[3] Tong H., Ouyang S., Bi Y., Umezawa N., Oshikiri M., Ye J. Nano-photocatalytic materials: possibilities and challenges. *Adv. Mater.*, 2012, **24**, P. 229–251.

[4] Ahmad M., Zhu J. ZnO based advanced functional nanostructures: synthesis, properties and applications. *J. Mater. Chem.*, 2011, **21**, P. 599–614.

[5] Nithya A., Jothivenkatachalam K. Chitosan assisted synthesis of ZnO nanoparticles: an efficient solar light driven photocatalyst and evaluation of antibacterial activity. *J. Mater. Sci.–Mater. Electron.*, 2015, **26**(12), P. 10207–10216.

[6] Rokesh K., Pandikumar A., Chandra Mohan S., Jothivenkatachalam K. Aminosilicate sol-gel supported zinc oxide-silver nanocomposite material for photoelectrocatalytic oxidation of methanol. *J. Alloys Compd.*, 201; DOI: 10.1016/j.jallcom.2016.04.089.

[7] Ansari S.A., Khan M.M., Ansari M.O., Lee J., Cho M.H. Biogenic synthesis, photocatalytic, and photoelectrochemical performance of Ag-ZnO nanocomposite. *J. Phys. Chem. C*, 2013, **117**(51), P. 27023–27030.

[8] Li P., Wei Z., Wu T., Peng Q., Li Y. Au-ZnO hybrid nanopyramids and their photocatalytic properties. *J. Am. Chem. Soc.*, 2011, **133**, P. 5660–5663.

[9] Zong Y., Li Z., Wang X., Ma J., Men Y. Synthesis and high photocatalytic activity of Eu-doped ZnO nanoparticles. *Ceram. Int.*, 2014, **40**, P. 10375–10382.

[10] Xie W., Li Y., Sun W., Huang J., Xie H., Zhao X. Surface modification of ZnO with Ag improves its photocatalytic efficiency and photostability. *J. Photochem. Photobiol. A*, 2010, **216**, P. 149–155.

[11] Georgekutty R., Seery M.K., Pillai S.C. A highly efficient Ag-ZnO photocatalyst: synthesis, properties, and mechanism. *J. Phys. Chem. C*, 2008, **112**, P. 13563–13570.

[12] Chang Y., Xu J., Zhang Y., Ma S., Xin L., Zhu L., Xu C. Optical properties and photocatalytic performances of Pd modified ZnO samples. *J. Phys. Chem. C*, 2009, **113**, P. 18761–18767.

[13] Zhang Y., Wang Q., Xu J., Ma S. Synthesis of Pd/ZnO nanocomposites with high photocatalytic performance by a solvothermal method. *Appl. Surf. Sci.*, 2012, **258**(24), P. 10104–10109.

[14] Zeng Y., Lou Z., Wang L., Zou B., Zhang T., Zheng W., Zou G. Enhanced ammonia sensing performances of Pd-sensitized flowerlike ZnO nanostructure. *Sens. Actuators, B,* 2011, **156**, P. 395–400.

[15] Zhong J.B., Li J.Z., He X.Y., Zeng J., Lu Y., Hu W., Lin K. Improved photocatalytic performance of Pd-doped ZnO. *Curr. Appl. Phys.*, 2012, **12**, P. 998–1001.

[16] Erdemoglu S., Aksu S.K., Sayılkan F., Izgi B., Asilturk M., Sayılkan H., Frimmel F., Guçer S. Photocatalytic degradation of congo red by hydrothermally synthesized nanocrystalline TiO_2 and identification of degradation products by LC-MS. *J. Hazard. Mater.*, 2008, **155**, P. 469–476.

[17] Jothivenkatachalam K., Prabhu S., Chandra Mohan S., Jeganathan K. Solar, visible and UV light photocatalytic activity of $CoWO_4$ for the decolourization of methyl orange. *Desalin. Water Treat.*, 2014, P. 1–12, DOI: 10.1080/19443994.2014.906324.

[18] Jothivenkatachalam K., Prabhu S., Nithya A., Jeganathan K. Facile synthesis of WO_3 with reduced particle size on zeolite-Y and enhanced photocatalytic activity. *RSC Adv.*, 2014, **4**, P. 21221–21229.

[19] Subash B., Krishnakumar B., Swaminathan M., Shanthi M. Highly active Zr co-doped Ag-ZnO photocatalyst for the mineralization of acid black 1 under UV-A light illumination. *Mater. Chem. Phys.*, 2013, **141**, P. 114–120.

[20] Khalil A., Gondal M.A., Dastageer M.A. Augmented photocatalytic activity of palladium incorporated ZnO nanoparticles in the disinfection of Escherichia coli microorganism from water. *Appl. Catal. A*, 2011, **402**, P. 162–167.

NANOSYSTEMS: PHYSICS, CHEMISTRY, MATHEMATICS, 2016, 7 (4), P. 747–751

Electrochemical synthesis of p-type copper oxides

C. V. Niveditha, M. J. JabeenFatima, S. Sindhu*
Department of Nanoscience and Technology, University of Calicut, Kerala–673635, India
*sindhu.swaminath@gmail.com

PACS 82.45. Aa, 81.07.-b, 87.80Kc, 82.45Yz **DOI 10.17586/2220-8054-2016-7-4-747-751**

Copper oxide is a narrow band gap, low cost, nontoxic, photoactive metal oxide and can be considered as the best candidate for photo-electrochemical applications. Thin films of p-type copper oxide are prepared by cyclic voltammetric technique. The electrochemical method is a cost effective low temperature technique for the preparation of functional thin films. Tools like, GIXRD, Raman Spectroscopy, UV-Vis Spectroscopy, PL, SEM and EIS analysis are done to study the structure, phase, optical, morphological and electrochemical behavior of the copper oxide thin film. The effect of deposition conditions on the electrical and optical properties of the thin films are analyzed in detail.

Keywords: cyclic voltammetry, electrochemical impedance analysis.

Received: 14 February 2016

Revised: 26 April 2016

1. Introduction

Copper oxide is a low cost, non-toxic, narrow band gap metal oxide [1]. Oxides of copper crystallize mainly in two forms, cuprous oxide (Cu_2O) and cupric oxide (CuO) [1, 2]. Cuprous oxide is a direct bandgap [1] and cupric oxide is an indirect band gap [1] metal oxide. These metal oxides exhibit interesting properties suitable for catalytic [3], electrochromic [4], electrochemical [4], photoelectrochemical [5] and photovoltaic applications [4]. Due to the narrow band gap (Cu_2O – 1.9–2.2 eV and for CuO is 1.2–1.7 eV) it has high potential in photovoltaic and photoelectrochemical applications. Commonly, copper oxide films have been synthesized by the high temperature thermal oxidation of copper metal [6] that limits the control over the interfacial features like surface area, particle size, and grain boundaries etc, which affect the optical and electrochemical properties. Hence, the present study focus on electrodeposition method [7] which is an attractive method for thin film synthesis under low temperature conditions. The efficiency of electronic and charge transfer mechanism between the nanoparticles or the nanoparticles and the adjacent layer depends highly on the shape and size of the particles participating in the process. This highlights the significance of deposition of size and shape controlled nanostructures by electrochemical deposition.

2. Experimental method

Electrodeposition of copper oxide is done using three electrode system, where cleaned FTO is used as the working electrode, platinum wire as counter electrode and Ag/AgCl as reference electrode. The Cu_2O is deposited on the FTO substrate under neutral pH the potential is swept between 0 V to -0.8 V from the solution containing 5 mM $CuSO_4$ and 50 mM KNO_3 and repeat the cycles three times to get a yellow colored film. The CuO is deposited from solution containing 5 mM $CuSO_4$ and 50 mM KNO_3 under acidic (2.5 mM H_2SO_4) pH the potential is swept between 0 V to -0.8 V and repeat the cycles three times to obtain a black colored film. Fig. 1 shows the photographs of the obtained yellow and black films of copper oxides.

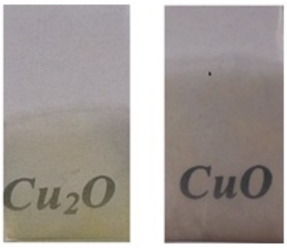

FIG. 1. Photographs of Cu_2O and CuO films

3. Result and discussion

3.1. Cyclic voltammetry

Figure 2 depicts the cyclic voltammogram for the electrodeposition of both Cu_2O and CuO. Cu_2O formed under neutral pH. In Fig. 2(a), the peak at -0.21 V shows the film formation and there are two peaks at Fig. 2(b) shows the conversion of Cu^{2+} ion from Cu^{+}ion i.e, the formation of CuO. The Cu^{2+} ion accepts an electron from the electrode and becomes a Cu^{+} ion to attain a stable electronic configuration. The positive nature of the metal ion helps, forming weak Van der Waals interactions with the non-bonded electrons of oxygen atom of the water and the adsorbed Cu-H_2O complex on FTO substrate is neutralized by releasing H^{+} ion, which resulted in the deposition of Cu_2O. An increase in cathodic current is found near a cathodic potential of -0.21 V, indicating the deposition of Cu_2O film. When the cycle is repeated, the deposition current diminishes with an increase in film coverage on the substrate, since Cu_2O is less conducting than FTO. But at acidic pH, the H^{+} ion from H_3O^{+} ion complex reduced by accepting electron from Cu^{+} ion, leads to the formation of Cu^{2+} ion which is the then converted into CuO.

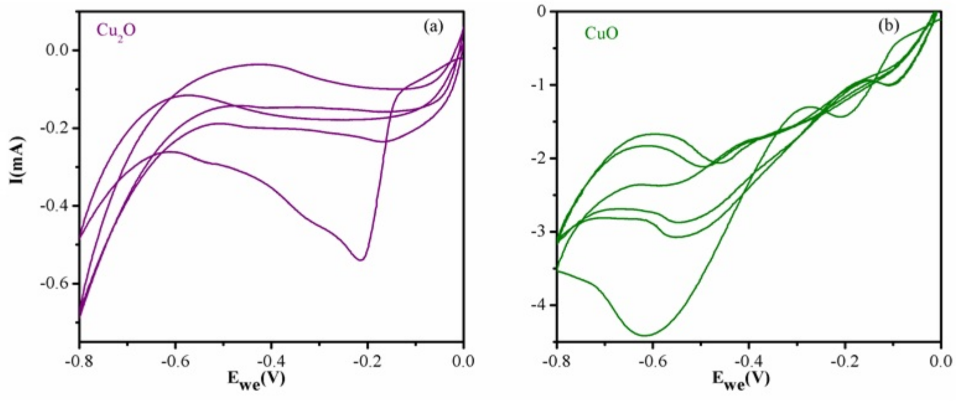

FIG. 2. Cyclic voltammogram of electrodeposition of (a) Cu_2O and (b) CuO

3.2. Structural analysis

The crystallinity of the deposited films was analyzed using a grazing angle X-ray diffraction (GIXRD). Fig. 3 depicts the XRD spectra of the deposited films and is compared with standard JCPDS files 78-2076, 80-1917, which correspond to cubic and monoclinic crystal structures respectively for cuprous and cupric oxide of space groups Pn3m and C1c1. In cubic Cu_2O, the copper atoms are at fcc sub lattices and oxygen atoms are at bcc sub lattices [8]. In the case of monoclinic CuO, the copper atom is coordinated by four oxygen atoms in an approximately square planar configuration and the oxygen is coordinated to four copper atoms at the corners of a distorted tetrahedron [9].

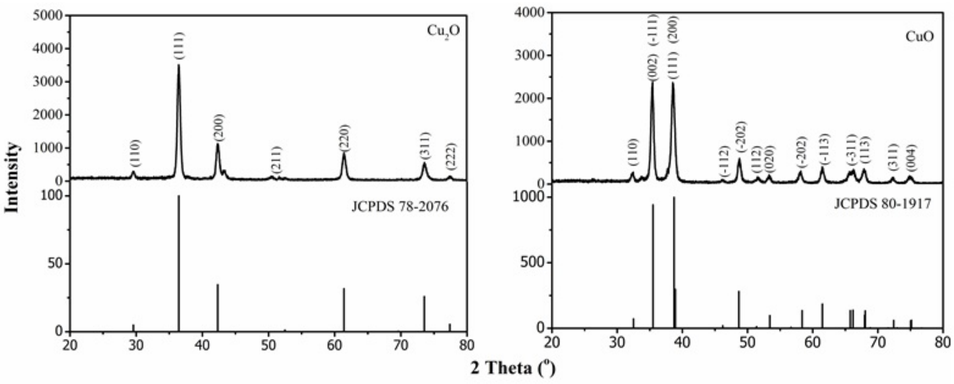

FIG. 3. XRD spectra of Cu_2O and CuO films compared with standard JCPDS

3.3. Morphology

The morphology of the film obtained from SEM analysis. Fig. 4 depicts the average size of Cu_2O is 75 nm and that of CuO is 93 nm. The morphology of Cu_2O is square in shape, while that of CuO is spherical shape.

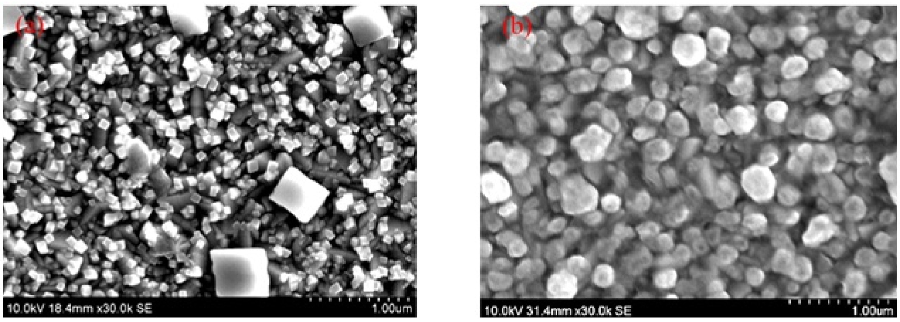

FIG. 4. SEM image of Cu_2O and CuO films

3.4. Optical properties

Optical properties of the films were analyzed by using UV-Visible spectroscopy. The absorption spectra and Tauc plots for Cu_2O and CuO are shown in Fig. 5. The band gap is estimated from the Tauc plot and the obtained values are 2.43 eV and 1.73 eV respectively for Cu_2O and CuO. The PL spectra give idea about the defect state. Fig. 6 depicts three peaks in the PL spectra corresponding to band edge emission, oxygen ion vacancy and copper ion vacancy [10]. The band edge emission is slightly red shifted (562 nm) in the case of cupric oxide than cuprous oxide (527 nm). All the defect emissions are also red shifted. The p-type nature of the films is due to the presence of copper ion vacancies.

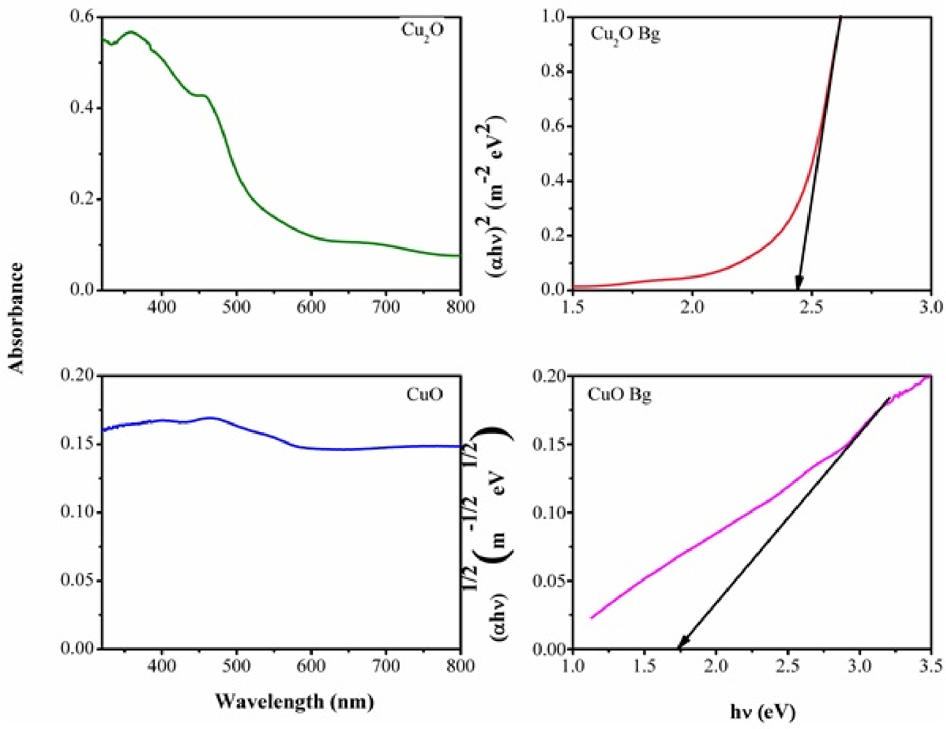

FIG. 5. UV-Visible spectra and Tauc plot of Cu_2O and CuO films

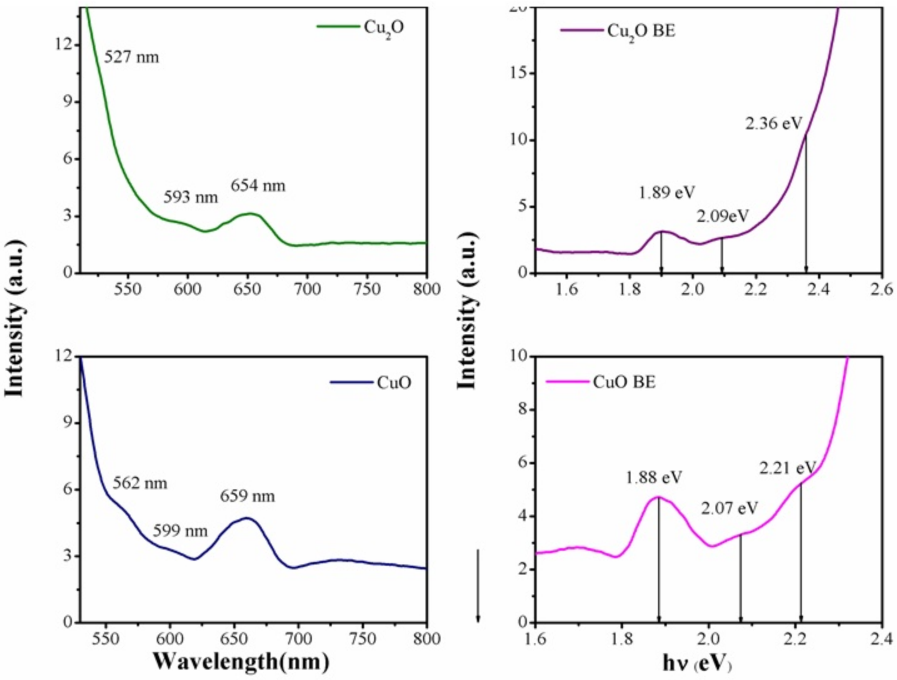

FIG. 6. PL spectra of Cu_2O and CuO films

3.5. Electrical properties

The electronic properties of the films are studied using hall measurement system. From this measurement both Cu_2O and CuO are p-type semiconductors with conductivity of 4.71×10^2 Scm^{-1} and 4.12×10^3 Scm^{-1} respectively. Fig. 7. depicts the Nyquist plots obtained from electrochemical impedance (EIS) analysis of copper oxides, which measure the interfacial resistance between the electrode and electrolyte in the dark and light condition. This analysis confirms the photo activity of copper oxide. Cu_2O is more photoactive than CuO.

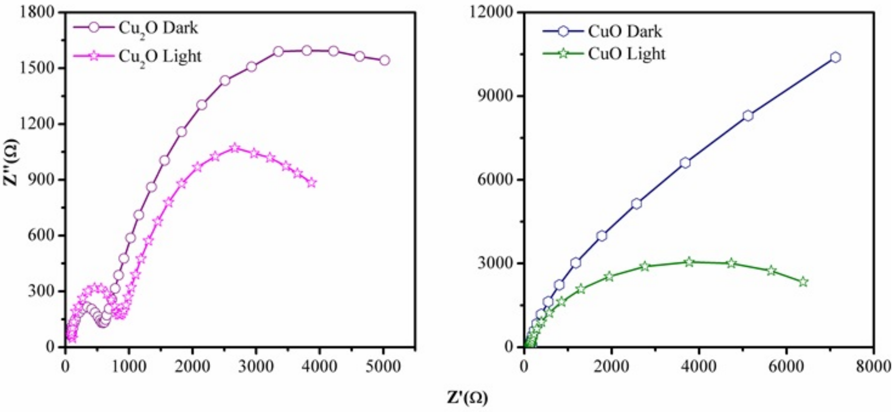

FIG. 7. Nyquist plots of electrodeposited Cu_2O and CuO films

The efficiency of the cell was obtained from chronoamperometric analysis in 0.1 M Na_2SO_4 electrolyte by using three electrode system where deposited film was a working electrode, Pt wire was a working electrode and Ag/AgCl was the reference electrode. The efficiency is calculated from equation 1, where η is the efficiency of the cell, I is the steady current density obtained from I-t curves (shown in Fig. 8), V is the applied potential -0.2 V and J_{Light} is the irradiance intensity of 100 mW/cm^2. The efficiencies obtained for Cu_2O and CuO were 0.5 % and 0.2 % respectively.

$$\eta = \frac{I(1.23 - V)}{J_{Light} \cdot 100}. \tag{1}$$

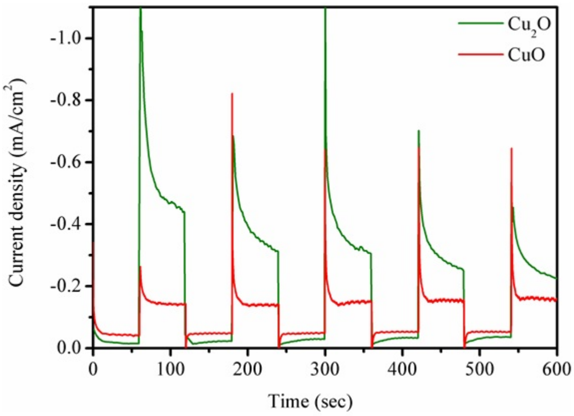

FIG. 8. Chronoamperometric spectra of electrodeposited Cu_2O and CuO films

4. Conclusion

Cyclic voltammetric deposition techniques were utilized to synthesize p-type copper oxides at potentials ranging from 0 V to -0.8 V at a scan rate of 20 mV/s. Cu_2O is formed under neutral pH and CuO is formed at lower pH values. The band gaps of both copper oxides are narrow ie; 2.43 eV and 1.73 eV for Cu_2O and CuO respectively. The p-type nature is confirmed from Hall measurement system. Both are p-type copper oxides. The electrochemical impedance analysis shows that the cuprous oxide thin films are more photoactive than cupric oxide, which was confirmed through chronoamperometric analysis. The efficiencies of Cu_2O and CuO were 0.5 % and 0.2 % respectively.

Acknowledgement

Authors Niveditha C.V. and Jabeen Fatima acknowledge CSIR for financial assistant in the form of Senior Research Fellowship. Sindhu S acknowledges Kerala State Council for Science Technology and Environment (KSCSTE), Govt. of Kerala, and Council of Scientific and Industrial Research (CSIR), Govt. of India for financial assistance. Support obtained from Satyabhama University, Chennai and NIT Calicut for GIXRD and SEM analysis are greatly acknowledged.

References

[1] Kari E.R.B., Kyoung-Shin C. Electrochemical synthesis and characterization of transparent nanocrystalline Cu_2O films and their conversion to CuO films. *ChemComm*, 2006, P. 3311–3313.
[2] Samarasekara P. Characterization of low cost p-Cu_2O/n-CuO junction, *GESJ.: Physics*, 2010, **2**(4), ISSN-1512-1461.
[3] Yongqian W., et al. Controllable fabrication nanostructured copper compound on Cu substrate by one-step route. *RSC.Adv.*, 2015, P. 1–17.
[4] Ahmad S.Z., et al. Nanostructured copper oxide semiconductor: a perspective on materials, synthesis method and applications. *J. Mater. Chem. C.*, 2014, **2**, P. 5247.
[5] Chia-Yu L., et al. Cu_2O/NiO_x nanocomposite as an inexpensive photocathode in photoelectrochemical water splitting. *Chem. Sci.*, 2012.
[6] Kasim U.I., et al. Effect of oxidation temperature on the properties of copper oxide thin films prepared from thermally oxidised evaporated copper thin films. *IOSR-JAP*, 2013, **3**, P. 61–66.
[7] Rachel O., Usha R., Sajeeviraja. Characteristics of electron beam evaporated and electrodeposited Cu_2O thin films-comparative study. *Int. J. Electrochem. Sci.*, 2012, **7**, P. 8288–8298.
[8] Reimann K., Syassen K. Raman Scattering and Photoluminescence in Cu_2O under Hydrostatic Pressure. *Phys. Rev. B*, 1989, **39**, P. 11113–11119.
[9] Ahmad S.Z., Rozina A.R., Anthony J.M., Anthony P.O., Kourosh K. Nanostructured Copper Oxide Semiconductors: A Perspective on Materials, Synthesis Methods and Application. *J. Mater. Chem. C*, 2014, **2**, P. 5247–5270.
[10] Jiji K., Soosen S.M., Anoop C., George K.C. Optical Properties of CuO Nanoparticles. *AIP Conf. Proc.*, 2011, **1391**, P. 576–578.

NANOSYSTEMS: PHYSICS, CHEMISTRY, MATHEMATICS, 2016, 7 (4), P. 752–754

Application of gel electrolyte in dye sensitized solar cells

P. Nijisha, N. M. Bhabhina, S. Sindhu*

Department of Nanoscience and Technology, University of Calicut, Kerala–673635, India

nijisha31@gmail.com, bhabhinanm@gmail.com, *sindhu.swaminath@gmail.com

PACS 88.40.fh, 88.40.H, 88.40.hj, 88.40.J **DOI 10.17586/2220-8054-2016-7-4-752-754**

The volatility of liquid electrolytes has been a major problem for their application in dye-sensitized solar cells (DSSC). In this study, liquid electrolyte was replaced by polymer based gel electrolyte. Polyvinyl alcohol is chosen as the polymeric matrix to gelate the liquid electrolyte with iodide-triiodide redox couple and suitable organic solvent. The amorphous nature and the physical cross linking formed between polymer-polymer and polymer-solvent is analyzed from XRD and FT-IR. Cell was fabricated and characterization was done. I-V and EIS measurements of the cell was taken. Easy fabrication and its advantages over liquid electrolyte makes gel electrolyte a promising alternative for liquid electrolyte.

Keywords: dye sensitized solar cells, quasi solid state dye sensitized solar cells, gel electrolyte.

Received: 14 February 2016. Revised: 26 April 2016.

1. Introduction

DSSC have received great attention owing to their low production costs and high efficiencies [1, 2]. The certified record efficiency of DSSC is 12–13 %. A DSSC consists of a photo anode, a semiconductor film coated on a transparent conducting oxide layer, which is dye sensitized, a counter electrode, usually FTO coated with a catalytic material and electrolyte which includes a redox couple usually I^- / I_3^- system and a suitable solvent. In DSSC, the electrolyte is the medium for charge transportation between the two electrodes and acts as a source for dye regeneration [3]. The long term stability of the device strongly depends on the electrolyte component [4]. The highest efficiency reported in DSSC was by employing liquid electrolyte. But there are some practical impediments when using this liquid electrolyte like leakage while sealing and volatilization of the solvent, desorption and photo-degradation of the attached dye, corrosion of the counter electrode etc., which prevent DSSC's from further application and commercialization [4, 5]. So, as an alternative to liquid electrolyte, solid state electrolytes and quasi solid state electrolytes (gel electrolytes) were introduced. Though solid state electrolytes seem to be an ideal material for DSSC, the efficiency was not up to expectations [6]. This might be due to poor interfacial contact and poor charge carrier mobility. When coming to gel electrolyte, all the problems related to liquid and solid state electrolyte can be resolved. It remains as quasi solid at room temperature and as a highly viscous liquid at high temperatures. Thus, a gel electrolyte possesses both the cohesive property of solid as well as diffusive transport property of liquid [7]. In the present work a polymer-based gel electrolyte is synthesized and its behavior in the performance of dye sensitized solar cell is studied by using two different photoanode materials – TiO_2 and ZnO.

2. Experimental

2.1. Materials

Fluorine doped tin oxide (FTO-7Ω/Sq.), N719 ($Ru(dcbpy)_2(NCS)_2$) -95%), Hexachloroplatinic acid (H_2PtCl_6), Potassium iodide (KI) (bio ultra, 99.5 %), Polyvinyl alcohol (PVA, 99 % hydrolyzed) were purchased from Sigma-Aldrich. Dimethyl sulfoxide (DMSO) and Iodine (I_2) is supplied by MERCK.

2.2. Gel electrolyte synthesis

Polyvinyl alcohol is used as the polymeric matrix. Gel electrolyte is prepared by adding adequate amount of polymer, KI and I_2 to dimethyl sulfoxide. The resulting mixture is heated to 2 hrs and stirred continuously to obtain the gel.

2.3. Assembling of quasi solid state dye sensitized solar cell

The nanocrystalline TiO_2 photo anode was fabricated by doctor blading TiO_2 paste on FTO substrate. The film was air dried and sintered at 450°C for 30 mins. The sintered sample was then cooled to room temperature and was dipped in the dye solution for 24 hrs. The dye loaded sample was then air dried and sealed. The counter electrode was made by electrodepositing Pt on FTO surface. The two electrodes were then kept face to face with gel electrolyte in between to obtain a sandwich structure and is then clamped tightly.

3. Results and discussion

3.1. Gel characterization

Figure 1 shows the FT-IR of pure PVA and PVA based gel electrolyte. The presence of broad band at 3416 shows the inter-molecular hydrogen bonding. In PVA-G, the intensity of the band was found to increase, and this is because of extensive hydrogen bonding between the polymeric chains due to its complete expansion. The band at 2914 cm^{-1} shows the –CH- stretching vibration. The band at 1654 cm^{-1} is for terminal vinyl group. Bands at 1783 cm^{-1} and 1806 cm^{-1} correspond to the ester group present. The 1315 cm^{-1} and 1434 cm^{-1} bands correspond to S-O stretching, while those at 1024 cm^{-1}, 1083 cm^{-1}, 1186 cm^{-1} show the C-O vibration of PVA.

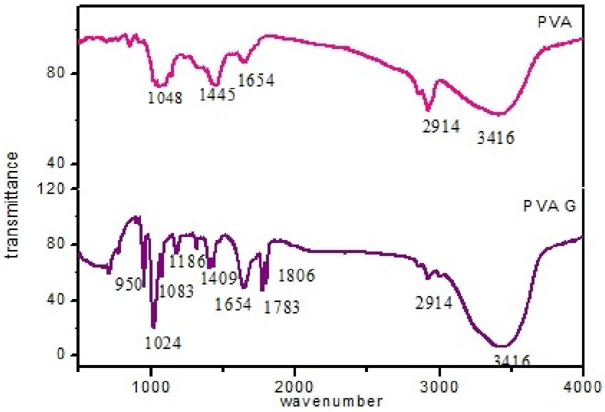

FIG. 1. FT-IR spectra of pure PVA and PVA gel electrolyte

The XRD spectra of gel electrolyte, pure PVA, KI, and I_2 are shown in figure 2. Diffraction peak at 2θ – 40.76 is ascribed to pure PVA. Diffraction peak at 2θ – 21.67, 30.80, 54.98 and 24.62, 25.07, 29.04 is for pure KI and I_2 respectively, shows the crystalline nature of the ionic salt. An amorphous peak is observed for polymer gel electrolyte, which shows the complete dissolution of the ionic salt and also increased liquid electrolyte uptake by the matrix.

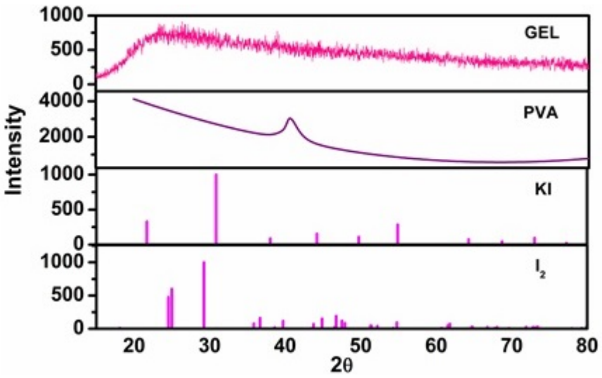

FIG. 2. XRD of pure I_2, KI, PVA and polymer gel electrolyte

3.2. Cell characterization

The current-voltage characteristics and Nyquist plot of the DSSCs based on polymer gel electrolyte were performed with two different photoanode semiconductor materials-TiO_2 and ZnO. The table below summarizes the best values of their photovoltaic parameters.

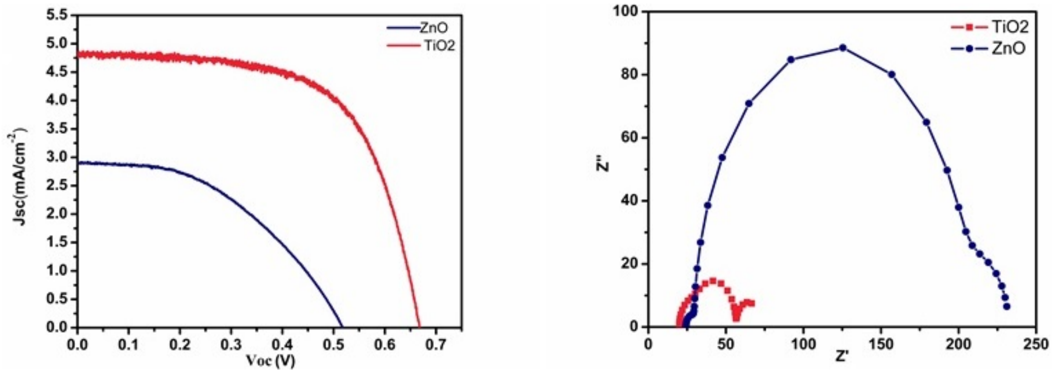

FIG. 3. (a) Jsc-Voc curve, (b) nyquist plot of the cell

TABLE 1. Photovoltaic parameters of TiO_2 and ZnO based DSCs with gel electrolyte

Photoanode material	**Jsc(mA/cm^2)**	**Voc(V)**	**FF(%)**	**Eff(%)**
TiO_2	1.21	0.67	63.6	2.05
ZnO	0.723	0.517	45.8	0.684

The obtained efficiencies are 2.05 and 0.68 % respectively for TiO_2 and ZnO based DSSC with PVA gel electrolyte. Here, the pure PVA based gel electrolyte of KI/I_2 in DMSO/EC mixture without ionic liquid and any additives or fillers is used. An enhancement in the efficiency is anticipated with ionic liquid and other additives in the gel electrolyte and more studies in this direction are ongoing to enhance the efficiency. The efficiency values are low compared to perovskite-based DSSC. Perovskites give better efficiency and absorption coefficient as a sensitizer along with conventional electrolytes. However, focus of current work is on the synthesis of gel electrolyte, a better substitute for liquid electrolytes, and its application in electrochemical cells.

The charge transfer or transport behavior of the cell was measured by utilizing electrochemical impedance spectroscopy. The three semicircle from left to right gives the electrochemical behavior at the Pt counter electrode,TiO_2/dye/electrolyte interface and Warburg diffusion. The resistance offered at each interface when using ZnO as photoanode is very high when compared to the cell fabricated with TiO_2 as the photoanode. This confirms the lower performance of the ZnO-based quasi solid state dye sensitized solar cell.

4. Conclusion

PVA based polymer gel electrolyte was synthesized. DSSC were fabricated with two different photoanode materials to study the performance of the cell. Photovoltaic studies show that the gel works well with TiO_2-based solar cell, displaying an overall efficiency of 2.05 %.

References

[1] O'Regan B., Gratzel M. A low-cost, high-efficiency solar cell based on dye-sensitized colloidal TiO_2 films. *Nature*, 1991, **353**, P. 737–740.

[2] Yuh-Lang Lee., Yu-Jen Shen., Yu Min Yang. A hybrid PVDF-HFP/nanoparticle gel electrolyte for dye-sensitized solar cell application. *Nanotechnology*, 2008, **19**, P. 455201.

[3] Nogueira A.F., Longo C., De Paoli M.A. Polymers in dye sensitized solar cells: overview and perspectives. *Coordination Chemistry Reviews*, 2004, **248**, P. 1455–1468.

[4] Jo-Lin Lan, Tzu-Chien Wei, et al. Effects of iodine content in the electrolyte on the charge transfer and power conversion efficiency of dye sensitized solar cells under low light intensities. *The J. Phys. Chem. C*, 2012, **116**, P. 25727–25733.

[5] Kun Seok Lee, Yongseok Jun, Jong Hyeok Park. Controlled Dissolution Of Polystyrene nanobeads: Transition from Liquid Electrolyte to Gel Electrolyte. *Nano Lett.*, 2012, **12**, P. 2233–2237.

[6] Chih-Hung Tsai, Chun-Yang Lu, et al. Efficient gel-state dye-sensitized solar cells adopting polymer gel electrolyte based on poly(methyl methacrylate). *Organic electronics*, 2013, **14**, P. 3131–3137.

[7] Wataru Kubo, Kei Murakoshi, et al. Quasi-solid-state dye-sensitized TiO_2 solar cells:Effective charge transport in mesoporous space filled with gel electrolytes containing iodide and iodine. *J.Phys.Chem. B*, 2001, **105**, P. 12809–12815.

NANOSYSTEMS: PHYSICS, CHEMISTRY, MATHEMATICS, 2016, 7 (4), P. 755–758

An investigative study on application of carbon nanotubes for strain sensing

M. R. Khodke[1], Satishchandra V. Joshi[2]

[1]Mechanical Engineering Department, Vishwakarma Institute of Technology Pune–411037,
Maharashtra, India

[2]Principal, Padmabhushan Vasantraodada Patil Institute of Technology, Budhgaon–416304,
Sangli, Maharashtra, India

moreshwar.khodke@vit.edu, joshisv17@gmail.com

PACS 61.48.De; 07.10.Pz; 73.50.Dn **DOI 10.17586/2220-8054-2016-7-4-755-758**

Traditional strain sensors, such as metal foil gauges, can measure the strains only on the structural surface in designated directions and locations. Hence, there is a need to develop new types of strain sensors which can function on both the micro-and macro-scale, either on the surface or embedded in the structure, and able to behave as multifunctional materials. Owing to its outstanding electrical and mechanical properties carbon nanotubes (CNTs) can be used as strain sensing material. A film (Bucky paper/CNT network) made from multiwalled carbon nanotubes by use of solvent/surfactant and vacuum filtration method is used as strain sensor.

The paper discusses the experimental work involving preparation of CNT film sensor specimen, its application on aluminum and brass strips along with conventional foil gauge and subjecting the metal strips to axial loading to measure gauge factor. It was found that CNT film strain sensor shows linear relationship between change in resistance and strain. Furthermore, the gauge factor increases as the film aspect ratio increases, and for the same aspect ratio, a higher gauge factor was observed for brass than aluminum.

Keywords: carbon nanotube, strain sensor, bucky paper, sensitivity, gauge factor.

Received: 22 March 2016

1. Introduction

Mechanical strain sensors are widely used for structural health monitoring and vibration control. Traditional strain sensors such as strain gauges are sensitive, stable, of low cost and easy to use. However, strain gauges can only measure the strains on the structural surface in designated directions and locations; also strain sensing is usually the only function they can offer. Carbon nanotubes (CNTs) possess excellent physical and chemical properties [1] and strain sensor made of carbon nanotube material can alleviate this difficulty and can behave as multifunctional material.

Comprehensive reviews on sensors based on carbon nanotubes and their composites are presented by Christofer Hierold et al. [2] and Chunyu Li et al. [3]. A study by Dharap et al. [4] showed that pure SWCNT films (‘bulky paper’) can serve as strain sensors if they are bonded to the structural surface as conventional strain sensors.

Strain sensitivity is one of the most important parameters to consider and is expressed as the gauge factor (GF), a dimensionless number describing the change in resistance as a ratio of applied strain, and is given by [5]:

$$GF = \frac{\text{Relative change in resistance}}{\text{Applied strain}} = \frac{\left({}^{\Delta R}\!/_{R}\right)}{\varepsilon}. \tag{1}$$

The effect of aspect ratio on sensitivity of CNT film sensor is not reported in the literature. The investigation of this relationship is the objective of this study.

2. Carbon nanotube film

Many applications of CNT film are reported in the literature [6]. Some of them are in field emission, energy storage and conversion, electronics, humidity and temperature sensor, gas sensors, bio sensor etc. The methods for preparation of CNT film are chemical vapor deposition growth, electrophoretic deposition, drop drying from solvent etc. Vacuum filtration method as outlined in [7] is used in this study.

2.1. Preparation of CNT Film

Multiwalled carbon nanotubes (MWCNTs) having an average inner and outer diameters 4–13 nm, and length of 1–4 μm was procured from D & D Advanced Materials, Pune, India. 25 mg of MWCNT, as procured, was mixed in 100 ml of Dimethylformamide (DMF) solvent. DMF-MWCNT solution was then ultrasonicated in a bath sonicator (DC-80H, MRC, 80 W) for 3 hours and by an ultrasonic tip (Vibra-Cell VCX130, Sonics, USA) for 20 min in an alternating sequence. CNT suspension was then filtered by using vacuum filtration method. The film is peeled off from filter paper and dried in oven at 60 to 80 °C for 12 hours. The film after drying is cut in required aspect ratios and used as strain sensor.

3. Experimental setup

The setup consists of Universal Testing Machine (UTM) for tensile loading (1–10 kN) of specimens and Agilent 34410A digital multimeter for measuring the resistance change. The CNT film strain sensors and conventional metal foil strain gauge are bonded on opposite side of on aluminum or brass strip by epoxy adhesive. The terminals for the electrical resistance measurements were taken from film through silver paste.

Four sensors of different aspect ratio as mentioned in Table 1, were used on Aan aluminum strip of size 300 mm×30 mm×3 mm and on a Brass strip of size 300 mm×50 mm×6 mm.

TABLE 1. Specifications of CNT Film and metal foil strain sensors

Sensor Type	**CNT Film Size**	**Aspect Ratio**	**Used on**	**Initial Resistance, R_0, Ohm**
Sensor 1	30 mm × 10 mm	3:1	Aluminium Strip	19.0365
Sensor 2	20 mm × 10 mm	2:1	Aluminium Strip	11.2752
Sensor 3	10 mm × 10 mm	1:1	Aluminium Strip	5.0815
Sensor 4	30 mm × 10 mm	3:1	Brass Strip	42.1362
Metal Foil 1			Aluminium Strip	349.565
Metal Foil 2			Brass Strip	350.005

4. Results and discussion

The relative change in resistance with respect to applied strain for three CNT film sensors, Sensor 1 to 3 and conventional metal foil gauge applied on aluminum strip is shown in Fig. 1.

The relative change in resistance with respect to applied strain for sensor 4 and one conventional metal foil gauge applied on brass strip is shown in Fig. 2.

Gauge factor is slope of straight line fitted in the graphs shown in Fig. 1 and Fig. 2. The gauge factors were determined for all these six sensors using equation (1) i.e. slope of straight lines fitted are listed in Table 2.

TABLE 2. Gauge factors for CNT sensors of different aspect ratio

Sensor Type	**Film Size**	**Aspect Ratio**	**Used on**	**Initial Resistance, R_0, Ohm**	**Gauge Factor observed**
Sensor 1	30 mm × 10 mm	3:1	Aluminium	19.0365	1.05
Sensor 2	20 mm × 10 mm	2:1	Aluminium	11.2752	0.59
Sensor 3	10 mm × 10 mm	1:1	Aluminium	5.0815	0.38
Sensor 4	30 mm × 10 mm	3:1	Brass	42.1362	1.38
Metal Foil 1			Aluminium	349.565	2.10
Metal Foil 2			Brass	350.005	1.99

Gauge factor for metal foil strain gauge as supplied by the manufacturer is 2.0, which validates the observations shown in Table 2.

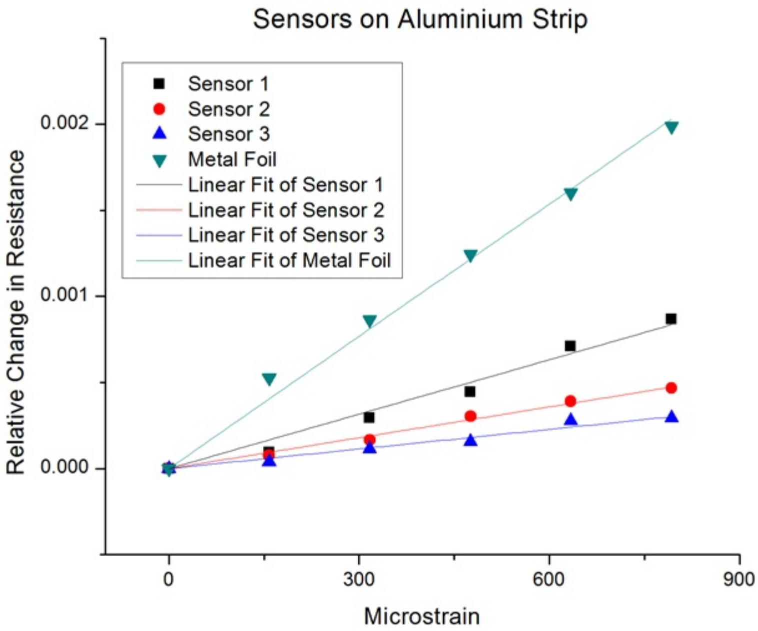

FIG. 1. Relative resistance change vs applied strain for sensors on Aluminium strip

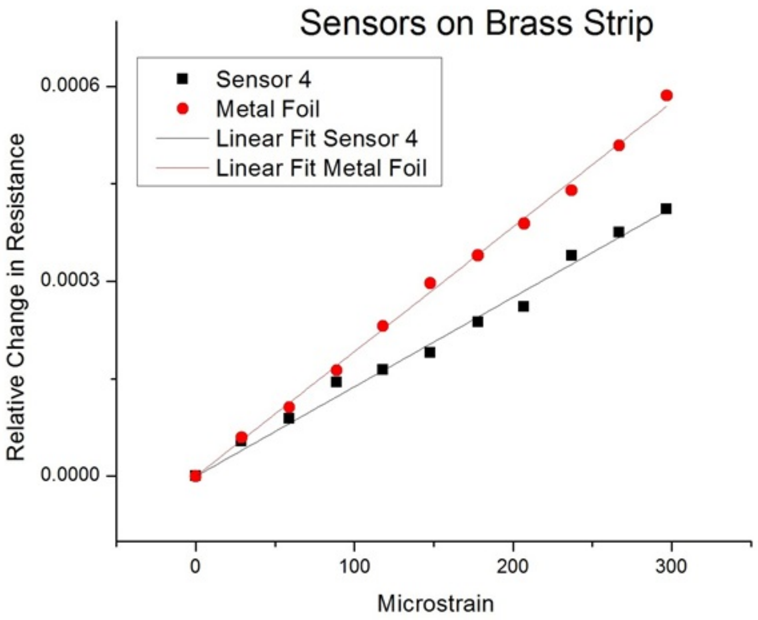

FIG. 2. Relative resistance change vs applied strain for sensors on Brass strip

5. Conclusion and future scope

CNT film sensors show nearly linear response to applied strain similar to conventional metal foil gauges. Sensitivity of CNT film sensor is affected by aspect ratio. Higher aspect ratios were shown to result in better sensitivity. Additionally, a higher gauge factor noted for CNT sensor mounted brass strip than that mounted on an aluminum one, suggesting its better suitability for brass material.

5.1. Future scope

The following two points can be suggested as future scope of study:

1. Magnitude of resistance change for a CNT film is proportional to its initial resistance which in turn depends on its thickness. Hence, resistance change and sensitivity of sensor can be increased by reducing film thickness i.e. by lowering CNT content in film.
2. Alternatively, initial resistance of CNT film can also be increased by manufacturing composite film of CNT with polymers, e.g., Poly Dimethyl Siloxane (PDMS).

Acknowledgement

Authors gratefully acknowledge the Research Grant No. 13ENG001061 received from the Board of College and University Development (BCUD), Savitribai Phule Pune University, Pune, India, for the research work.

References

[1] Dresselhaus M.S., Dresselhaus G., Charlier J.C., Hernandez E., Electronic, thermal and mechanical properties of carbon nanotubes. *Philos. Trans. R. Soc. A Math. Phys. Eng. Sci.*, 2004, **362**(1823), P. 2065–2098.

[2] Hierold C., Jungen A., Stampfer C., Helbling T. Nano electromechanical sensors based on carbon nanotubes. *Sensors Actuators A Phys.*, 2007, **136**(1), P. 51–61.

[3] Li C., Thostenson E.T., Chou T.-W. Sensors and actuators based on carbon nanotubes and their composites: A review. *Compos. Sci. Technol.*, 2008, **68**(6), P. 1227–1249.

[4] Dharap P., Li Z., Nagarajaiah S., Barrera E.V. Nanotube film based on single-wall carbon nanotubes for strain sensing. *Nanotechnology*, 2004, **15**(3), P. 379–382.

[5] Stephan B., Graham E., Michael K., Neil W. *MEMS Mechanical Sensors*. Artech House, Boston, 2004, 86 p.

[6] Zhu H., Wei B. Assembly and applications of carbon nanotube thin films. *J. Mater. Sci. & Technol.*, 2008, **24**(4), P. 447–456.

[7] Rein M.D., Breuer O., Wagner H.D. Sensors and sensitivity: Carbon nanotube buckypaper films as strain sensing devices. *Compos. Sci. Technol.*, 2011, **71**(3), P. 373–381.

NANOSYSTEMS: PHYSICS, CHEMISTRY, MATHEMATICS, 2016, 7 (4), P. 759–764

Synthesis and characterization of neomycin functionalized chitosan stabilized silver nanoparticles and study its antimicrobial activity

R. K. Preethika[1], R. Ramya[2], M. Ganesan[1], S. Nagaraj[3], K. Pandian[2,*]
[1]Department of Chemistry, Thiagarajar College, Madurai–625009, India
[2]Department of Inorganic Chemistry, University of Madras, Guindy Campus, Chennai–600025, India
[3]CASBotany, University of Madras, Guindy Campus, Chennai–600025, India
*jeevapandian@yahoo.co.uk

PACS 82.65.+r **DOI 10.17586/2220-8054-2016-7-4-759-764**

A simple green method was developed for the synthesis of silver nanoparticles in the presence of a neomycin-functionalized chitosan as stabilizing agent using a fresh lemon juice as green reducing agent. The stabilizing agent was synthesized based on the Schiff base formation reaction between the chitosan dialdehyde and neomycin antibiotic in 0.05 mM at pH 7.0. The combined form of neomycin antibiotic with chitosan can be used as stabilizing agent for silver nanoparticles (AgNPs) synthesized by a biogenic method using lemon juice as a green reducing agent. The neomycin functionalized chitosan stabilized AgNPs were characterized by various analytical techniques, including UV-Visible spectra studies, FTIR, XRD and SEM. The antimicrobial activity of these composite was tested against human pathogenic Gram-positive and Gram-negative bacteria. The synergetic effect of the neomycin functionalized chitosan protected silver nanoparticles was tested against various drug resistant microorganisms. These chitosan derivatives can be used in combination with an anti-bacterial agent to treat and inhibit a resistant bacterial infection or the growth of resistant bacterial infection.

Keywords: silver nanoparticles, lemom juice, neomycin, chitosan, antimicrobial activity.

Received: 3 April 2016

Revised: 5 July 2016

1. Introduction

Due to its biocompatibility, biodegradability and non-toxicity, chitosan has increasingly been used in the biomedical and pharmaceutical fields [1–4]. Chemical modifications have been used to prepare chitosan derivatives with enhanced biological and physicochemical properties. Recently, aldehyde-functionalized chitosans have received considerable interest. The preparation of chitosan derivatives containing aldehyde groups have been achieved by reaction with periodates. The latter selectively cleaves the 2, 3 C-C bond and converts chitosan into a dialdehyde derivative [5, 6]. Aldehyde-functionalized chitosans have also been prepared by reaction with nitrous acid (HNO_2) [7–10]. In this method, chitosan undergoes deaminative cleavage of the 1, 4-glycosidic bonds, producing 2, 5-anhydro-D-mannose as the reducing end, which contain an aldehyde group. Hydrogen peroxide was also used to synthesis chitosan containing 2, 5-anhydro-D-mannose recently [11]. The periodate oxidation of chitosan was performed which yielded a dialdehyde chitosan (DAC) that can be used for the construction of biosensor and drug delivery applications [12]. Similarly, chitin and chitosan can be easily processed into hydrogels for various types of biomedical applications such as drug and gene delivery, wound healing and tissue engineering [13–15]. Drug loaded chitosan hydrogels have been generated using diffusion, entrapment and tethering techniques [16]. Chitosan membrane and its derivative have shown a prolonged antibacterial activity and decreased potential toxicity of silver [17, 18].

Recently, a facile and green method was reported in the literature to synthesize stable Ag nanoparticles (AgNPs) with a narrow size distribution. It is well established that chitosan (DAC) and its derivatives were widely used as both a reducing as well as stabilizing agent for the synthesis of metal nanoparticles. In the present study, we investigated the antibacterial activity of both neomycin-functionalized chitosan as well as the combined form of Neo-chit stabilized silver nanoparticles because of the synergetic microbial activity. Here, lemon juice was used to prepare narrow size silver nanoparticles, as previously reported in the literature.

2. Materials and methods

2.1. Materials

Analytical grades chitosan and sodium periodate were purchased from Sigma-Aldrich. The other reagents and solvents were analytical grade. All materials were used without further purification.

2.2. Preparation procedures

2.2.1. Oxidation of chitosan. About 1g chitosan (5.34 mM) was dispersed in 50 ml HCl (10^{-3} M) (pH ranging from 4–5) with magnetic stirring. Then, 1 ml aqueous sodium periodate 0.534 mM was added, the reaction mixture was allowed to stir at 4 °C in the dark for 30 minutes. After completion of the reaction, to eliminate the unreacted periodate, 1 ml of ethylene glycol was added. The oxidized chitosan was washed by distilled water and the sample was frozen and lyophilized for 4 h.

2.2.2. Synthesis of neomycin functionalized chitosan (Neo-Chit). 10 ml of chitosan dialdehyde mixed with 0.05 mM of neomycin sulfate and then the reaction mixture was stirred for 2 h. The powder form of the sample was isolated by by lyophilization after freezing with liquid nitrogen.

2.2.3. Synthesis of silver nanoparticles. 1 ml of freshly prepared lemon juice was diluted with 3 ml of distilled water and then the pH of the solution was adjusted to 11. Then, 2 ml 1 M aq. $AgNO_3$ was added dropwise to the above vigorously-stirred lemon juice solution. The polyphenol group present in the lemon juice reduced the silver ions to silver metal nanoparticles in th aq. medium. The appearance of reddish brown color solution indicated the formation of silver nanoparticles. Then, th silver nanoparticles were isolated via centrifugation.

2.2.4. Neomycin functionalized chitosan stabilized silver nanoparticles. To prepare Neo-Chit stabilized AgNPs, 0.1 g neomycin-functionalized chitosan was mixed with 1 ml of silver nanoparticle solution and then allowed to stir for 30 min. The Neo-Chit @ AgNPs was isolated by centrifugation followed by drying under nitrogen atmosphere in the dark. The powdered samples were collected and stored in dark until further use Fig. 1.

2.2.5. Instrumentation. UV-Visible spectral studies were carried out by using a Shimadzu UV-Visible Spectrophotometer, Japan (Model UV-1800). The characterization of functional groups on the surface of AgNPs performed by FT-IR (perkin-Elmer, Germony) the spectra were scanned over 500 to 4000 cm^{-1}.

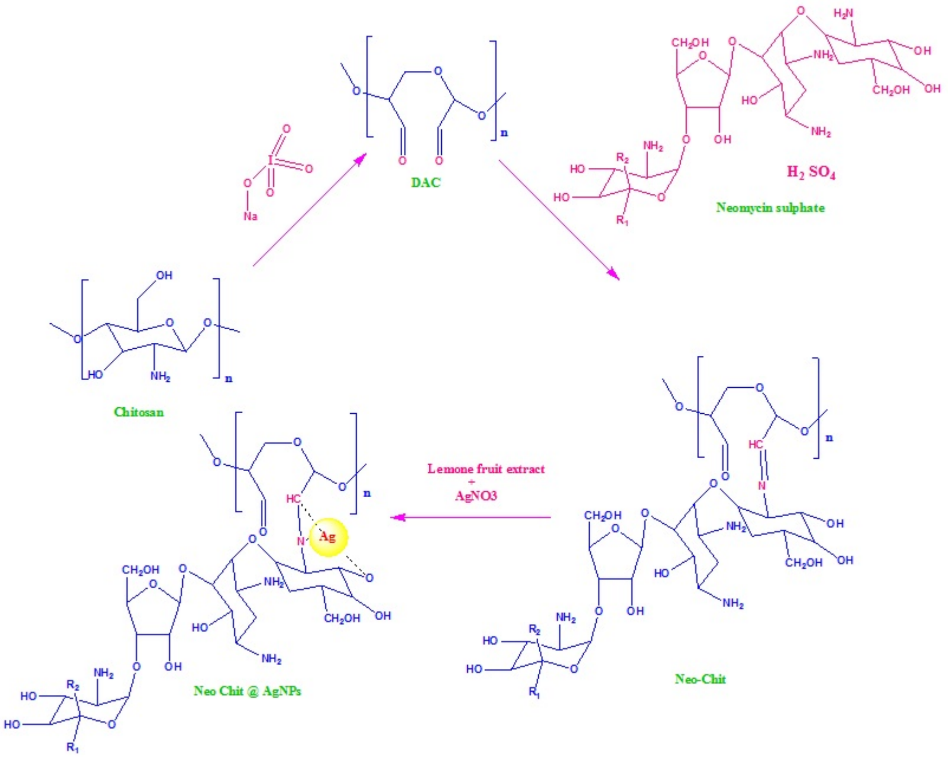

FIG. 1. Schematic representation of the synthetic route of Neomycin functionalized chitosan stabilized silver nanoparticles

3. Result and discussion

3.1. UV-Vis spectroscopy

The UV-Visible spectrum of silver nanoparticles and Neo-chit protected AgNP are shown in Fig. 2. The Plasmon absorption peak was observed at 408 nm which indicated the formation of silver nanoparticles. From the UV-Visible spectral studies, it is clearly seen that the particle size of the silver nanoparticles ranged from 5–20 nm. The peak shape of AgNPs is narrow and sharp, providing evidence for the uniform size distribution of the silver nanoparticles in lemon juice solution. The appearance a sharp Plasmon band is due to the formation of silver nanoparticles having a narrow size range. A slight shift in Plasmon band position is due to the surface modification of silver nanoparticles using neomycin-functionalized chitosan as stabilizing agent. The decrease in Plasmon band position is due to the surface modification of the neomycin functionalized AgNP. The broaderning of the peak position was also observed which is due to the partial aggregated particles of the silver nanoparticles.

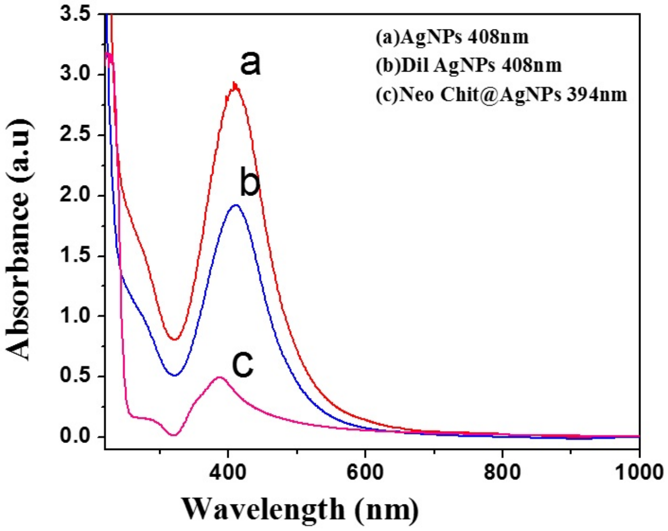

FIG. 2. (a) UV-Visible spectrum of AgNPs obtained from lemon juice reduction method; (b Dilute AgNPs and (c) Neo-chit @ AgNPs

3.2. FT-IR-spectrum of neomycin functionalized chitosan modified AgNPs

The FT-IR spectrum was recorded for both neomycin-functionalized chitosan and neomycin-functionalized chitosan protected silver nanoparticles. The major bands at 2926, 2851, 1746, 881, 774 cm^{-1} are assigned for the characteristic bands for aldehyde group that resulted from periodate mediated oxidation was observed at Fig. 3(b). The bands at 1077 and 1020 cm^{-1} are typical for neomycin-functionalized chitosan modified AgNPs was observed at Fig. 3(c), Table 1.

TABLE 1. FT-IR bands related to chitosan/modified chitosans and their respective assignments

FT-IR band(cm^{-1})	Assignment	FT-IR band(cm^{-1})	Assignment
3356, 2926	N-H,C-H	1071, 1020	C-O-C
3425	O-H	2352, 1323	N-N,NO_2
2851	C-H	2075	O-H
1746	C=O	1077	C-O
1626	C-C	881,774	C-H, NO_3
1406	C=O		

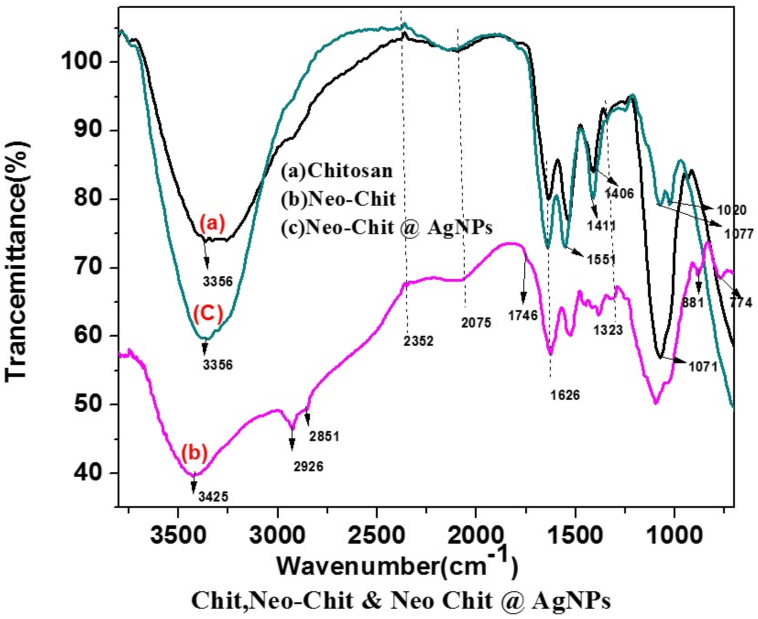

FIG. 3. FT-IR spectrum of chitosan and neomycin functionalized chitosan

3.3. Scanning Electron Microscopic studies

Conventional high vacuum scanning electron microscopy (SEM) images were also taken to envision the structure of oxidized chitosan and Chitosan dialdehyde with neomycine@AgNPs. Fig. 4 shows that there is no change for the stretched out and fibrous network of chitosan, but on the surface of oxidized chitosan one can see a slight degradation of some foliage. The EDX pattern of chitosan dialdehyde with neomycin @ AgNPs is shown in Fig. 5. This pattern shows peaks for the elements **Ag** and **C** are the major components. From these studies, we conclude that the the chitosan dialdehyde-functionalized neomycin stabilizes the AgNPs.

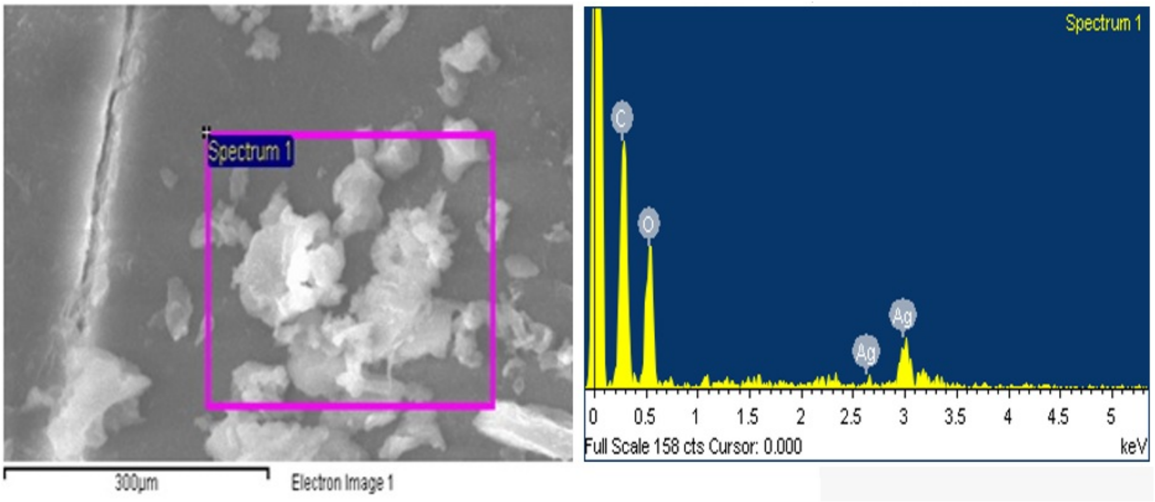

FIG. 4. SEM – EDAX of Chitosan dialdehyde with neomycin @ AgNPs

3.4. Antibacterial activity of Neo-Chit @ AgNP

It is well established that silver nanoparticles with various capping agents have shown excellent antimicrobial activity [18, 19]. In the present study, we demonstrate the antimicrobial activity of silver nanoparticles, neomycin-functionalized chitosan modified AgNPs against various Gram negative and Gram positive bacteria. The disc diffusion method was used for the quantification of inactivation of microbial growth. From the experimental

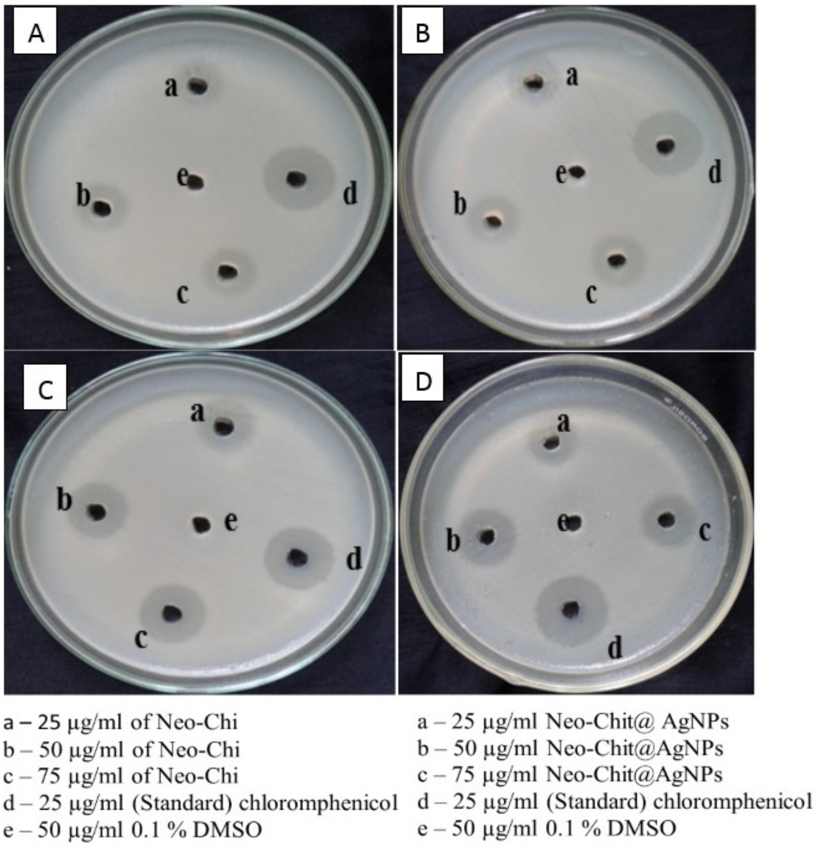

FIG. 5. Antibacterial activity of the Neo-chit and Neo-chit@AgNPs against A, C – Staphylococcus aureus and B, D – Salmonella typhi

studies it is inferred that Neo-chit@AgNPs have shown an enhanced antimicrobial activity than the Neo-chit as well as bare AgNP (Table 2).

TABLE 2. Antimicrobial activity of the Neo-chit and Neo-chit @ AgNPs against Gram positive and Gram negative bacteria

	Gram positive bacteria					**Gram negative bacteria**				
Sample (μg/ml)	***Staphylococcus aureus***					***Salmonella typhi***				
	a	**b**	**c**	**d**	**e**	**a**	**b**	**c**	**d**	**e**
Neo-chit	2.5	3	3.5	8	–	–	–	–	11	–
Neo-chit@AgNPs	3	6	8	14	–	4	6	9	24	–

4. Conclusion

We have synthesized neomycin antibiotic drug-functionalized chitosan by a Schiff base reaction using chitosan dialdehyde. The neomycin-functionalized chitosan was isolated in pure form by dialysis followed by freeze drying method. From the FT-IR result it is confirmed that neomycin aminoglucoside antibiotic drug molecules effective functionalized on chitosan backbone. The neomycin-functionalized chitosan was used further to stabilize the green synthesized silver nanoparticles using lemon juice as reducing agent. The antibacterial activity of the Neo-chit and Neo-chit@AgNP were tested. An enhanced antimicrobial activity was noted in the case of neo-chit-stabilized silver nanoparticles system than the neo-chit system and silver nanoparticles. The combined form of silver nanoparticles and Neo-Chit showed can be used to eradicate the microbial drug resistance organisms.

References

[1] Enxian Lu, Scott Franzblan, Carmen Popesu. Preparation of aminoglycoside-loaded chitosan nanoparticles using dextran sulphate as a counter ion. *J. Micro encapsulation: Micro and Nano carriers*, 2009, **26**(4), P. 346–354.

[2] Jayakumar R., Deepthy Menon, Manzoor K., Tamura H. Biomedical application of chitin and chitosan based nanomaterials. *Carbohydrate polymers*, 2010, **82**(2), P. 227–232.

[3] Chen J., Liu Q., Zhang X., Zhang Q. Prevaporation and characterization of chitosan membranes cross linked by 3-aminopropyltriethoxysilane. *J. Member. Sci*, 2007, **292**, P. 125–132.

[4] Ravi Kumar M.N.V. A review of chitin and chitosan applications. *Reactive and Functional Polymers*, 2000, **46**, P. 1–27.

[5] Vold I.M., Christensen B.E. Periodate oxidation of chitosans with different chemicalCompositions. *Carbohydr Res*, 2005, **340**, P. 679–684.

[6] Xin Liu, Yunhui. Preparation process and Antimicrobial Properties of cross-linking chitosan on to periodate-oxidised bamboo pulp fabric. *J. of Fibers and polymers*, 2014, **15**, P. 1887–1894.

[7] Jolanta kumirska, Mirko X., Weinhold, Jorg Thoming, Piotr Stepnowski. Biomedical Activity of Chitin/Chitosan Based Materials- Influence of properties Apart from Molecular Weight and Degree of N-Acetylation. *J. Polymer*, 2011, **3**, P. 1875–1901.

[8] Hilde K. Holme, Lene Davidsen, Are Kristiansena. Kinetics and mechanism of depolymerization of alginate and chitosan in aqueous solution. *Carbohydrate polymers*, 2007, **73**, P. 656–664.

[9] Tommeraas K., Varum K.M., Christensen B.E., Smidsrod O. Preparation and characterisation of oligosaccharides produced by nitrous acid depolymerisation of chitosans. *Carbohydr. Res*, 2001, **333**, P. 137–144.

[10] Lin C.W., Lin J.C. Characterization and blood coagulation evaluation of the water soluble chitooligosaccharides prepared by a facile fractionation method. *Biomacromolecules*, 2003, **4**, P. 1691–1697.

[11] Tian F., Liu Y., Hu K., Zhao B. Study of the depolymerization behavior of chitosan by hydrogen peroxide. *Carbohydr. Polym.*, 2004, **57**, P. 31–37.

[12] Yan Feng, Limin Yang, Feng Li. A novel sensing platform based on periodate-oxidized chitosan. *Anal. Methods*, (2010), **2**, P. 2011–2016.

[13] Jayakumar R., Divya Rani V.V., Shalumon K.T., Sudheesh Kumar P.T. Nair S.V., Furuike T., et al. Bioactive and osteoblast cell attachement studies of novel α-and β-chitinmembranes for tissue engineering applications. *Int. J. Biol Macromol*, 2009, **45**, P. 260–4.

[14] Jayakumar R., Prabaharan M., Reis R.L., Mano J.F. Graft copolymerized chitosan – present status and applications. *Carbohydr. Polym.*, 2005, **62**, P. 142–58.

[15] Prabaharan M., Mano J.F. Chitosan-based particles as controlled drug delivery systems. *Drug Deliv*, 2005, **12**, P. 41–57.

[16] Lin C.C., Anseth K.S. PEG hydrogels for the controlled release of biomolecules in regenerative medicine. *Pharm. Res*, 2009, **26**, P. 631–43.

[17] Mi F.L., Wu Y.B., Shyu S.S., Chao A.C., Lai J.Y., Su C.C. Asymmetric chitosan membranes prepared by dry/wet phase separation: a new type of wound dressing for controlled antibacterial release. *J. Membr Sci*, 2003, **212**, P. 237–54.

[18] Sharma V.K., Yangard R.A. Green Synthesis and their antimicrobial activities. *J. Colloid Interface. Sci*, 2009, **9**, P. 83–96.

[19] Kora A.J., Rastogi L. Enhancement of antibacterial activity of capped silver nanoparticles in combination with antibiotics, on model Gram-negative and Gram-positive bacteria. *Bioinorg. Chem. Appl*, 2013, P. 1–7.

NANOSYSTEMS: PHYSICS, CHEMISTRY, MATHEMATICS, 2016, 7 (4), P. 765–767

Surfactant assisted synthesis of nanocrystalline n-Bi_2Se_3 thin films at room temperature via arrested precipitation technique

N. D. Desai, S. M. Patil, K. V. Khot, R. M. Mane, P. N. Bhosale*

Materials Research Laboratory, Department of Chemistry, Shivaji University, Kolhapur–416004, India

*p_n_bhosale@rediffmail.com

PACS 81.07.-b **DOI 10.17586/2220-8054-2016-7-4-765-767**

In the present investigation, we have successfully synthesized nanocrystalline bismuth selenide (Bi_2Se_3) thin films using an arrested precipitation technique at room temperature. The optostructural, morphological, compositional and photoeletrochemical properties were studied for Bi_2Se_3 thin films prepared via surfactant-assisted synthesis. The optical study reveals the presence of direct allowed transition with band gap energy ranging from 1.40–1.80 eV. The X-ray diffraction (XRD) pattern confirms rhombohedral crystal structure. Scanning electron microscopy study shows the morphological transition from an interconnected mesh to nanosphere-like morphology and finally, lamellar sphere. Atomic force microscopy (AFM) study carried out to determine surface roughness and surface topography of thin films. Energy dispersive spectroscopy (EDS) analysis reveals the presence and ratio of elemental bismuth and selenium. Finally, the photoelectrochemical (PEC) performance of all the as-synthesized thin films were carried out using iodide-polyiodide redox couple.

Keywords: Bi_2Se_3, APT, surfactant.

Received: 16 April 2016

Revised: 22 April 2016

1. Introduction

Currently, there is significant research interest in the development of semiconducting materials for solar cell applications. Bi_2Se_3 is V-VI group binary chalcogenide which has been a material of interest for many years [1, 2]. The novel optostructural and morphological properties of Bi_2Se_3 are useful in numerous fields, such as thermoelectric devices, photosensitive devices, photovoltaic cells, Hall Effect magnetometer, refrigeration, high frequency power sensors, topographic insulator, etc [3–7].

Several methods have been developed to obtain nanostructured Bi_2Se_3 such as SILAR, MOCVD, CBD, Sputtering, Microwave assisted synthesis, etc. Among all these metods, APT is a simple, attractive and cost effective method. Hence, we have selected an APT method for deposition of Bi_2Se_3 thin films. There are very few reports available on the PEC performance of Bi_2Se_3 thin films. Hence, in the present article, we are reporting on the PEC performance for Bi_2Se_3 thin films prepared by a surfactant-assisted APT protocol.

2. Experimental

Nanocrystalline Bi_2Se_3 thin films have been synthesized via an arrested precipitation technique (APT) at room temperature. 0.05 M bismuth triethanolamine complex (Bi-TEA) and 0.25 M sodium selenosulphite (Na_2SeSO_3) were used as precursor solution for Bi and Se respectively. TEA was used as a complexing agent. In a typical synthesis, both precursor solutions were added in a 2:3 ratio. The pH was adjusted to 10. The pre-cleaned glass substrate was placed vertically in the reaction bath. The total volume of reaction bath was made 40 mL by addition of double distilled water (D/W). The reaction bath is maintained at room temperature without disturbing for 8 hrs. When the terminal growth stops, thin films were taken out and washed 2–3 times with D/W. Thin films were dried at room temperature and used for further characterization.

3. Optical study

The thicknesses of Bi_2Se_3 were measured using a surface profilometer. The thickness was found in the range of 630 nm to 910 nm.

The UV-Visible spectrum of as-deposited Bi_2Se_3 thin film was recorded for wavelengths ranging from 500–1100 nm, as shown in Fig. 1(a). In order to determine the band gap of Bi_2Se_3 thin films, the classical absorption equation is used:

$$\alpha h\nu = A(h\nu - E_g)^n. \tag{1}$$

The optical band gap was found to be 1.7 eV with directly-allowed transition, as shown in Fig. 1(b)

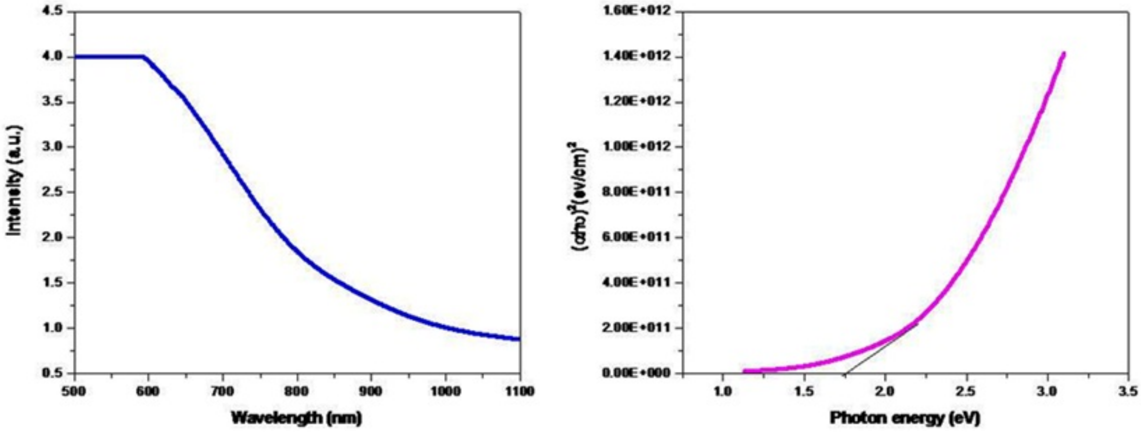

FIG. 1. (a) Optical absorption spectrum of Bi_2Se_3 thin films (b) Plot of $(\alpha h\nu)^2$ vs. $h\nu$

4. Structural study

The phase determination of as-deposited Bi_2Se_3 thin film was done using XRD. All peaks in the XRD pattern are well matched with rhombohedral crystal structure (JCPDS 33-021). The most intense peak is observed at 29.33° for (015) plane. The crystallite size is calculated by the Debye-Sheerer equation.

$$D = 0.9\lambda/\beta\cos\theta. \tag{2}$$

The crystallite size is found to be 47.89 nm.

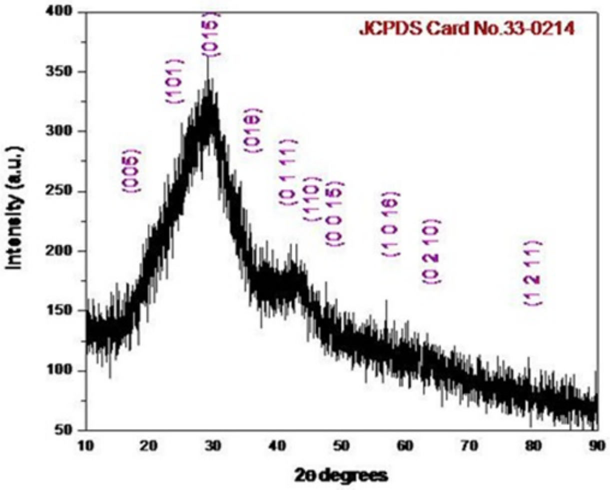

FIG. 2. XRD Patterns of Bi_2Se_3 thin films

5. Morphological and compositional study

The SEM image indicates a uniform, well-adherent and pinhole-free deposition for the Bi_2Se_3 thin film. The SEM micrograph shows an interconnected mesh-like structure.

In order to determine the chemical composition of Bi_2Se_3 thin films, EDS analysis was also carried out. The presence of Bi^{3+} and Se^{2-} was confirmed from EDS. The expected and observed atomic percentages of Bi and Se are in good agreement with standard data. The excess percentage of bismuth is most likely due to an antisite defect. Antisite defects means that excess Bi enters the lattice by replacing Se. The higher percentage of Bi may also attributed to the more metallic character of Bi and its high reactivity towards Se. The small difference in the electronegativity between Bi and Se is also responsible for antisite defect.

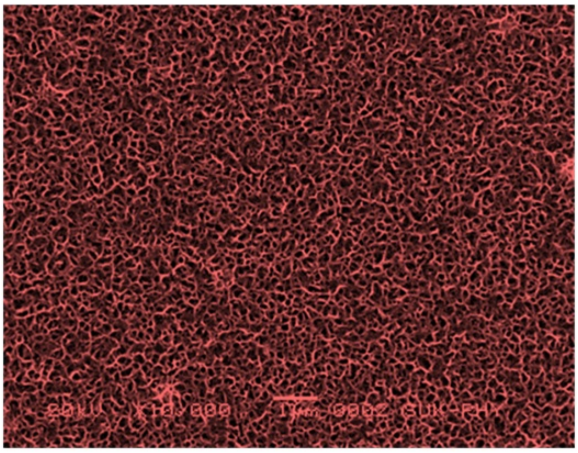

FIG. 3. SEM images of Bi_2Se_3

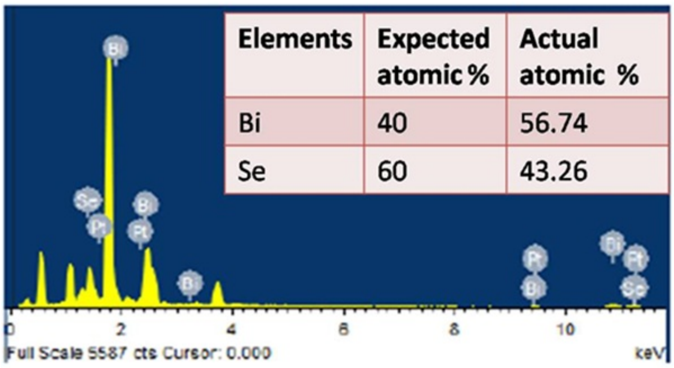

Elements	Expected atomic %	Actual atomic %
Bi	40	56.74
Se	60	43.26

FIG. 4. EDS pattern of Bi_2Se_3 thin films

6. Conclusion

Bi_2Se_3 thin films were synthesized via simple and low cost APT. The optostructural and morphological properties were studied to a film prepared using a surfactant-assisted protocol. The XRD pattern confirmed rhombohedral crystal structure. The SEM pattern revealed an inetrconnected mesh-like structure. The EDS pattern determined the stoichiometric ratio for Bi and Se in the thin film formation.

All these results showed that Bi_2Se_3 thin films may be useful for solar cell application.

References

[1] Osterloh F.E. Inorganic nanostructures for photoelectrochemical and photocatalytic water splitting. *Chem. Soc. Rev.*, 2013, **42**, P. 2294–2320.

[2] Yang J., Li Y., Liu F., Jiang L., Ye J., Liu Y. The electrochemical self assembly of hierarchical dendritic Bi_2Se_3 nanostructures. *Cryst. Eng. Comm.*, 2014, **16**, P. 2823–2834.

[3] Jagminas A., Valiunas I., Vernese G.P., Juskenas R., Rutavicius A. Alumina template assisted growth of bismuth selenide nanowire arrays. *J. Cryst. Growth*, 2008, **310**, P. 428–433.

[4] Xiao F., Hangarter C., Yoo B., Rheem Y., Lee K., Myung N.V. Recent progress in electrodeposition of thermoelectric thin films and nanostructures. *Electrochim. Acta*, 2008, **53**, P. 8103–8117.

[5] Xiao C., Li Z., Li K., Huang P., Xie Y. Decoupling Interrelated Parameters for Designing High Performance Thermoelectric Materials. *Acc. Chem. Res.*, 2014, **47**, P. 1287–1295.

[6] Ko J., Kim J., Choi S., Lim Y., Seo W., Lee K. Nanograined thermoelectric $Bi_2Te_{2.7}Se_{0.3}$ with ultralow phonon transport prepared from chemically exfoliated nanoplatelets. *J. Mater. Chem.*, 2013, **1**, P. 12791–12796.

[7] Borisova S., Krumrain J., Luysberg M., Mussler G., Gruitzmacher D. Mode of Growth of Ultrathin Topological Insulator Bi_2Te_3 Films on Si (111) Substrates. *Cryst. Growth Des.* 2012, **12**, P. 6098–6103.

NANOSYSTEMS: PHYSICS, CHEMISTRY, MATHEMATICS, 2016, 7 (4), P. 768–773

Antibacterial and catalytic properties of silver nanoparticles loaded zeolite: green method for synthesis of silver nanoparticles using lemon juice as reducing agent

J. Selvamuthumari[1], S. Meenakshi[2], M. Ganesan[1], S. Nagaraj[3], K. Pandian[2,*]

[1]Department of Chemistry, Thiagarajar College, Madurai–625009, India

[2]Department of Inorganic Chemistry, University of Madras, Guindy Campus, Chennai–600025, India

[3]CAS Botany, University of Madras, Guindy Campus, Chennai–600025, India

*jeevapandian@yahoo.co.uk

PACS 82.65.+r **DOI 10.17586/2220-8054-2016-7-4-768-773**

Zeolite Y is a cage-like alumina silicate which is widely used as solid support to immobilize metal and metal sulfide nanoclusters. We have attempted to synthesis silver nanoparticle-loaded zeolite Y by an ion exchange method followed by a biogenic reduction method using lemon juice as a reducing agent. The antimicrobial activity of the silver ion, silver nanoparticles and silver chloride-modified zeolite was investigated against various Gram negative and Gram positive microorganisms. The silver nanoparticle-loaded zeolite was further functionalized with amoxicillin antibiotic which exhibited a strong antimicrobial action to kill drug resistant microorganisms. The catalytic behavior of silver nanoparticles was investigated to reduce 4-Nitrophenol in presence of $NaBH_4$. The catalytic reaction is found to be pseudo-first order, resulting in a rate constant that was comparable with previously-reported results.

Keywords: zeolite-Y, silver nanoparticles, amoxicillin, catalytic reduction of 4-aminophenol, antibacterial studies.

Received: 3 May 2016

Revised: 25 June 2016

1. Introduction

Zeolites are an important group of crystalline aluminosilicates currently available for various fields of applications. These minerals are widely used as sorbents, ion exchangers, catalysts and biosensors [1–4]. The catalytic nature, reactivity and other properties of zeolite can be greatly improved by cation exchange methods [5]. These materials are negatively charged with a high density of active acid sites, high thermal stability, high size selectivity and unique porous properties, which impart their ability act as catalysts for various industrial catalytic studies at elevated temperature with wider pH ranges. Because of void space and swelling behavior which can be used in petrochemical cracking, ion-exchange, gas and solvent separation, and removal of pollutants [6]. Metal ion, charged species, redox and photoactive molecules can be immobilized within the pores of zeolite system and these composites can be used in sensors and catalytic applications [7–10].

Silver (Ag) is a metallic element that has been widely used in various excellent fields [11]. Silver ions (Ag^+) and silver nanoparticles are effective in inhibiting bacterial growth and may damage the DNA of both Gram-positive and Gram-negative bacteria [12–15]. Silver modified zeolite has been used in various fields such as catalyst, biosensors, water purification, antifungal and antimicrobial activity [16, 17].

The aim of this study is to prepare AgNPs/Zeo-Y nanocomposites using lemon juice as reducing agent by green synthesis method and study of its applications in the catalytic reduction of 4-Nitrophenol and the antibacterial activity of the system.

2. Experimental Section

2.1. Chemicals

Zeolite-Y and silver nitrate were purchased from Sigma Aldrich, USA. 4-Nitrophenol and liquid ammonia (30% v/v) were received from Fisher Scientific Pvt. Ltd., India. Sodium borohydrate, sodium chloride and amoxicillin were received from Merck, India. Hydrochloric acid and sulphuric acid were purchased from SRL Pvt. Ltd., India. All reagents and chemicals were used received from commercial source with an analytical grade and without further purification.

2.2. Preparation of AgNPs/Zeo-Y

To prepare AgNPs/Zeo-Y nanocomposite, 0.1 M $AgNO_3$ was dissolved in 20 mL of distilled water and then 1 % solution of NH_4OH was added dropwise to the aq. solution of $AgNO_3$ [18]. The color of the solution changed from greenish gray to colorless. 1 g of natural zeolite-Y was added to above mixture and stirred overnight. The product was collected and washed with distilled water and then dried at 100 °C for 2 h. Finally, the AgNPs/Zeo-Y nanocomposite was collected for further studies.

2.3. Synthesis of AgCl/ Zeo-Y

The Ag^+ ion loaded Zeo-Y was placed in a sealed 100 ml round bottom flask and then purged with HCl gas which was generated from NaCl in presence of conc.H_2SO_4 continuously to obtain AgCl immobilized Zeo-Y for a period of 2 h.

2.4. Preparation of AgNPs/Zeo-Y using lemon juice as reducing agent

To 3 mL of DD water was added a fresh 1 mL of lemon juice and the pH of the medium was adjusted to 11 followed by 0.01 M of silver nitrate solution was added. Finally, the yellowish green colored solution was changed to reddish brown color which indicated the formation of silver nanoparticle immobilized zeolites.

2.5. Preparation of Amoxicillin modified AgNPs/Zeo-Y

A known amount of AgNPs/Zeo-Y was dispersed an aqueous solution of 0.01M amoxicillin and then allowed stand for 1 h to obtain amoxicillin protected AgNPs/Zeo-Y. The final product was obtained by centrifugation.

2.6. Instrumentation

UV-Visible spectral studies were carried out using Shimadzu UV-Visible Spectrophotometer, Japan (Model UV-1800). The XRD patterns with diffraction intensity versus 2 θ were recorded in a JSO Debye Flex 2002 Seifert diffractometer using Cu Kα radiation (λ=1.5406 Å) from 10 to 80° at a scanning speed of 1° min^{-1}. X-ray tube voltage and current were set at 40 kV and 40 mA, respectively. Morphological and structural investigations were carried out using field emission scanning electron microscopy (FE-SEM, SU6600, Hitachi, Japan).

2.7. Antibacterial test

To evaluate the antibacterial properties of AgNPs/Zeo-Y and amoxicillin modified AgNPs/Zeo-Y, *Bacillus subtilis* and *Salmonella typhi* were selected as Gram-negative and Gram-positive bacteria, respectively. One has the ability to measure the effectiveness of an antibacterial agent by determining a zone of inhibition. A standard inoculum of the test organism with 1×10^7 colony forming units (CFU)/mL was swabbed onto the surface of a LB agar plate, AgNPs/Zeo-Y and Amoxicillin/AgNPs/Zeo-Y antibacterial agents were placed on the surface of agar. The plates were incubated overnight at 37°C, and the clear zones around the antibacterial agents were then measured. The above experiments were repeated thrice and the average values were taken.

3. Results and discussion

3.1. Characterization of AgNPs loaded Zeolite Y

The UV-Visible spectra of a) AgNPs/Zeo-Y, b) lemon juice, c) amoxicillin and d) AgNPs/Zeo-Y with amoxicillin are shown in Fig. 1. The silver nanoparticles loaded zeolite Y nanocomposite shows a silver nanoparticle peak at 420 nm due to surface plasmon resonance (SPR). The lemon juice not showing any peak and the amoxicillin peak was obtained at 270 nm. After the incorporation of amoxicillin drug into the silver nanoparticles loaded zeolite Y nanocomposite two major peaks were observed one at 360 nm and another one at 250 nm. Thus, these results confirm that amoxicillin drug was effectively attached to the silver nanoparticles loaded zeolite Y nanocomposite through ionic interaction.

The X-ray diffraction pattern of a) zeolite-Y and b) AgNps/Zeo-Y nanocomposite are shown in Fig. 2. As shown in Zeo-Y, the peaks at 31.04, 32.74, 33.24, 34.34, 35.94, 36.64, 37.76, 40.24, 41.74, 41.92, 52.80, 54.48, 56.54, 57.58, 58.74, 65.22, 66.54, 69.34, 71.10, 72.92, 75.96, and 77.82° are assigned for the presence of zeolite (JCPDS: 01-072-2344) [19]. In AgNPs/Zeo-Y, the characteristics peaks are due to the presence of silver chloride are attributed at 27.6, 32.05, 46.05, 54.6, 57.3, 67.4, 74.5 and 76.6° with plane of 111, 200, 220, 311, 222, 400, 311 and 420 reflections owing to the AgCl phase. These results confirm that the silver nanoparticles loaded within zeolite Y matrix.

The structural and morphology were confirms by FE-SEM images. The mesoporous material of zeolite has octahedral shaped particles with various sizes around 1 μm (Fig. 3(a)) [20]. From AgNPs loaded zeolite Y, the

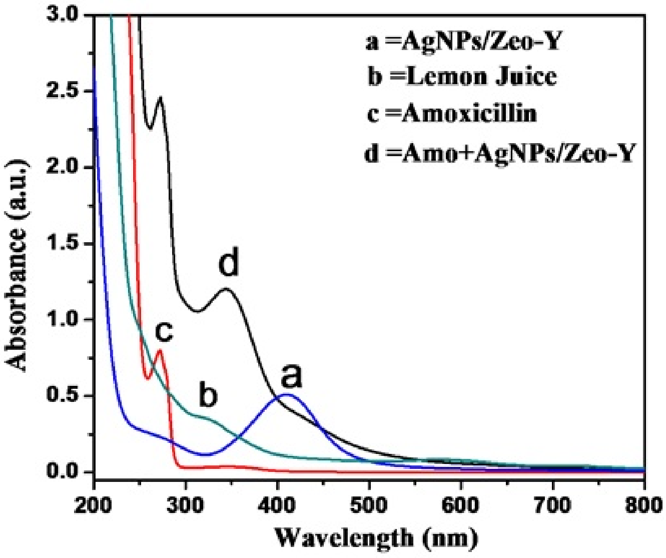

FIG. 1. UV-Visible spectrum of a) AgNPs/Zeo-Y, b) lemon, c) amoxicillin and d) AgNPs/Zeo-Y with amoxicillin

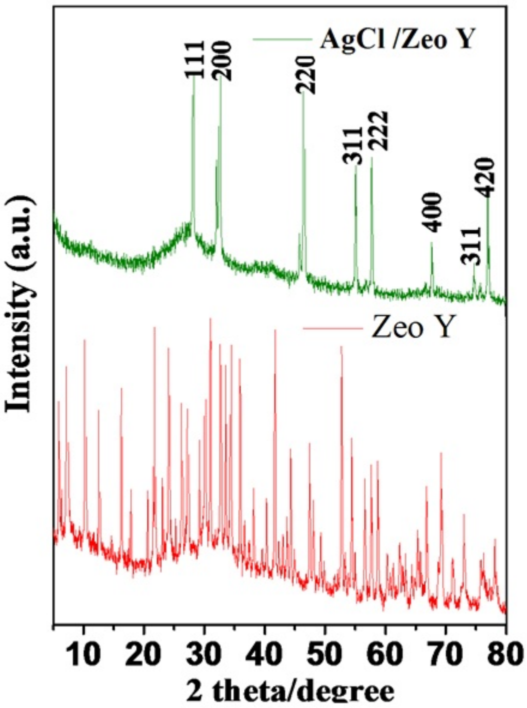

FIG. 2. XRD analysis a) zeolite Y and b) AgNPs loaded Zeo-Y

silver nanoparticles loaded on surface of mesoporous zeolite and also regular shaped silver nanoparticles and the size of the silver nanoparticles are roughly 0.1 μm as shown in Fig. 3(b). Therefore, the present method can be exploited for the effective loading of silver nanoparticles on zeolite surface.

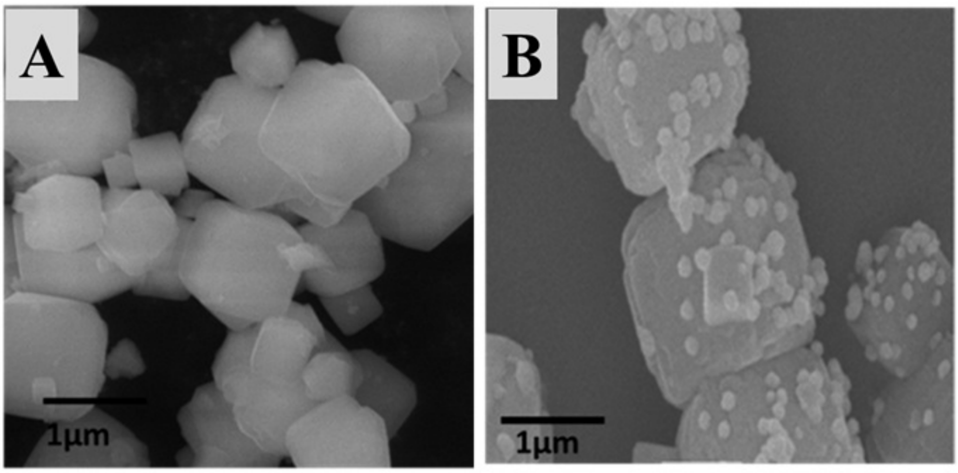

FIG. 3. FE-SEM images for Zeolite-Y (A) and AgNPs/Zeo-Y (B)

3.2. Catalytic activity of Zeolite Y loaded AgNPs

The catalytic activity of AgNPs/Zeo-Y was tested against the catalytic reduction of 4-Nitrophenol (4-NP) in the presence of $NaBH_4$. Upon the addition of $NaBH_4$ (Fig. 4(a)), the absorption peak of 4-Nitrophenol undergoes an immediate red-shift from 317 nm to 400 nm indicating the formation of 4-Nitrophenolate ions, evidenced by the visible color changes from light yellow to yellow green in color. After the addition of AgNPs/Zeo-Y using lemon juice nanocomposite, the absorption peak at 400 nm gradually decreased in intensity along with increase in absorption of a new peak at 300 nm, indicating the formation of 4-Aminophenol (4-AP). Under these reaction conditions, the reduction was completed within 10 and 5 mins for the addition catalytic amount 5 mg and 10 mg respectively (Fig. 4(b) and Fig. 4(c)).

The rate of reaction forb the reduction of 4-NP in presence of the AgNPs/Zeo-Y nanocomposite is due to decrease in absorbance values at 400 nm. Therefore, the rate constant of the reaction can be calculated using the following formula:

$$\ln C/C_0 = -kt, \tag{1}$$

where k is the constant, t is the reaction time; C and C_0 are the concentration of 4-NP at time t and 0, respectively. The concentration or borohydride used in the entire study was 0.1 M, which is large excess when compared to the concentration of 4-NP, thus the reduction reaction is considered to be pseudo first order so that the rate of the reaction depends primarily on the concentration of 4-NP. The rate of the reaction (k) obtained from the slope of the straight line was found to be 0.083 min^{-1} and 0.32 min^{-1} for 5 and 10 mg of catalyst used for the catalytic studies (Fig. 4(d)). The rate of the reaction increases with increasing of the catalyst concentration which is due to the increase of the catalytic activities.

3.3. Antibacterial activity

It is well established that silver nanoparticles modified substrates have shown an enhanced antimicrobial activity [12, 13]. In the present study, we studied the antimicrobial activity of silver nanoparticles, AgNPs/Zeo-Y and amoxicillin incorporated AgNPs/Zeo-Y against various Gram negative and Gram positive bacteria. Obviously, amoxicillin modified AgNPs/Zeo-Y showed a good antimicrobial activity against *Bacillus subtilis* and *Salmonella typhi.* The antimicrobial activity of AgNPs/Zeo-Y and Amoxicillin/AgNPs/Zeo-Y against various Gram positive and Gram negative bacteria as shown in Table 1.

4. Conclusion

In summary, the biogenic method was established to synthesize silver nanoparticle-loaded zeolite Y through an ion exchange approach followed green chemical reduction using lemon juice. This method is a fast and easy way to synthesize the AgNPs/Zeo-Y in large scale. The activity of AgNPs/Zeo-Y was studied, displaying excellent

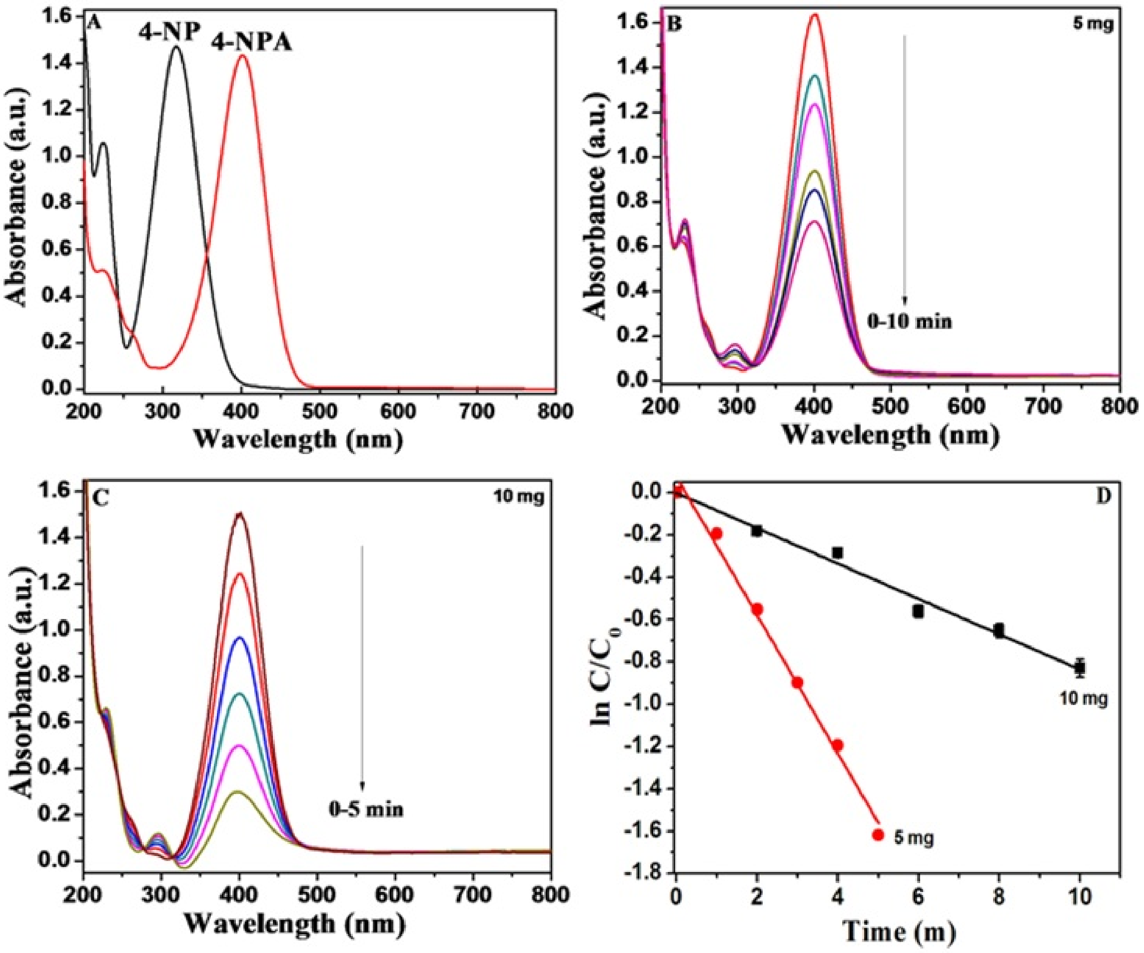

FIG. 4. UV-Visible spectra capturing the conversion of 4-NP to 4-AP upon reaction with $NaBH_4$(A), in presence of 5 mg and 10 mg of AgNPs/Zeo-Y (B), (C) and kinetic plot. Error bars designates the standard deviation for five independent measurements (D)

TABLE 1. Antibacterial activity of AgNPs/Zeo-Y and Amoxicillin/AgNPs/Zeo-Y against *Bacillus subtilis* and *Salmonella typhi*

Sample (mg/mL)	**Gram Positive Bacteria**					**Gram Negative Bacteria**				
	Bacillus subtilis					***Salmonella typhi***				
	a	**b**	**c**	**d**	**e**	**a**	**b**	**c**	**d**	**e**
AgNPs/Zeo-Y	2.2	6.5	7.3	16.4	-	3.3	6.5	8.4	20.5	-
Amoxicillin AgNPs/Zeo-Y	-	3.1	3.5	7.5	-	-	-	-	9.4	-

a = (25 μg/ml), b = (50 μg/ml), c = (75 μg/ml), d = (25 μg/ml (Standard) chloramphenicol), e = 50 μg/ml 0.1 % DMSO catalytic activity for the conversion of 4-NP to 4-AP. The amoxicillin-protected AgNPs/Zeo-Y system can be exhibited an enhanced antimicrobial activity as compared to AgNPs/Zeo-Y.

Acknowledgement

The authors (Dr. K. P. and S. M.) is grateful the UGC-CPEPA for providing partial financial assistance to carry out a part of this work.

References

[1] Bandura L., Franus M., Jozefaciuk G., Franus W. Synthetic zeolites from fly ash as effective mineral sorbents for land-based petroleum spills cleanup. *Fuel*, 2015, **147**, P. 100–107.

[2] Rees L.V.C., Zuyi T. Rare-earth ion exchange in zeolite Y. *Zeolites*, 1986, **6**, P. 201–205.

[3] Yu J., Xiao F., Corma A. Preface to special issue on zeolite materials and catalysis. *Chinese Journals of Catalysis*, 2015, **36**, P. 787–788.

[4] Serban S., Murr N.E. Synergetic effect for NADH oxidation of ferrocene and zeolite in modified carbon paste electrodes: New approach for dehydrogenase based biosensors. *Biosensors and Bioelectronics*, 2004, **20**, P. 161–166.

[5] Onyango M.S., Kojima Y., Aoyi O., Bernardo E.C., Matsuda H. Adsorption equilibrium modeling and solution chemistry dependence of fluoride removal from water by trivalent-cation-exchanged zeolite F-9. *Journal of Colloid and Interface Science*, 2004, **279**, P. 341–350.

[6] Banerjee R., Furukawa H., Britt D., Knobler C., Keeffe M.O., Yaghi O.M. Control of pore size and functionality I isoreticular zeolitic imidazolate frameworks and their carbon dioxide selective capture properties. *J. Am. Chem. Soc.*, 2009, **131**, P. 3875–3877.

[7] Zhang Y., Yu X., Wang X., Shan W., Yang P., Tang Y. Zeolite nanoparticles with immobilized metal ions:isolation and MALDI-TOF-MS/MS identification of phosphopeptides. *Chem. Commun.*, 2004, **25**, P. 2882–2883.

[8] Mitsuo Y. Immobilization of toxic heavy metals using hydrotalcite minerals: possible applications for decontamination of polluted land and water. *Journal of Ecotechnology Research*, 2002, **8**, P. 248–249.

[9] Kharlamov V.V., Minachev K.M., Gulyaeva L.P., Slyunadev P.I. The investigation of redox properties of palladium-zeolite catalysts. *Russian Chemical Bulletin*, 1995, **44**, P. 621–623.

[10] Peter A., Cozmuta L.M., Cozmuta A.M., Nicula C. Photocatalytic efficiency of zeolite-based TiO_2 composites for reduction of Cu (II): Kinetic models. *Int. J. Appl. Ceram. Technol.*, 2014, **11**, P. 568–581.

[11] Guzman M., Dille J., Godet S. Synthesis and antibacterial activity of silver nanoparticles against gram-positive and gram-negative bacteria. *Nanomedicine: Nanotechnology, Biology and Medicine*, 2012, **8**, P. 37–45.

[12] Castanon G.A.M., Martinez N.N., Gutierrez F.M., Mendoza J.R., Ruiz F. Synthesis and antibacterial activity of silver nanoparticals with different sizes. *J. Nanopart Res*, 2008, **10**, P. 1343–1348.

[13] Rai M., Yadav A., Gade A. Silver nanoparticals as a new generation of antimicrobials. *Biotechn. Adv.*, 2009, **27**, P. 76–83.

[14] Xie W.R.L.X.B., Shi Q.S., Zeng H.Y., Yang Y.S.O., Chen Y.B. Antibacterial activity and mechanism of silver nanoparticles on Escherichia coli. *Appl. Microbial Biotechol*, 2010, **85**, P. 1115–1122.

[15] Baker C., Pradhan A., Pakstis L., Darrin J. Pochan, Shah S. Ismat. Synthesis and antibacterial properties of silver nanoparticles. *J. Nanosci. Nanotech.*, 2005, **5**, P. 244–249.

[16] Garza M.R., Olguin M.T., Sosa I.G., Alcantara D., Fuentes G.R. Silver supported on natural Mexican zeolite as an antibacterial material. *Microporous and Mesoporous Materials*, 2000, **39**, P. 431–444.

[17] Kaur B., Srivastava R., Satpati B. Silver nanoparticle decorated polyaniline zeolite nanocompoite material based non-enzymatic electrochemical sensor for nanomolar detection of lindane. *RSC Adv.*, 2015, **5**, P. 57657–57665.

[18] Meenakshi S., Devi S., PAndian K., Devendiran R., Selvaraj M. Sunlight assisted synthesis of silver nanoparticles in zeolite matrix and study of its application on electrochemical detection of dopamine and uric acid in urine samples. *Mat. Sci. Eng. C*, 2016, **69**, P. 85–94.

[19] Shameli K., Ahmad M.B., Zargar M., Yunus W.M.Z.W., Ibrahim N.A. Fabrication of silver nanparticles doped in the zeolite framework and antibacterial activity. *Int. J. Nanomed.*, 2011, **6**, P. 331–341.

[20] Reddy V.R., Currao A., Calzaferri G., Zeolite A., Zeolite L. Monolayers modified with AgCl as photocatalyst for water oxidation to O_2. *J. Mater. Chem.*, 2007, **17**, P. 3606–3609.

NANOSYSTEMS: PHYSICS, CHEMISTRY, MATHEMATICS, 2016, 7 (4), P. 774–779

In-situ functionalization of aniline oligomer onto layered graphene sheet and study of its application on electrochemical detection of ascorbic acidin food samples

S. Devasena[1], S. Meenakshi[2], R. Sayeekannan[1], K. Pandian[2,*]

[1]Department of Chemistry, Thiagarajar College, Madurai–625009, India

[2]Department of Inorganic Chemistry, University of Madras, Guindy, Chennai–600025, India

*jeevapandian@yahoo.co.uk

PACS 82.47.Rs **DOI 10.17586/2220-8054-2016-7-4-774-779**

Aniline oligomers are considered as one of the electron transfer mediators for the electrochemical oxidation of ascorbic acid. The electrochemical oxidation of ascorbic acid was investigated using aniline oligomer-functionalized polymer modified electrode. In the present investigation, we demonstrated a novel methodology for the in-situ modification of aniline oligomer onto the layered graphene sheet by using diazonium salt form as precursor molecule. An enhanced electrocatalytic current was obtained for the oxidation of ascorbic acid using aniline pentamer-functionalized reduced graphene oxide (AP-rGO). Detailed studies have been carried out to study the surface modified rGO by FTIR spectroscopy. A linear relationship between peak current against the concentration of ascorbic acid was observed within the ranges from 1 μM to 10 μM. The detection limit was measured at signal/noise (S/N) of 3. The present method can be utilized for the electrochemical detection of ascorbic acid present in food products like fruit juices.

Keywords: graphene oxide, pentamer, voltammetric method, ascorbic acid, food samples.

Received: 3 May 2016

Revised: 25 June 2016

1. Introduction

Ascorbic acid is one of most important biological compounds involved in various human metabolisms. It is used to ameliorate a number of illnesses, such as the scurvy, common cold, cancer and AIDS [1]. Moreover it is present in fresh fruits, vegetables and also available in pharmaceutical products and foodstuffs as an oxidant as well as stabilizer. Thus, the development of inexpensive and easy methods for the determination of ascorbic acid is particularly important in the pharmaceutical and food industries. There are several reported methods for the detection of ascorbic acid in foodstuffs, such as chromatography [2], spectrophotometry [3], capillary electrophoresis [4] and most recently, electrochemical methods [5–7].

The amperometric determination of ascorbic acid is based on its electrochemical oxidation, which occurs at high potential at carbon or metal electrodes, however, fouling by oxidation products leads to poor reproducibility [8]. Numerous attempts to decrease the high working electrode potential and improve reproducibility have been made by modifying the electrode surface with various active mediators for the electrochemical oxidation of ascorbic acid. Attempts have been made to develop a chemically-modified electrode with various redox mediators like 7,7,8,8-tetracyanoquinodimethane, osmium 2,2-bipyridyl poly-4-vinyl pyridine chloride complex, lanthanum 2,6-dichlorophenolindophenol, manganese dioxide and a cobalt (II) phthalocyanine and Prussian blue was also used to oxidize ascorbic acid [9, 10]. The electrocatalytic oxidation of ascorbic acid on conducting polymer modified electrodes, in particular on polyaniline, has also been studied. Recently, aniline oligomer-functionalized polymers have been used for the electrochemical oxidation of ascorbic acid has been developed that has both a low applied operating potential and a low detection limit.

In the present investigation, we demonstrated the preparation of an aniline oligomer-modified graphene oxide based on chemical reductive binding of diazonium salt form of aniline oligomer in presence of graphene oxide. The electrocatalytic behavior of an aniline oligomer-functionalized graphene oxide-modified glassy carbon electrode was tested against the electrochemical oxidation of ascorbic acid in phosphate buffer solution. The greater sensitivity and low detection limits were achieved by the differential pulse voltammetry method. Thus, the present method can be considered as an efficient one for electrochemical detection of ascorbic acid in food products.

2. Experimental Section

2.1. Chemicals

Graphite powder, Ascorbic acid and N, N-diphenylamine were received from Sigma Aldrich, USA. Ammonium hydroxide and sodium nitrite were purchased from Fisher Scientific Pvt. Ltd. India. DMF, HCl, H_2SO_4 and ethanol were received from SRL Pvt. Ltd. India. Ethanol and $KMnO_4$ were procured from Merck, India. All reagents and chemicals were used an analytical grade and without further purification.

2.2. Preparation of pentamer

2.28 g amino capped aniline trimer and 3.04 g N, N-diphenylamine were dissolved with 80 mL of DMF. 20 mL of water and 10 mL of 36 % of HCl were then added to the above solution with vigorous stirring at 4 hrs for room temperature. The HCl-doped aniline pentamer was obtained by filtration and then washed by a mixture of DMF/water. The product was doped in 100 mL of 1 ML^{-1} ammonium hydroxide for 30 m to produce aniline pentamer in emeraldine state. The emeraldine aniline pentamer was reduced by phenylhydrazine and was precipitated in a H_2O/ethanol mixture. The leucomeraldine aniline pentamer was collected by filtration and washed thoroughly with H_2O/ethanol mixture. The product was finally dried in vaccum oven.

2.3. Preparation of graphene oxide

20 g of graphite powder stirred with 500 mL of conc. H_2SO_4 in 1L beaker for 30 min. Then, 60 g of $KMnO_4$ was gradually added to this solution (added 20 g/30 minutes). The solution was then stirred for an additional 5 to 8 h and then added one l L water (900 mL) to the above mixture. Then, the reaction was terminated by addition of 50 mL H_2O_2 solution. Repeated centrifugation was done by using 5 % HCl aqueous solution followed by washed with deionized water until the pH of the solution reaches neutral. Then 160 mL of water was added resulting in the formation of precipitate. A uniform suspension of grapheme oxide (GO) nanoparticles was obtained after sonication [11].

2.4. Preparation of AP-rGO

The modification of GO was accomplished by dispersing GO (10 mg) in DI water (5 mL) to which aniline pentamer (10 mg) in 2 mL water was added. After complete dispersion of the reagent 0.011 g sodium nitrite in 1 ml of conc. HCl was added drop wise. The mixture was stirred for 4 h and then filtered, washed successively with deionized water followed by methanol. Finally, the powdered form of the product was isolated and then dried under nitrogen atmosphere in overnight.

2.5. Instrumentation

FTIR spectrum was recorded in the range of 400 to 4000 cm^{-1} FTIR spectrum was collected against the background spectrum of KBr. The cyclic voltammetric experiment was carried out using CHI 660A electrochemical instrument, USA and Gamry model 330, USA. A conventional three electrode system comprising of glassy carbon electrode (GCE) of 3 mm of geometrical surface area was purchased from BAS. Pvt. Ltd., USA. The Ag/AgCl and platinum wire were used as a reference electrode and counter electrode, respectively. The working electrode was polished using Bioanalytical system (BAS, USA) polishing kit.

3. Results and discussion

3.1. Characterization of AP-rGO

The FTIR spectrum of pentamer and AP-rGO are shown in Fig. 1. The absorption of aniline pentamer showed main bands at 1590 cm^{-1} and 1485 cm^{-1} assigned to the absorption of benzene ring and the quinoid ring. The 1273 cm^{-1} band was attributed to C-N stretching in the proximity of quinoid rings as shown in Fig. 1 [12]. After modification of AP-rGO, the benzenoid and quinoid peaks are bounded in the surface of graphene oxide. So these results confirm that the pentamer modified on graphene oxide surface.

The electrochemical behavior of AP-rGO was studied and the resulting cyclic voltammetry responses are shown in Fig. 2. As seen from Fig. 2(A), the typical cyclic voltammogram of AP-rGO in presence of 0.1 M H_2SO_4. With increase of scan rate the electrocatalytic oxidation peak current also increased gradually in the range from 5–100 mV/s. A linear relationship exists between peak current (I_p) versus scan rate (ν) and a linear regression equation of $y = 0.406 - 5.685$ with correlation coefficient (R^2) of 0.9959 as shown in Fig. 2(B), which illustrates a reversible electron transfer process with adsorption controlled one.

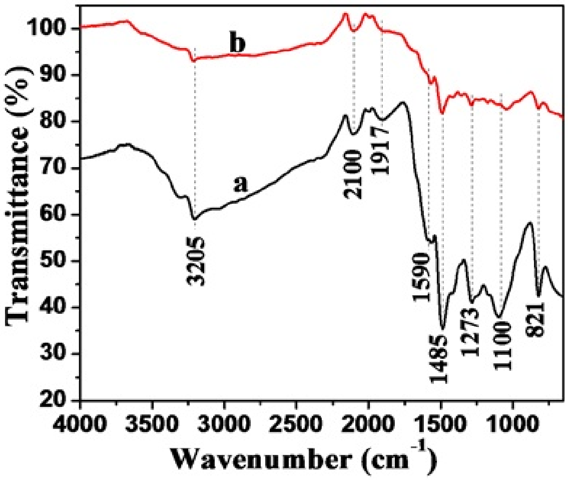

FIG. 1. FTIR spectrum of a) pentamer and b) AP-rGO

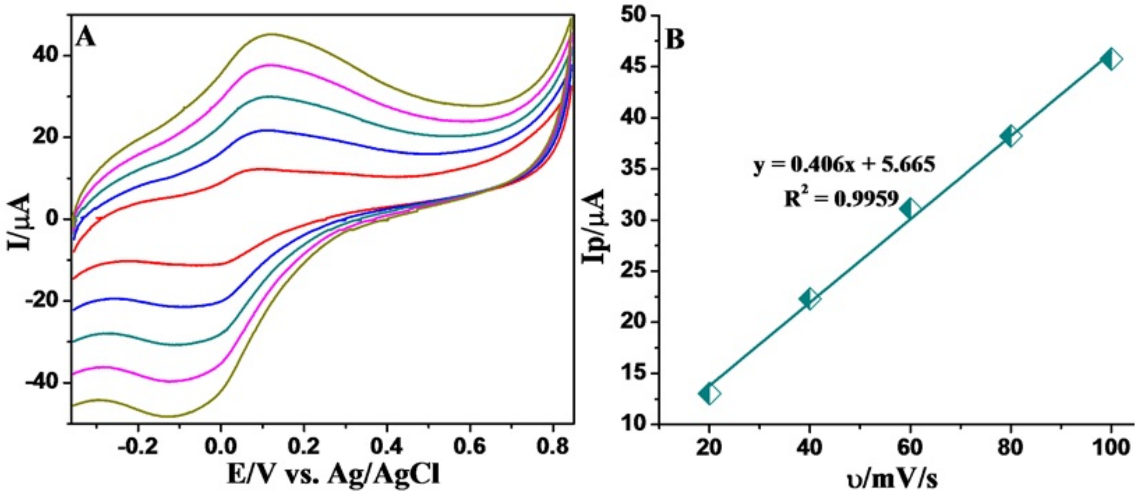

FIG. 2. A) CV of AP-rGO modified GCE at different scan rates (5-100 mV/s) in presence of 0.1 M H_2SO_4. B) Linear plot of Ip vs. υ

3.2. Electrochemical oxidation of ascorbic acid

The electrochemical behaviors of a) bare, b) bare-with ascorbic acid and c) AP-rGO modified GCE in presence of AA are shown in Fig. 3.(A) poor anodic current response was observed for the AA oxidation on bare GCE where as a well define oxidation peak was observed at +0.05 V (vs. Ag/AgCl) in the case of AP-rGO modified GCE.

The electrochemical behavior of AP-rGO/GCE at different concentrations of ascorbic acid (1×10^{-4} – 7×10^{-4} M) were investigated in 0.1 M pH 7.0 PBS by cyclic voltammetry (CV). As can be seen in Fig. 4(A), the AP-rGO/GCE after addition of AA to the buffer solution, an irreversible oxidation peak was observed at a scan rate of 50 mV/s with a anodic oxidation peak potential of +0.05 V (vs. Ag/AgCl). In Fig. 4(B) shows a linear regression equation of $y = 0.092x - 0.14$ with correlation coefficient is 0.9994.

The influence of peak potential scan rate against the electrochemical oxidation of ascorbic acid was investigated using AP-rGO/GCE in presence of 1mM of ascorbic acid at 0.1 M PBS (pH 7) with various scan rates as shown in Fig. 4(C). From AP-rGO modified GCE, the oxidation peak current of AA was increased by increasing the scan rates (10–120 mV/s) and linearity was observed by plotting the peak current values versus the square of scan rates with correlation coefficient of 0.9920 (Fig. 4(D)), suggesting that the electrochemical oxidation of AA is diffusion controlled electron transfer process.

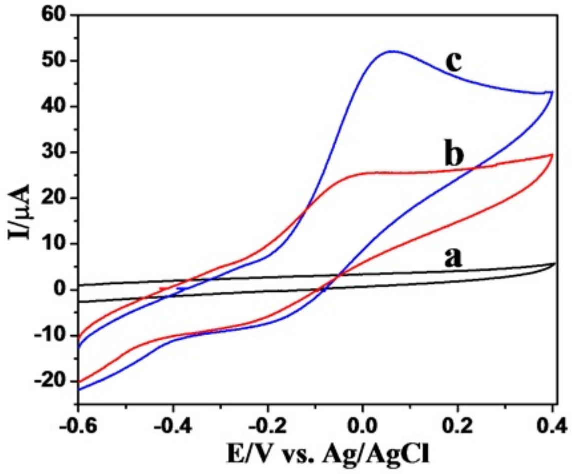

FIG. 3. Electrocatalytic behavior of a) bare, b) bare-with AA (1 mM) and c) AP-rGO/GCE with 1 mM of AA in 0.1 M PBS (pH 7) at scan rate 50 mV/s

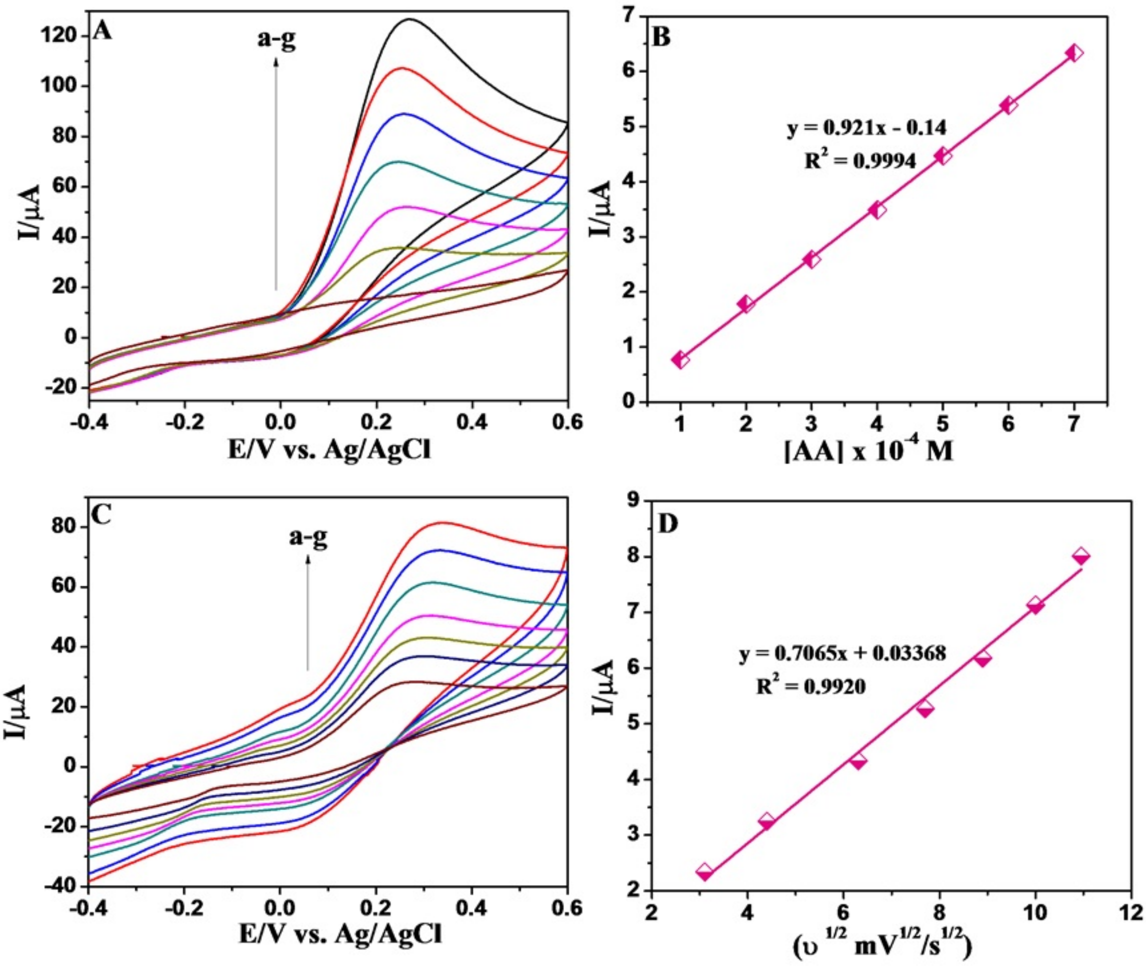

FIG. 4. A) AP-rGO/GCE in presence of AA in 0.1 M PBS (pH 7) at scan rate 50 mV/s and B) Linear plot of conc. vs. peak current. C) AP-rGO/GCE in presence of AA at different scan rates in 0.1 M PBS (pH 7) and D) Linear plot of Ip vs. $\upsilon^{1/2}$

3.3. Differential pulse voltammetry method

For the quantitative detection of ascorbic acid (AA) present in the pharmaceutical formulations and fruits samples at low concentration levels, the differential pulse voltammetry method was demonstrated using AP-rGO modified GCE under optimized experimental conditions. Fig. 5(A) shows differential pulse voltammogram for the electrocatalytic oxidation of AA using AP-rGO/GCE in PBS (pH 7) containing various concentrations of AA. The result shows the electrocatalytic peak current of AA oxidation at the AP-rGO/GCE was linearly dependent on the AA concentration and its ranges from 0.3 μM to 3 μM. As seen from Fig. 5(B), the calibration plot shows electrocatalytic peak current (I_p) versus AA concentrations with linear regression equation of $y = 0.494x - 0.212$ with correlation coefficient of 0.9923 and the detection limit (3σ/slope, σ is a standard deviation) is found to be 20 nM. These results strongly suggest that the oxidation of AA can be good selective and sensitive at aniline AP -rGO/GCE.

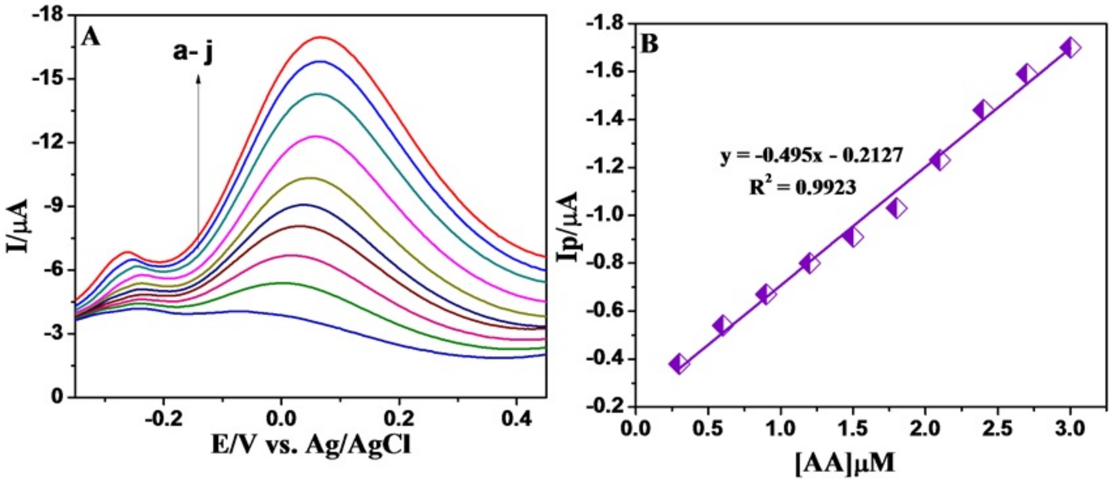

FIG. 5. A) DPV of AP-rGO/GCE in presence of AA at various concentrations (0.3–3.0 μM) in 0.1 M PBS (pH 7). B) Linear plot of concentration vs. peak current

3.4. Food sample analysis

In order to estimate the amount of AA present, fruit juice food samples were analyzed. Based on the repeated differential pulse voltammetric responses ($n = 5$) of the diluted analyte, samples were spiked with specified concentration of AA, measurements were made for determination of AA concentration in food samples. The results are listed in Table 1. The AP-rGO/GCE possessed reasonable selectivity and produced satisfactory recovery result with an average recovery of 100.3 % and the RSD was less than 5.3 %. The measured data of AA concentration was in good agreement with the results found in the titration measurements, suggesting the good accuracy and reliability.

TABLE 1. Determination of AA in fruit samples

Samples	Added (10^{-6} g/ml^{-1})	Found (10^{-6} g/ml^{-1})	Recovery (%)
Apple	0.50	1.024	99.3
Pineapple	0.70	1.208	100.6
Orange	1.50	2.133	101

4. Conclusion

A single step method was adapted to modified graphene sheet with aniline pentamer as electron transfer mediator. The surface modification of graphene was confirmed from FTIR and cyclic voltammetry studies. A simple differential pulse voltammetry method was developed to determine low concentration ranges of ascorbic acid using aniline pentamer grafted graphene sheet. Enhanced detection limits was achieved using this method. The present method can be utilized for the electrochemical detection of ascorbic acid in pharmaceutical and fruit samples.

Acknowledgement

The authors (Dr. K. P and S. M.) are grateful to DST purse programme to upgrade the Gamry 330 electrochemical system (DPV software).

References

[1] DeNobili M.D., Perez C.D., Navarro D.A., Stortz C.A., Rojas A.M. Hydrolytic stability of L-(+)-ascorbic acid in low methoxyl pectin films with potential antioxidant activity at food interfaces. *Food Bioprocess Technol.*, 2011, **6**, P. 186–197.

[2] Jens L. Determination of ascorbic acid and dehydroascorbic acid in biological samples by high performance liquid chromatography using subtraction methods: Reliable reduction with tris (2-carboxyethyl) phosphine hydrochloride. *Anal. Biochem.*, 2000, **282**, P. 89–93.

[3] Yu Y.H., Donat P.H. UV-B-induced formation of reactive oxygen species and oxidative damage of the cyanobacterium *Anabaena sp.*: protective effects of ascorbic acid and N-acetyl-L-cysteine. *J. Photochem. Photobio. B: Biology*, 2002, **66**, P. 115–124.

[4] Wu T., Guan Y., Ye J. Determination of flavonoids and ascorbic acid in grapefruit peel and juice by capillary electrophoresis with electrochemical detection. *Food Chem.*, 2007, **100**, P. 1573–1579.

[5] Ping J., Wang Y., Wu J., Ying Y., Ji F. Determination of ascorbic acid levels in food samples by using an ionic liquid carbon nanotube composite electrode. *Food Chem.*, 2012, **135**, P. 362–367.

[6] Francis F.J. *Wiley encyclopedia of food science and technology*, 2-nd ed., Vol 4. Wiley, New York, 1999.

[7] Habibi B., Pournaghi-Azar M.H. Simultaneous determination of ascorbic acid, dopamine and uric acid by use of a MWCNT modified carbon-ceramic electrode and differential pulse voltammetry. *Electrochimica Acta*, 2012, **55**, P. 5492–5498.

[8] Roy P.R., Saha M.S., Okajima T., Ohsaka T. Electrooxidation and amperometric detection of ascorbic acid at GC electrode modified by electropolymerization of N, N-Dimethylaniline. *Electroanalysis*, 2004, **16**, P. 289–297.

[9] Florou A.B., Prodromidis M.I., Stella M.T.K., Miltiades I. Fabrication and voltammetric study of lanthanum 2,6-dichlorophenolindophenol chemically modified screen printed eletrodes: Application for the determination of ascorbic acid. *Anal. Chimica Acta*, 2000, **423**, P. 107–114.

[10] Zuo X., Zhang H., Li N. An electrochemical biosensor for determination of ascorbic acid by cobalt (II) phthalocyanine- multiwalled carbon nanotubes modified glassy carbon electrode. *Sensors Actuat.*, 2012, **161**, P. 1074–1079.

[11] Hummers W.S., Offemn R.E. Preparation of graphitic oxide. *J. Am. Chem. Soc.*, 1958, **80**, P. 1339.

[12] Huang L., Hu J., Lang L., Wang X., Zhang P., Jing X., Wang X., Chen X., Lelkes P.I., MacDiarmid A.G., Wei Y. Synthesis and characterization of electroactive and biodegradable ABA block copolymer of polylactide and aniline pentamer. *Biomaterials*, 2007, **28**, P. 1741–1751.

NANOSYSTEMS:

PHYSICS, CHEMISTRY, MATHEMATICS

Журнал зарегистрирован
Федеральной службой по надзору в сфере связи, информационных технологий и массовых коммуникаций
(свидетельство ПИ № ФС 77 - 49048 от 22.03.2012 г.)
ISSN 2220-8054

Учредитель: федеральное государственное автономное образовательное учреждение высшего образования
«Санкт-Петербургский национальный исследовательский университет информационных технологий, механики и оптики»

Издатель: федеральное государственное автономное образовательное учреждение высшего образования
«Санкт-Петербургский национальный исследовательский университет информационных технологий, механики и оптики»

Отпечатано в Учреждении «Университетские телекоммуникации»
Адрес: 197101, Санкт-Петербург, Кронверкский пр., 49

Подписка на журнал НФХМ
На первое полугодие 2017 года подписка осуществляется через
ОАО Агентство «Роспечать»
Подписной индекс 57385 в каталоге «Издания органов научно-технической информации»